Plasmonic enhancement of fluorescence for biomedical diagnostics

By

Ondrej Stranik M.Sc. (Hons)

A Thesis presented

to

Dublin City University

For The Degree Of Doctor Of Philosophy

Research Supervisors:

Prof. Brian MacCraith, Prof. Colette McDonagh

School of Physical Sciences,

Dublin City University.

March 2007

Declaration

I hereby certify that this material, which I now submit for assessment on the programme of study leading to the award of Doctor of Philosophy is entirely my own work and has not been taken from the work of others save and to the extent that such work has been cited and acknowledged within the text of my work.

Signed: _____ (Candidate) ID No.: 52171302

Date: 24.7.2007

Acknowledgements

First of all, I would like to thank Prof. Brian MacCraith and Prof. Colette McDonagh for allowing me to study in their research group and for their invaluable supervision throughout my Ph.D. study, which is very much appreciated.

I would also like to thank Dr. Robert Nooney, who revealed to me the interesting chemistry of nanoparticles, and our work together was very rewarding. Long discussions and arguments with Rob about world of nanoscience was very enjoyable and useful, which brought a lot of excellent ideas.

Next, I have to thank Orla McGaughey for assisting with pin-printer immobilisation routines on substrates, and Helen McEvoy for assistance with antibodies and construction of flow cells.

A big thank you should be given to colleagues who patiently read drafts of this thesis. I want to thank Bob Blue, who helped me the most, but also Rob Nooney, Helen McEvoy, Conor Burke and Aoibheann Bird.

For the help with the everyday problems in the laboratory and for friendship I would like to thank Conor Burke and John Donohe and later Bob Blue, Michal Trnavsky and Orla McGaughey.

Overall, I have to thank all the members of the Optical Sensor Laboratory group at DCU, because they are amazing group of people, which made my study very pleasant, especially Honza Hradil, Rapheal Kribich, Rob Nooney, Scott Spillman and Thomas Ruckstuhl whose scientific discourse and insights during the duration of my studies was very enjoyable.

Finally, I would like to thank my parents and Janja for supporting and encouraging me throughout my stay in Ireland.

Abstract

The enhancement of fluorescence that can result from the proximity of fluorophores to metallic nanoparticles (NP's) is investigated. This plasmonic enhancement, which is a result of the localized surface plasmon resonance (LSPR) at the metal surface, can be exploited in order to improve the signal obtained from optical biochips and thereby lower the limits of detection. The scale of the enhancement depends on many parameters such as NP size and shape, metal type and NP-fluorophore separation. Throughout the work, theoretical calculations were carried out, and, where relevant, theoretical predictions were compared with experimental measurements. Characterisation techniques used include TEM, AFM as well as optical fluorescence and absorption. The first section deals with the production of ordered arrays of nanostructures, of varying size and composition, on glass substrates using a nanosphere lithography technique. The ability to tune the peak wavelength of LSPR was demonstrated. Fluorescent dyes were then pin-printed onto the NP layer and the fluorescence enhancement was measured. The second body of work involved characterising the enhanced fluorescence from dyes attached to free NPs in solution. NPs of sizes ranging from 5 to 50nm radius and with different gold/silver alloy compositions were prepared by wet chemistry. The NPs were coated with silica shells to control the dye-NP separation and to minimise quenching. The dependence of the enhancement on NP size was found to agree well with theoretical calculations based on the Mie theory. The final body of work focused on the development of strategies applicable to polymer biochips. This included the development of techniques for immobilising NPs on plastic substrates. A range of dyes and a range of NP shapes were investigated. Dye-NP separation was controlled to nanometer precision by layer-by-layer deposition of polyelectrolytes. In this configuration, both dye quenching and enhancement effects were observed and characterised. The key result to emerge from this work was that it is possible to design an optical biochip enhancement platform where the NP shape, size and composition are optimised for the selected dye label and where the average dye-NP separation is designed to achieve maximum enhancement.

Contents

Chapter 1

Introduction

1.1 Nanotechnology

Over the last few decades nanotechnology has become one of the main areas of focus in scientific research and development and it is believed that it will be a key enabling technology of the 21^{st} century. Nanotechnology is generally understood as an area of science and technology involving the assembly, manipulation and control of matter on a functional scale smaller than one tenth of a micrometer. It is a highly multidisciplinary field, which cuts across many fields, such as colloidal science, applied physics, material science, supramolecular chemistry and biology. The impetus for the development of nanotechnology was a demand for the reduced size of devices in microelectronics [1], construction of new analytical tools such as the Atomic Force Microscopy and the Scanning Tunnelling Microscopy which enable nanometer scale resolution, the concept of noncrystalline materials [2] and development of electron beam lithography.

A unique aspect of nanotechnology is that the reduction of the size of materials to the nanometer scale leads to a change of material properties, which differ markedly from those of the corresponding bulk material. The changes are observed in a variety of electrical, optical, mechanical, and magnetic properties of the structure. For example, nanometer-scale thin films of semiconductor exhibit quantum size effects, where the density of the electronic states is altered [3]. If the semiconductor material is restricted in three dimensions, quantum dots are formed, which have a discrete energy spectrum depending on their size. These

quantum dots can fluoresce and their emission spectra are dependent on the diameter of the nanoparticle [4]. Other examples of changing optical properties by decreasing the size are metallic nanoparticles. Metallic nanoparticles exhibit localised surface plasmon resonance, which causes strong absorption of the light by the particles, a property which is not present in bulk material [5]. Also, by decreasing the size of the object, the ratio of surface area to volume is vastly increased. This causes changes in mechanical properties such as hardness and toughness [6]. Additionally, there may be changes in the chemical properties of the material. The large surface significantly increases the reactivity of the catalytic reactions and the melting point of the material is lowered. These examples represent only a small number of the many effects that can by achieved by reducing the size of the object, and demonstrating the variety of possible applications of nanotechnology.

1.2 Metal nanoparticles, their properties and applications

A significant area of nanotechnology is production, characterisation and application of metal nanoparticles. A metal nanoparticle is defined as a particle with at least one dimension less than 100nm. Due to their small dimensions, metal nanoparticles acquire some special physical and chemical properties, which are used in a variety of applications.

Probably the most intriguing property of metal nanoparticles is their strong absorption in the visible spectrum giving them a specific colour depending on the geometrical parameters of the nanoparticles. Such nanoparticles were first used by the Romans in the 4^{th} century AD, who exploited the strong absorption of gold nanoparticles by adding nanoparticles (in the form of powder) to glass to produce a red stained-glass vase [7] (see Lycurgus cup in figure 1.1). Later in the middle ages, gold and copper (red) or silver (yellow) nanoparticles were used for staining windows in cathedrals (for example Freiburg Munster, Germany). However, it was not until the beginning of the 20^{th} century that the absorption of metal nanoparticles was fully understood and described in the framework of electrodynamics [8]. With increasing interest in nanoparticles, new properties

Figure 1.1: The Lycurgus Cup from 4^{th} century AD. The glass contains gold nanoparticles. In reflected light the cup seems green, in transmitted light the cup appears red. Courtesy of the British Museum.

of nanoparticles have been discovered, which are being exploited in present day technology. An ordered array of metal nanoparticles can be used as a polarisation filter with excellent thermal and optical stability. This application exploits the fact that the absorption of non-spherical nanoparticles depends on their orientation [9]. Due to the high nanoparticles scattering they can enhance the efficiency of thin semiconductor photo-detectors by improved coupling of the light into the detection area [10].

Besides scattering, nanoparticles absorb incident light whose energy is then changed into heat and transferred to the surrounding material. Optically-controlled valves made from nanoparticle-hydrogel composites are based on this effect, in which the nanoparticle by illumination heat the hydrogel, which swells and closes the valve [11].

The particulate films of silver or gold films can be used for optical recording or for photographic applications [12, 13]. Recording is carried out by irradiating the particulate films by a laser. Due to the very low sintering temperature of the particles, the optical properties of the particulate films is altered.

Because illuminated nanoparticles have a strong local electromagnetic field which can interact with adjacent nanoparticles, they can be used in optics to guide light below the diffraction limit [14, 15], such as optical waveguides, mirrors, beam splitters or even logical switches of sizes smaller than the wavelength of

the used light. It has been discovered that nanoparticles, and especially their aggregates, have strong non-linear optical properties [16], which can be used instead of simple inorganic optical non-linear crystals, and offer better mechanical properties and structural and physical tailorability. Further, the surface-enhanced Raman scattering effect of metallic nanoparticles increases the Raman signal of molecules attached to the nanoparticles [17].

Metal nanoparticles have also interesting electrical properties, which are investigated in order to decrease the size of electronic devices to the nanoscopic level. If the particles are arranged within about 1nm of each other, tunnel junctions with very low capacitance are created, which allow single electron transport between particles leading to staircase-shaped I-V curves, which is used for building nanotransistors [18]. This effect was also applied to build unusual humidity sensors based on hybrid structures of microorganisms and nanoparticles. A bacterium, which was sensitive to humidity by changing its size, was covered by nanoparticles. The current passing through the nanoparticles depends on the size of the bacteria and therefore the humidity [19]. Silver nanoparticles can also be used for high-conductivity elements in circuit boards in printed electronics [20, 21, 22]. The nanoparticles in solution are simply printed on the electronic circuit and, due to their small size, the annealing temperature at which nanoparticles form a continuum conducting layer, is much lower than in the case of bulk silver, hence fulfilling the low-temperature processing requirements in electronics.

This short list of examples of the application of nanoparticles is merely an introduction to this interesting field, which, although still in its infancy, has many areas under investigation and many more potential developments and discoveries on the horizon.

1.3 Applications of metal nanoparticles in biology

From the previous examples it is obvious that nanoparticles have a broad range of application in many areas of science. In this section the focus is on the application of nanoparticles in biology.

Interestingly, colloid silver nanoparticles exhibit antibacterial properties [23]

and this effect was used in medicine as early as the late 19^{th} century as an anti-infection measure in the form of nose drops and common cold remedies. However, this application of silver nanoparticles is now replaced by the use of antibiotics, due to the side-effect called argyria, resulting in a metallic grey skin of the patients taking the nanoparticles [24]. However, the main application of the nanoparticles in biology is in biodiagnostics, where they open new ways to detect molecules [25, 26, 27, 28, 29, 30, 31], especially in screening for nucleic acids, proteins and some biologically relevant small molecules. In the following section, the current methods of detection of biological molecule are presented followed by examples of using nanoparticles in bio-detection.

1.3.1 Overview of biosensors

In biodiagnostics either part of a nucleid acid, which is unique to viruses and pathogens, or certain proteins can be used for identification of various diseases. The device in which the detection is achieved by biological recognition elements (due to the high sensitivity and specificity of biological molecules) is called a biosensor [32]. The biomolecules incorporated into the sensor are chosen for their specificity with which they recognise a particular analyte. The biomolecules employed in biosensors include antibodies, enzymes, receptors or DNA probes. The biomolecule-analyte binding reaction results in physical or chemical changes that may result in the production of ions, electrons, heat, mass or light [32]. Alternatively, the analyte can be labelled with tags ('biomarkers') that are easily detectable. Such tags are commonly fluorescent or colored dyes, radioisotopes, or enzymes.

In the area of protein diagnostics, the current standard is the enzyme-linked immunosorbent assay (ELISA), which is mainly used to detect the presence of antigen or antibody in a sample. There are several formats of detection, and one of the most common is the sandwich assay design presented in figure 1.2. The principle is the following: (1) a known-quantity of the antibodies is attached to the substrate, often a well of a microtiter plate. (2) sample containing the antigen is applied into the wells. (3) The plate is washed and the enzyme-linked antibodies which are also specific to the antigen are added. These antibodies attach to the bound antigen. (4) A chemical substrate is applied which is converted by

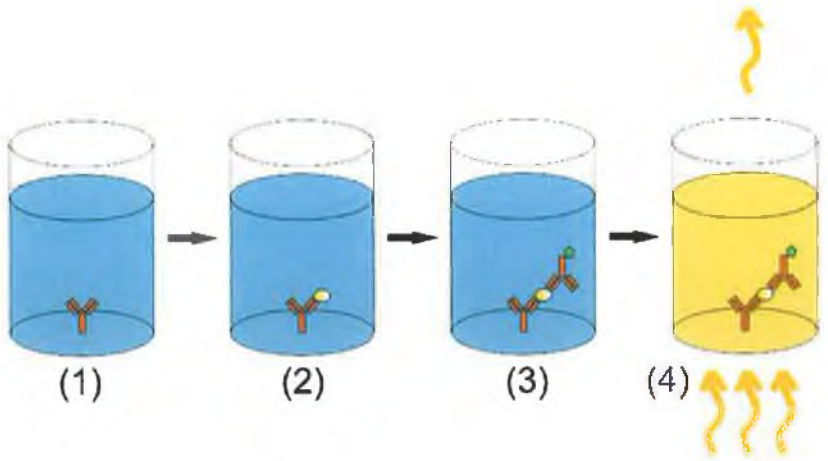

Figure 1.2: The steps in ELISA method. (1) recognition element (antibody) is attached to the substrate. (2) the present antigen (molecule of interest) binds to the capture antibody. (3) labelled antibody binds to antigen. (4) the enzyme change the optical properties of a substance (absorption)

the enzyme into a color change (an absorption signal) which is then optically detected. The standard detection limit can be in ~pM range [25]. There are many companies on the market selling ELISA kits and efforts are being made to incorporate microfluidics into the ELISA systems, which decreases the detection time [33].

Another biosensor already commercially available is based on surface plasmon based detection (for example the BIAcore^{TM} system from Biacore). The basic principle of the technique is presented in figure 1.3. The system consists of a metal layer on a glass substrate with attached antibodies. Polarised light is shone on the metal layer through the substrate at various angles and the reflected beam is measured. At particular angle the light is coupled into the metal layer, thereby decreasing the intensity of the reflected beam [34]. Upon binding of the analyte to the antibody, the local refractive index is changed leading to the shift of a angle which indicate the presence of the analyte. New detection concepts of this method based on phase measurement using a grating coupler or incorporation of integrated optics to increase the sensitivity, are being developed [35, 36]. The main advantages of these systems are suitability for real-time and kinetics

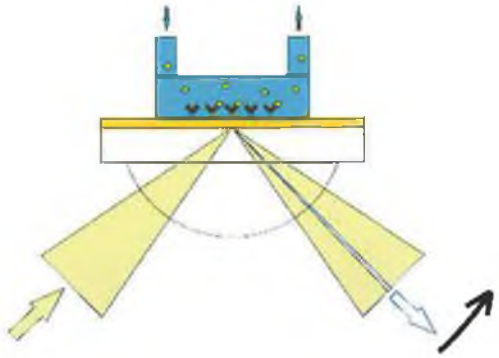

Figure 1.3: BIACore system based on Surface Plasmon Resonance. Upon the binding of an analyte to the attached antibodies, the dip in reflection at which SPR occurs shifts to higher angles.

measurement (label-free) and their high sensitivity. The limitations are the high sensitivity to temperature and bulk refractive index shift. Additionally, there are not so selective due to the non-specific adsorption of molecules to the substrate.

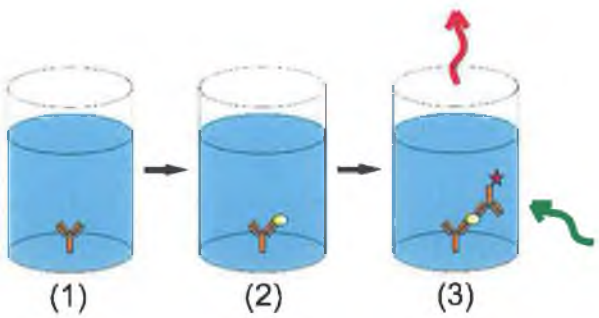

Figure 1.4: The steps in fluorescence-based bio-sensor. (1) recognition element (antibody) is attached to the substrate. (2) the present antigen (molecule of interest) binds to the capture antibody. (3) fluorescent dye-labelled antibody binds to antigen, which presence is detected by a fluorescence signal from the dye.

The third commonly used type of biosensor, which is of interest for this thesis, is the fluorescence-based biosensor. The format of the antigen detection is

similar to the case of ELISA, but the secondary antibody is not labelled with an enzyme but with a fluorophore (see figure 1.4). The presence of the antigen is then detected by illuminating the sample and measuring the intensity of a fluorescence signal from the fluorophore. The biggest advantages with regards to the ELISA system are spatial resolution, multianalyte detection, sensitivity and rapid detection [37].

The demand for detection of a very low concentration of antigens has lead to the need for improvement in the sensitivity of the fluorescence-based sensors. This was the main drive for starting the research described in this thesis. There are a variety of possible ways of enhancing the performance of the sensors. The most obvious solution is the use of quality optics and a highly sensitive detection system. Currently, detection of single fluorescent molecules and even measurement of their orientation is possible [38, 39]. Therefore, even a single biomolecule could be detected leading to infinitesimally low limit of detection and the limitation of such a sensor would be given by the diffusion rates of reagent (it would take too long for reagents to reach the biorecognition elements for very low concentration) and the affinity of the reagent-biorecognition element interaction (there is an equilibrium between the reagents attached to the substrate and the reagents in the solution). However, these single fluorescence detection systems are very expensive bench-top devices (for example systems from PicoQuant GmbH, Germany) used only in laboratories requiring skilled personnel and can not be implemented in low-cost portable bio-sensors. For this reason, alternative simple, compact and cheap methods for enhancement of detection of the fluorescent signal are sought.

One of the strategies is the employment of an interference layer, which is deposited between the substrate and the antibodies. Due to the presence of this interference layer two effects occurs: the excitation is enhanced by constructive interference of the illumination light and reciprocally the fluorescence emission rate can be enhanced by interference of the emission light. This method leads to several fold enhancement of the signal [40]. Alternatively, special geometry of the optics can be employed for excitation of the fluorophore and collection of the emitted fluorescence in order to suppress the signal from unbound labelled molecules from solution. For the excitation a method called total internal reflection fluorescence is used [41] exploiting the advantages of total internal reflection. The excitation beam passing through the substrate illuminates the interface at

the angle larger than critical angle causing no propagation of light into the sensing area. The excitation field is evanescent at the interface and extends only a few hundred nanometers into the solution. Therefore, only the bound fluorophore labelled molecules are excited and subsequently detected. A complementary effect to this is used in supercritical angle fluorescence method (SAF) [42, 43]. Due to total internal reflection, fluorescence from unbound labelled molecules in solution can not be emitted into the substrate (the refractive index of substrate is higher than of solution) at angles larger than the critical angle (water-glass interface $=61^{o}$). However, a fluorophore in the proximity (less than emission wavelength) of an interface emits light into angles larger than critical angle [44]. Therefore, the fluorescence from bound analytes can be distinguished from fluorescence from unbound analyte by collecting the fluorescence light from angles above critical angle. A similar technique using the anisotropic emission of a fluorophore is called surface plasmon-coupled emission (SPCE), here a thin metallic layer is located between the substrate and biorecognition layer [45, 46]. The additional layer causes molecules close to the interface to have a distinct angle-dependant emission with the majority of the fluorescence emitted into a very narrow angle range. Because the emitted angle depends on the emission wavelengths, this gives the possibility of multianalyte detection. Fluorescence from the unbound molecules in solution is not transmitted through the metallic layer, therefore only fluorescence from the bound analyte is detected. Lastly the development of new ultra bright labels is considered. This involves the chemical engineering of new molecules with desirable emission and excitation wavelengths to form a new class of labels, which consist of silica nanoparticles doped with large amount of standard fluorophore [47, 48]. Their advantages compared to a single fluorophore are higher brightness, better photostability, insensitive to the solution effects, and possible shift of the emission wavelength using two dyes incorporated into the particle [49].

1.3.2 The use of metal nanoparticles in biosensors

The use of metallic nanoparticles is another way to improve performance of biosensors or even to develop a new way of detecting biomolecule-analyte binding reactions. In the following, a short account of possible applications of nanoparti-

cles in biosensors is mentioned, concluding with an introduction to the plasmonic enhancement of fluorescence.

Metal nanoparticles were first applied in bioanalysis as probes in transmission electron microscopy [50]. Due to their high density, they are very easily detectable, enhancing the contrast of the images.

Due to the extraordinary light absorption and scattering of nanoparticles they can be used as tags in biological assays in optical detection systems. The system of biorecognition can be the same as in the case of a fluorescence-based sensor, but instead of fluorescent tags, a gold nanoparticle is used. The detection is then carried out via an absorption-based measurement. Due to the distinct red color of the nanoparticles the detection can be even done in some cases by the naked eye. Currently pregnancy tests using gold nanoparticles combined with such visual detection are commercially available on the market (for example, first response Easy-Read Ovulation Test). This concept is being further developed to produce low cost immunoassays with detection limits comparable with the ELISA method [51, 52]

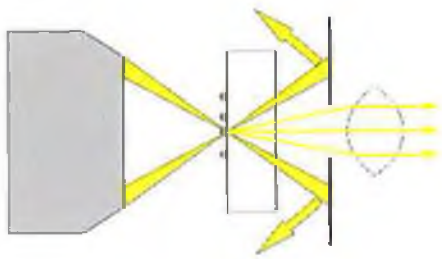

Figure 1.5: Schematic of detection NPs using dark field microscopy. A substrate with NPs is illuminated with beam of light in the form of ring which strikes the surface under high angles. It is achieved via an objective with high numerical aperture and an O-ring aperture. Only the light scattered by nanoparticle in low angles is collected via objective with low numerical aperture.

In a similar way, metal nanoparticles can be used as tags, but instead of the absorbed light, the scattered light is detected [53]. Slightly larger nanoparticles have to be used than in the case of absorption, but, when optimised, the intensity of the scattered light of one nanoparticle is equal to the fluorescence intensity

of approximately one million of fluorescent dyes [54]. Moreover, by using dark field microscopy even a single nanoparticle can be detected, hence significantly increasing the sensitivity of sensors [55]. A schematic of dark field microscopy is shown in figure 1.5. Basically, a substrate is illuminated at high angles so that the incident light is not transmitted by the collection optics. But in the presence of a nanoparticle the incident light is scattered at lower angles resulting in detection of this light. The nanoparticles on an image then appear as bright spots on a black background. The next development in this technique is the use of striped metal nanoparticles allowing multiplexing [56]. These special nanoparticles consist of gold and silver stripes. Due to the different optical properties of the metal, the silver regions appear brighter than the gold regions, thus the nanoparticle acts as a bar-code when viewed in dark field microscopy. By tagging each antibody type with specific bar-code NP, the multiplexing is achieved.

Besides the detection of nanoparticles attached to a substrate by optical methods they can be also detected electrically, electrochemically, topologically or by mass spectrometry. In the electrical approach, two electrodes are present close to the detection spot and by capturing the antibodies tagged with nanoparticles the change of resistance or electrical current is detected [57]. In the electrochemical approach, after the capturing of NP-tagged antibodies, the metallic nanoparticles are dissolved and the metal is detected by the use of stripping potentiometry [58]. In another approach the attached antibodies labelled with nanoparticles form a rough surface, which can be detected by atomic force microscopy [57]. However, this approach is not yet practical for use in miniaturised sensors.

Another way of using nanoparticles as a transducer of binding events is exploiting the high sensitivity of their optical properties to change of refractive index of the surrounding medium [59, 28, 60]. A schematic of this sensor type is shown in figure 1.6. The sensor consists of a layer of attached nanoparticles which are covered with biorecognition elements and the absorption of the nanoparticles is monitored. Upon binding the reagents to the biorecognition elements, the local refractive index around the nanoparticles is changed causing the change of absorption spectra of the nanoparticles. This principle is similar to the standard surface plasmon resonance system described earlier, but the approaches differ in aspects of spatial resolution, distance dependence, sensitivity and cost [61].

Further, metal NPs can be also used in solution phase sensors exploiting the

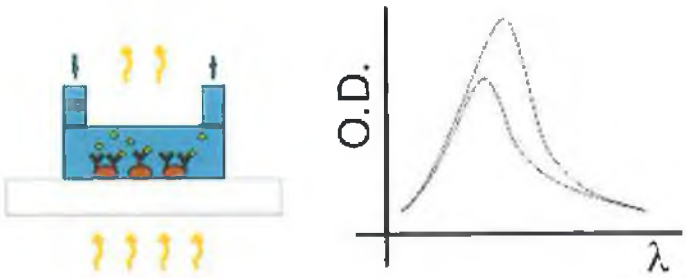

Figure 1.6: Schematic representation of biosensors based on change of NPs absorption caused by adsorption antigens to the antibodies attached to the nanoparticles. Upon binding of the antigen to the antibodies (left) the local refractive index around NPs is changed resulting in increase and shift of NPs absorption, which is detected by measuring the absorption (right).

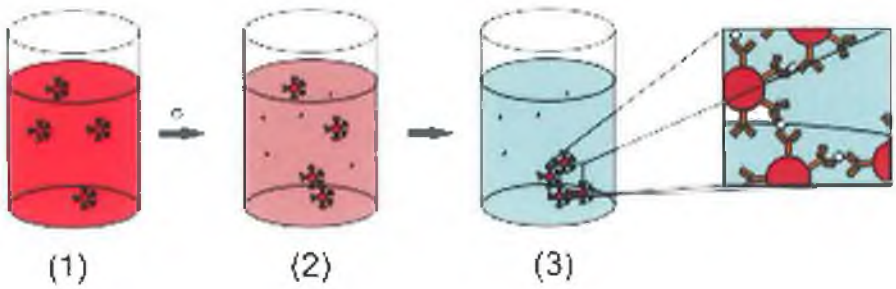

Figure 1.7: Schematic representation of biosensors based on aggregation of NPs. Without presence of reagent the nanoparticles are dispersed in solution giving it a red color. After adding the reagent the nanoparticles aggregate causing the solution to be transparent.

color change of the solution upon aggregation of the nanoparticles. A schematic of this sensor type is in figure 1.7. The principle is based on the earliest type of biosensors using latex microspheres covered with antibodies. When antigen is added to the solution, microspheres aggregate and the turbid solution become

transparent [32]. The metal nanoparticles have an advantage in much higher light absorption resulting in higher sensitivity of such sensors. Additionally, by using metal nanoshells instead of metal nanoparticles the absorption is shifted to longer wavelengths, where blood is already transparent, and the presence of an antigen in whole blood can be detected [62].

Instead of using a fluorescent label as a tag, a Raman active dye together with a metal nanoparticle can be attached to the molecule of interest and the surface enhanced Raman signal can be detected [63]. Because the Raman signal is highly specific for each molecule, multiplexing can be easily achieved. Earlier the application of a Raman active molecule as a tag hindered the fact that the Raman signal from a molecule is several orders of magnitude weaker than fluorescence signal, and therefore fluorescence tags were preferably used. But it was discovered that the Raman signal from a molecule can be significantly enhanced by the presence of a metal nanoparticle [17, 64, 65, 66] enabling its detection. In another configuration, the metal nanoparticles are deposited on a substrate and the biorecognition elements are deposited over the nanoparticles. After binding of the tagged molecules, the surface enhanced Raman signal is detected [67], or even in some cases the molecule can act as a Raman active label [68, 69] avoiding the need for labelling the molecule.

Many other applications of metal nanoparticles in bio-sensors, which can improve the sensitivity have been reported such as a combination of nanoparticles with SPR-sensors [70], combination with mass spectrometric measurements or incorporating nanoparticles with molecular beacons [71]. But now we focus on the principal applications of the research within this thesis.

1.3.3 Application of metal nanoparticles in fluorescence-based biosensors

The main topic of this thesis is the interaction of metallic nanostructures with fluorescent dyes. It was theoretically formulated [72, 73, 74] and experimentally discovered [75, 76] that metal nanoparticles not only enhance the Raman signal but also the fluorescence signal from molecules near the nanoparticles. The effect of the enhanced fluorescence via nanoparticles can be pictured by analogy to radio techniques, where a fluorescent dye acts as a walkie-talkie and a nanoparticle acts

as an antenna, which amplifies the received and emitted signal. There are some similar processes in enhanced Raman spectroscopy and in fluorescence enhanced spectroscopy, where the enhancement is caused by the increased electromagnetic field around the nanoparticles. However, these effects have different intensities which depends on various parameters. Since the discovery of the enhanced fluorescence in the 80's several authors published the measurement of the effects and they tried to optimise it by varying several parameters [77, 78, 79, 80, 81, 82]. With the advance of the technique, even measurements of the effect on a single fluorescent dye and nanoparticle were carried out [83, 84]. Despite this effort, there is no definite answer to the optimal nanostructures for enhancement of the fluorescence. This involves an understanding of the very complex behaviour of the electromagnetic field interacting with the metal structures and, at the experimental level, the manipulation and controll of the position of the molecules and nanostructures on a nanometer scale.

Figure 1.8: Schematic representation of fluorescence based biosensors enhanced via plasmonic. The substrate is covered with metal nanoparticles, which enhance the fluorescence signal from dye labelled antibodies binding to the bound analyte.

Recently, some authors have applied this fluorescence enhancement effect to the detection of fluorescently labelled biomolecules in order to decrease the limit of detection and increase the sensitivity of the measurement [85, 86, 87, 88]. The schematic of the idea is shown in figure 1.8. The presence of the nanos-

tructures close to the biorecognition elements increases the fluorescence from the dye-labelled analyte and, therefore increasing the performance of the biosensor.

Inspired by these results, the enhancement of fluorescence-based biosensors via metallic nanostructures is the main scope of the work of this thesis. Its purpose is to analyse the possibility of the application of nanostructured surfaces onto fluorescence-based biosensors in order to increase their performance. Furthermore, the challenge is to develop a technique for the deposition of nanostructured surfaces onto biochips. In order to apply this enhancement strategy to the biochips the fabrication technique must fulfill several criteria such as low-cost, flexibility, reproducibility of the nanostructures, and the deposition of these structures on different substrate materials. Finally, these substrates will be then tested for their ability to enhance the fluorescence signal and parameters will be varied in order to optimise the performance of the biosensors.

1.4 Thesis structure

Chapter 1 provides an introduction to this work and describes the application of nanoparticles in general and then focuses on biosensors.

Chapter 2 introduces the principles of fluorescence and describes the optical properties of metal nanoparticles, especially the effect of localised surface plasmon resonance. Further, theoretical consideration is given to plasmonic enhancement of fluorescence.

Chapter 3 deals primarily with the formation of nanostructures via Nanosphere lithography techniques and thermal evaporation techniques. It is followed by a study of the enhancing effect of nanoparticles prepared by nanosphere lithography on fluorescent dyes. In particular, the dependence of the fluorescence enhancement on the optical properties of the nanoparticles is treated.

Chapter 4 deals with the plasmonic enhancement of fluorescence from molecules attached to the colloidal nanoparticles. The dependence of the fluorescence enhancement on the nanoparticle size and composition is studied (both, experimentally and theoretically)

Chapter 5 describes the development techniques for the production of nanostructured substrates which can be incorporated in biosensors. Firstly, methods of formation of nanoparticles with different optical properties are presented, espe-

cially photoconversion of spherical nanoparticles into triangular shaped particles. Next, the deposition of such nanoparticles on plastic and glass substrates is discussed. In the last section of Chapter 5, experiments dealing the measurement of the plasmonic enhancement of fluorescence from such substrates are described. Several parameters are varied to optimise the effect in order to produce fluorescence based sensors with enhanced sensitivity.

Finally, chapter 6 concludes the results achieved during the research and describes possible future methodologies for enhancing the performance of fluorescence-based biosenors incorporating metallic nanoparticles.

1.5 Thesis objectives

- To theoretically analyse the effects of Localised Surface Plasmon Resonance and consider its use in the enhancement of fluorescence. Further, to determine key parameters that influence the enhancement of fluorescence signal from fluorescent dyes (such as nanoparticle-dye distance, nanoparticle size and composition, optical wavelengths employed).

- To develop simple non-expensive techniques for the deposition of nanostructures on a range of surfaces.

- To experimentally observe the effect of plasmonic enhancement of fluorescence for dye molecules and to quantify its dependence on several parameters that can be adjusted to effect an optimisation of the fluorescence signal.

Bibliography

[1] R Kassing, P Petkov, W Kulisch, and C Popov. *Functional Properties of Nanostructured Materials*, volume 223 of *Series II: Mathematics, Physics and Chemistry*. Springer, 2006.

[2] R Wurschum. Textbook for a lecture "nanostructuren und nanotechnologie" at technische universitat graz, 2002.

[3] G Timp. *Nanotechnology*. Springer-Verlag New York, Inc., New York, 1999.

[4] A P Alivisatos. Semiconductor clusters, nanocrystals, and quantum dots. *Science*, 271:933–937, 1996.

[5] U Kreibig and M Vollmer. *Optical properties of Metal Clusters*. Springer Series in Materials Science. Springer-Verlag Berlin Heidelberg, 1995.

[6] S Veprek. The search for novel, superhard materials. *Journal of vacuum science & technology A*, 17(5):2401–2420, 1999.

[7] L Lee, G Seddon, and F Stephens. *Stained Glass*. Crown,, New York, 1976.

[8] G Mie. Beitrage zur optik trueber medien speziell kolloidaler metalloesungen. *Ann. Phys.*, 25:377–445, 1908.

[9] Y Dirix, C Bastiaanse, W Caseri, and P Smith. Oriented pearl-necklace arrays of metalllic nanoparticles in polymers: a new route toward polarization-dependent color filters. *Advanced Materials*, 11:223–227, 1999.

[10] H. R. Stuart and D. G. Hall. Absorption enhancement in silicon-on-insulator waveguides using metal island films. *Applied Physics Letters*, 69(16):2327–2329, 1996.

[11] L R Hirsch, A M Gobin, A R Lowery, F Tam, R A Drezek, N J Halas, and J L West. Metal nanoshells. *Annals of Biomedical Engineering*, 34(1, January):15–22, 2006.

[12] A. Werner and H. Hibst. Particulate au and ag films for optical-recording. *Applied Optics*, 28(7):1422–1428, 1989.

[13] K. Baba, Y. Ohkuma, T. Yonezawa, and M. Miyagi. Silver-based compound metal island films for write-once optical data-storage media. *Applied Optics*, 40(16):2796–2804, 2001.

[14] S A Maier and H A Atwater. Plasmonics: Localization and guiding of electromagnetic energy in metal/dielectric structure. *Journal of applied physics*, 95:011101, 2005.

[15] S A Maier, M L Brongersma, P G Kik, S Melzer, A A G Requicha, and H A Atwater. Plasmonics - a route to nanoscale optical devices. *Advanced Materials*, 13(19, October 2):1501–1505, 2001.

[16] Y Shen, C S Friend, Y Jiang, D Jakubczyk, J Swiatkiewicz, and P N Prasad. Nanophotonics: Interactions, materials, and applications. *Physical Chemistry B*, 104(32):7577–7587, 2000.

[17] M. Kerker, D. S. Wang, and H. Chew. Surface enhanced raman-scattering (sers) by molecules adsorbed at spherical-particles. *Applied Optics*, 19(19):3373–3388, 1980.

[18] D. L. Feldheim and C D Keating. Self-assembly of single electron transistors and related devices. *Chem. Soc. Rev.*, 27:1–12, 1998.

[19] V Berry and R F Saraf. Self-assembly of nanoparticles on live bacterium: Av avenue to fabricate electronic devices. *Angendte Chemie Int. Ed.*, 44:6668-6673, 2005.

[20] Y Li, Y Wu, and B S ONg. Facile synthesisi of silver nanoparticles useful for fabrication of high-conductivity elements for printed electronics. *Journal of the American Chemical Society*, 127:3266–3267, 2005.

[21] H H Lee, K S Chou, and K C Huang. Inkjet printing of nanosized silver colloids. *Nanotechnology*, 16:2436–2441, 2005.

[22] S Molesa, D R Redinger, D C Huang, and V Subramanian. High-quality inkjet-printed multilevel interconnects and inductive components on plastic for ultra-low-cost rfid applications. *Mat. Res. Soc. Symp.*, 769:H8.3.1, 2003.

[23] J R Morones, J L Elechiquerra, A Camacho, K Holt, J B Kouri, J T Ramirez, and M J Yacaman. The bactericidal effect of silver nanoparticles. *Nanotechnology*, 16:2346–2353, 2005.

[24] Akhil Wadhera and Fung Max. Systemic argyria associated with ingestion of colloidal silver. *Dermatology Online Journal*, 11(1):12, 2005.

[25] N L Rosi and C A Mirkin. Nanostructures in biodiagnostics. *Chemical Reviews*, 105:1547–1562, 2005.

[26] E Katz and I Willner. Integrated nanoparticle-biomolecule hybrid systems: Synthesis, properties, and applications. *Angew. Chem. Int. Ed.*, 43:6042–6108, 2004.

[27] S. G. Penn, L. He, and M. J. Natan. Nanoparticles for bioanalysis. *Current Opinion in Chemical Biology*, 7(5):609–615, 2003.

[28] N. Nath and A. Chilkoti. Label free colorimetric biosensing using nanoparticles. *Journal of Fluorescence*, 14(4):377–389, 2004.

[29] F Frederix, J M Friedt, K H Choi, W Laureyn, A Campitelli, D Mondelaers, G Maes, and G Borghs. Biosensing based on light absorption of nanoscaled gold and silver particles. *Anal. Chem.*, 75:6894–6900, 2003.

[30] D A Stuart, A J Haes, C R Yonzon, E M Hicks, and R. P. Van Duyne. Biological applications of localised surface plasmonic phenomenae. *IEE Proc.-Nanobiotechnology*, 152(1):13–32, 2005.

[31] M Seydack. Nanoparticle labels in immunosensing using optical detection methods. *Biosensors and Bioelectronics*, 20:2454–2469, 2005.

[32] S Y Rabbany, B L Donner, and F S Ligler. Optical immunosensors. *Critical reviews in Biomedical Engineering*, 22(5/6):307–346, 1994.

[33] E Eteshola and M Balberg. Microfluidic elisa: On-chip fluorescence imaging. *Biomedical Microdevices*, 6(1):7–9, 2004.

[34] H Raether. *Surface plasmons on smooth and rough surfaces and on gratings*, volume 111 of *Springer tracts in modern physics*. 1988.

[35] J Homola, S S Yee, and g Gauglitz. Surface plasmon resonance sensor: review. *Sensor and Actuators B*, 54:3–15, 1999.

[36] D K Kambhampati and W. Knoll. Surface-plasmon optical techniques. *Current Opinion in Colloid & Interface Sci.*, 4:273–280, 1999.

[37] H M McEvoy. *Development and Optimisation of Patterned Optical Immunosensors*. PhD thesis, Dublin City University, 2005.

[38] A. P. Bartko and R. M. Dickson. Imaging three-dimensional single molecule orientations. *Journal of Physical Chemistry B*, 103:11237–11241, 1999.

[39] H Gersen, M F Garcia-Parajo, L Novotny, J A Veerman, L Kuipers, and N F Van Hulst. Near-field effects in single molecule emission. *Journal of Microscopy*, 202(Pt 2, May):374–378, 2001.

[40] M Bras, V Dugas, F Bessueille, J P Cloarec, J R Martin, M Cabrera, J P Chauvet, R Souteyrand, and M Garrigues. Optimisation of a silicon/silicon dioxide substrate for a fluorescence dna microarray. *Biosensors and Bioelectronics*, 20:796–805, 2004.

[41] K E Sapsford, Y S Shubin, J B Delehanty, J P Golden, C R Taitt, L C Shriver-Lake, and F S Ligler. Fluorescence-based array biosensors for detection of biohazards. *Journal of Applied Microbiology*, 96:47–58, 2004.

[42] T Ruckstuhl and D Verdes. Supercritical angle fluorescence microscopy. *Optics express*, 12(18):4246–4254, 2004.

[43] L Polerecky. *Optimisation of multimode waveguide platforms for optical chemical sensors and biosensors*. PhD thesis, Dublin City University, Ireland, 2002.

[44] W Lukosz. theory of optical-environment-dependent spontaneous-emission rates for emitters in thin layers. *Physical review B*, 22(6):3030–3038, 1980.

[45] J. R. Lakowicz. Radiative decay engineering 3. surface plasmon-coupled directional emission. *Analytical Biochemistry*, 324(2):153–169, 2004.

[46] W R Holland and D G Hall. Waveguide mode enhancement of molecular fluorescence. *Optics Letters*, 10(8, August):414–416, 1985.

[47] Hooisweng Ow, D R Larson, M Srivanstana, B A Baird, W W Webb, and U Wiesner. Bright and stable core-shell fluorescent silica nanoparticles. *Nano Letters*, 5(1):113–117, 2005.

[48] X Zhao, R P Bagwe, and W Tan. Development of organic-dye-doped silica nanoparticles in a reverse microemulsion. *Advanced Materials*, 16(2, January 16), 2004.

[49] L Wang, Y Chaoyoung, and W Tan. Dual-luminophore-doped silica nanoparticles for multiplexed signaling. *Nano Letters*, 5(1):37–43, 2005.

[50] G M Hodges, J Southgate, and E C Toulson. Colloidal gold - a powerful tool in scanning electron microscope immunocytochemistry: an overview of bioapplications. *Scanning Microscopy*, 1(1):301–318, 1987.

[51] S K Sia, V Linder, B A Parviz, A Siegel, and G M Whitesides. An intergrated approach to a portable and low-cost immunoassay for resource-poor settings. *Angewandte Chemie Int. Ed.*, 43:498–502, 2004.

[52] J Liu, D Mazumdar, and Yi Lu. A simple and sensitie "dipstick" test in serum based on lateral flow separation of aptamer-linked nanostrures. *Angendte Chemie Int. Ed.*, 45:7955–7959, 2006.

[53] J M Kohler, A Csaki, J Reichert, R Moller, W Straube, and W Fritzsche. Selective labeling of oligonucleotide monolayers by metallic nanobeads for fast optical readout of dna-chips. *Sensor and Actuators B*, 76:166–172, 2001.

[54] J Yguerabide and E Yguerabide. Light-scattering submmicroscopic particles as higly fluorescent analogs and their use as tracer labels in clinical and biological applications - experimental characterization. *Analytical Biochemistry*, 262:157–176, 1998.

[55] A Curry, G Nusz, A. Chilkoti, and A Wax. Substrate effect on refractive index dependence of plasmon resonance for individual silver nanoparticles observed using darkfield micro-spectroscopy. *Optics express*, 13(7):2668–2677, 2005.

[56] I Walton, S Norton, A Balasingham, L He, Oviso D F, D Gupta, P A Raju, M J Natan, and R G Freeman. Particles for multiplexed analysis in solution: Detection and identification of striped metallic particles using optical microscopy. *Analytical Chemistry*, 74:2240–2247, 2002.

[57] A Csaki, M Moller, W Straube, J M Kohler, and W Fritzsche. Dna monolayer on gold substrates characterized by nanoparticle labeling and scanning force microscopy. *Nucleic Acisds Research*, 29(16):e81, 2001.

[58] J Wang, D Xu, A-N Kawde, and R Polsky. Metal nanoparticle-based electrochemical stripping potentiometric detection of dna hybridization. *Analytical Chemistry*, 73:5576–5581, 2001.

[59] A.J. Haes and R. P. Van Duyne. A nanoscale optical biosensor: Sensitivity and selectivity of an approach based on the localized surface plasmon resonance spectroscopy of triangular silver nanoparticles. *J. Am. Chem. Soc.*, 124:10596–10604, 2002.

[60] T. Okamoto, I. Yamaguchi, and T. Kobayashi. Local plasmon sensor with gold colloid monolayers deposited upon glass substrates. *Optics Letters*, 25(6):372–374, 2000.

[61] A. J. Haes and R. P. Van Duyne. A unified view of propagating and localized surface plasmon resonance biosensors. *ANALYTICAL AND BIOANALYTICAL CHEMISTRY*, 379(7-8):920–930, 2004.

[62] L R Hirsch, J B Jackson, A Lee, N J Halas, and J L West. A whole blood immunoassay using gold nanoshells. *Analytical Chemistry*, 75:2377–2381, 2003.

[63] S Schlucker, B Kustner, A Punge, R Bonfig, A Marx, and P Strobel. Immuno-raman microspectroscopy: In situ detection of antigens in tissue

specimens by surface-enhanced raman scattering. *Journal of Raman spectroscopy*, 37:719–721, 2006.

[64] G C Schatz and R P Van Duyne. Electromagnetic mechanism of surface-enhanced spectroscopy. In *Handbook of Vibrational Spectroscopy*. John Wiley & Sons Ltd. Chichester, 2002.

[65] D. A. Weitz, S. Garoff, J. I. Gersten, and A. Nitzan. The enhancement of raman-scattering, resonance raman-scattering, and fluorescence from molecules adsorbed on a rough silver surface. *Journal of Chemical Physics*, 78(9):5324–5338, 1983.

[66] Z Wang, S Pan, T D Krauss, and L J Rothberg. The structural basis for giant enhancement enabling single-molecule raman scattering. *PNAS*, 100(15, July 22):8639–8643, 2003.

[67] G A Baker and D S Moore. Progress in plasmonic engineering of surface-enhanced raman-scattering substrates toward ultra-trace analysis. *Anal. Bioanal. Chem.*, 382:1751–1770, 2005.

[68] M Green, F M Liu, L Cohen, P Kollensperger, and T Cass. Sers platforms for high density dna arrays. *Faraday Discussion*, 132:269–280, 2006.

[69] X Dou, Y Yamaguchi, H Yamamoto, S Dioi, and O Yukihiro. Nir sers detection of immune reaction on gold colloid particles without bound/free antigen separation. *Journal of Raman spectroscopy*, 29:739–742, 1998.

[70] L A Lyon, M D Musick, P C Smith, B D Reiss, D J Pena, and M J Natan. Surface plasmon resonance of colloidal au-modified gold films. *Sensor and Actuators B*, 54:118–124, 1999.

[71] B Dubertret, M Calame, and A J Libchaber. Single-mismatch detection using gold-quenched fluorescent oligonucleotides. *Nature Biotechnology*, 19:365–370, 2001.

[72] D. S. Wang and M. Kerker. Absorption and luminescence of dye-coated silver and gold particles. *Physical Review B*, 25(4):2433–2449, 1982.

[73] J. Gersten and A. Nitzan. Spectroscopic properties of molecules interacting with small dielectric particles. *Journal of Chemical Physics*, 75(3):1139–1152, 1981.

[74] H Chew, P J McNulty, and M Kerker. Model for raman and fluoresecent scattering by molecules embedded in small particles. *Physical review A*, 13(1):396–404, 1976.

[75] A M Glass, P F Liao, J G Bergman, and D H Olson. Interaction of metal particles with adsorbed dye molecules: Absorption and luminescence. *Optics Letters*, 5:368–370, 1980.

[76] A. Wokaun, H. P. Lutz, A. P. King, U. P. Wild, and R. R. Ernst. Energy-transfer in surface enhanced luminescence. *Journal of Chemical Physics*, 79(1):509–514, 1983.

[77] K. Sokolov, G. Chumanov, and T. M. Cotton. Enhancement of molecular fluorescence near the surface of colloidal metal films. *Analytical Chemistry*, 70(18):3898–3905, 1998.

[78] H Ditlbacher, N Felidj, J R Krenn, and F R Aussenegg. Electromagnetic interaction of fluorephores with designed two-dimentional silver nanoparticle arrays. *Appl. Phys. B Laser and Optics*, 73(4):373–377, 2001.

[79] G. Chumanov, K. Sokolov, B. W. Gregory, and T. M. Cotton. Colloidal metal-films as a substrate for surface-enhanced spectroscopy. *Journal of Physical Chemistry*, 99(23):9466–9471, 1995.

[80] R F Aroca, G J Kovacs, C A Jennigs, R O Loutfy, and P S Vincett. Fluorescence enhancement from langmuir-blodgett monolayers on silver island films. *Langmuir*, 4:518–521, 1988.

[81] J. Kummerlen, A. Leitner, H. Brunner, F. R. Aussenegg, and A. Wokaun. Enhanced dye fluorescence over silver island films - analysis of the distance dependence. *Molecular Physics*, 80(5):1031–1046, 1993.

[82] C Louis, S Roux, G Ledoux, L Lemelle, P Gillet, O Tillement, and P Perriat. Gold nano-antennas for increasing luminiscence. *Advanced Materials*, 16(23-24):2163–2166, 2004.

[83] P Anger, P Bharadwaj, and L Novotny. Enhancement and quenching of single-molecule fluorescence. *Physical Review Letters*, 96:113002, 2006.

[84] S Kuhn, U Hakanson, L Rogobete, and V Sandoghdar. Enhancement of single-molecule fluorescence using a gold nanoparticle as an optical nanoantenna. *Physical review letters*, 97(7 July):017402, 2006.

[85] J R Lakowicz, B Shen, and I Gryczynski. Intrinsic fluorescence from dna can be enhanced be metallic particles. *Biochem. Biophis. Res. Commun.*, 286:875–879, 2001.

[86] C D Geddes, H Cao, I Gryczynski, Z Gryczynski, J Fang, and J R Lakowicz. Metal-enhanced fluorescence (mef) due to silver colloids on a planar surface: Potential application of indocyanine green to in vivo imaging. *Journal of Physical Chemistry A*, pages 3443–3449, 2003.

[87] C D Geddes and J R Lakowicz. Metal-enhanced fluorescence. *Journal of Fluorescence*, 12(2, June):121–129, 2002.

[88] Ch. R. Sabanaygam and J R Lakowicz. Increasing the sensitivity of dna microarrays by metal-enhanced fluorescence using surface-bound silver nanoparticles. *Nucleic Acisds Research*, 00:1–9, 2006.

Chapter 2

Theoretical Background

In this chapter a theoretical review of the principles of plasmonic enhancement of fluorescence are presented. At first, molecular photoluminescence is explained in terms of an electron energy level model in molecules. In the next part, electromagnetic wave theory is reviewed. The localised plasmon resonance in metal nanoparticles is defined and its properties are described using electromagnetic theory. In the last section of this chapter, the influence of metal nanoparticles on the photoluminescence of molecules is explained.

2.1 Basic principles of molecular photoluminescence

Photoluminescence is a process whereby light is produced from the illumination of a molecule with radiation of a certain energy and the subsequent emitted light is of a lower energy. Photoluminescence can be of two types: fluorescence and phosphorescence. In all cases, it is necessary that an electron of the molecule is raised into the excited state before the molecule can emit radiation, but the processes whereby the molecule emits the light differ. For fluorescence, the excited electron returns to the ground state rapidly after the excitation, the time spent in the excited state being typically in order 10^{-8}s, whereas the typical time for phosphorescence is about $10^{-3}s$.

Before describing the process of photoluminescence, the energy levels in a molecule have to be defined. A molecule can absorb energy by promoting an

electron to a higher excited state or by inducing rotation and vibration of the molecule. Quantum theory states that molecules have discrete energy levels that depends on the structure of a molecule. A schematic representation of the energy levels in a molecule is shown in figure 2.1. The energy for excitation of an electron from the ground electronic state to higher energy states occurs in the UV-VIS range ($\sim$ 1eV). Vibrational energies and rotational energies occur in the infrared ($\sim$0.1eV) and microwave region ($\sim$1meV) respectively.

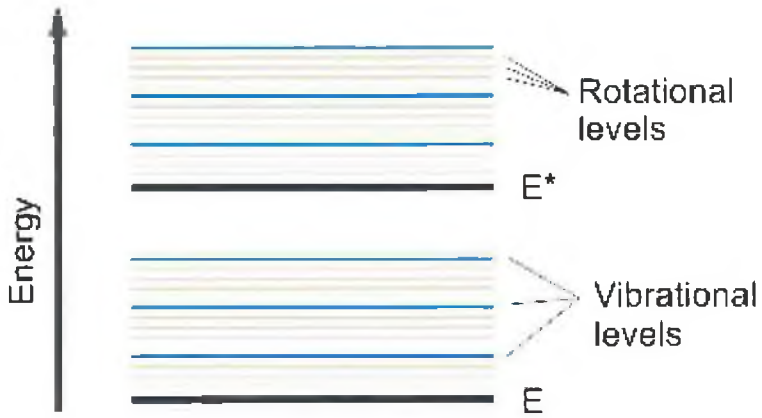

Figure 2.1: Energy levels in a model molecule. The E, E* level corresponds to the electronic states in the molecule, the next energetic levels are vibrational and rotational.

2.1.1 Absorption process

In photoluminescence the first step is absorption of a photon by a molecule. When a photon is absorbed by a molecule the energy is transferred to the valence electron which is promoted to a higher electronic orbital with additional vibrational and rotational energy. Prior to the excitation the molecular vibrational states are not excited at room temperature due to the low thermal energy. The process of the transition between electronic states is very quick, in order of 10^{-15}s. The energetic processes in a molecule can be visualied using the Jablonski diagram [1] (figure 2.2). In this diagram the absorption is represented by step (a). In or-

ganic molecules the valence electrons are in different orbital states called n, π, σ depending on the bonds between atoms in the molecule; and upon excitation, they undergo transfer to higher non-bonding energetic states called π^*, σ^*. Most absorption by organic compounds in the UV-VIS range is based on the transition of n or π electrons to the π^* excited state. In addition, electrons also have a spin, which does not change with absorption of a photon (the change is theoretically forbidden). Energetic levels with the same spin as the ground state are called singlet states and are indicated by the letter S. A more detailed description of energetic levels in organic molecules is given by Senk [2].

The probability of absorption of a photon depends on the initial and final states of the valence electron and on the final state of the molecule after absorption. The probability of the absorption is related to the molar absorptivity of the molecule $\epsilon(\lambda)$, which is a function of the photon's energy. The molar absorptivity reaches $10^5 M^{-1} cm^{-1}$ for transitions which are very likely to occur, whereas the absorptivity drops to $10^{-4} M^{-1} cm^{-1}$ for transitions which are theoretically forbidden [2]. The molar absorptivity can be determined from an experimental measurement of the absorbance of a dye using a UV-vis spectrophotometer and applying the Beer-Lambert law, which states that absorbance is proportional to concentration [3]. For a solution with molecules of concentration c, over a pathlength in a cuvette of length l, the absorbance is defined as $A = -log(T)$, where T is the transmission of the incident beam through the cuvette at steady illumination. From the Beer-Lambert law it follows that molar absorptivity is

$$\epsilon(\lambda) = \frac{A(\lambda)}{cl} \tag{2.1}$$

2.1.2 Emission processes in molecules

Immediately after absorption, the excess vibrational energy of the molecule is transferred to surrounding molecules (figure 2.2 step (b)). This relaxation process is very rapid, in the range of 10^{-12}s, which is the average time between collisions for molecules in the liquid phase at room temperature.

In a solution of dye molecules the solvent molecules distribute themselves around the dye in a way which leads to the greatest stability for the system. When the molecule undergoes electronic excitation, there is a significant change

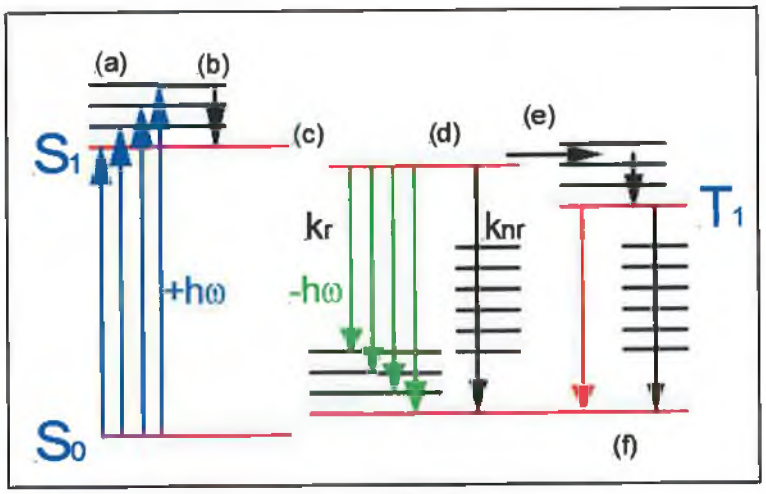

Figure 2.2: Jablonski diagram of photoluminescence processes in a molecule.

in its polarity. Because the molecule stays in the excited state much longer than the relaxation processes in the solution, the solvent molecules reorganise within $10^{-10}s$, which leads to reduction in the energy of the molecule. This is depicted in process c, figure 2.2.

In the case of fluorescence, the electron stays in the excited state S_1 typically for 10^{-8}s and then returns to its ground state releasing energy, either in the form of a photon or in the form of heat (step (d) figure 2.2). The radiation process is very fast, typically $10^{-15}s$. The molecule can still have energy from vibrational and rotational states and gain further energy due to the solution effect. The excitation of rotation and vibration modes of the molecule together with the solution effect from the absorption and emission process leads to an energy difference (or λ difference) between absorbed and emitted photon. This λ shift is called the Stokes shift and depends on the structure of the molecule, and the solution [3]. The molecule can also lose excess energy via a radiationless pathway. This can be done either by intra-molecular redistribution of the energy between the available electronic and vibrational states or by energy transfer to other molecules by collision and other mechanisms, called external quenching. The fluorescence quantum yield is defined as the ratio of the number of photons

emitted to the number of photons absorbed and is defined as

$$\phi = \frac{k_r}{k_r + k_{nr}} \tag{2.2}$$

where k_r and k_{nr} are the rates of radiation and radiationless de-excitation of the electron. The ϕ varies between 1 and 0 for highly fluorescent and non fluorescing molecules respectively.

When the source of the illumination is switched off, the fluorescence intensity starts to decrease. This decrease depends on the rate of the electron de-excitation and in many cases it can described as [1]

$$\begin{aligned} I_f(t) &= I_f(0)e^{-\frac{t}{\tau}} \\ 1/\tau &= k_r + k_{nr} \end{aligned} \tag{2.3}$$

where τ is called the fluorescence lifetime and is in range of $10^{-8}s$.

In phosphorescence, the molecule can undergo a process called inter-system crossing, where the electron in the excited state changes its spin (see figure 2.2, step (e)) and therefore its energy level. These electron energy levels, called triplet states T_1, are generally lower in energy than singlet states. The energy difference between these two states is transferred into the rotational and vibrational states of the molecule prior to relaxation. From this triplet state the electron can de-excite to the ground state by either emission of the photon or thermal de-excitation (as in the case of a singlet state). On returning to the ground state the electron has to change its spin, which is a forbidden process under the rules of quantum mechanics, and therefore the de-excitation rates k_r and k_{nr} are much lower than in the case for fluorescence. From equation (2.3) it follows that the phosphorescence lifetime is longer that fluorescence lifetime. A typical lifetime is on the order of 10^{-3}s.

2.2 Electromagnetic waves

An electromagnetic field in a vacuum can be described using an electric field $\vec{\mathcal{E}}$ and a magnetic field $\vec{\mathcal{H}}$. These field vectors, which are functions of space and time, have to satisfy Maxwell's equations. Only the sinusoidal time-harmonic electromagnetic waves with angular frequency ω will be considered here. This is

still a generalisation because any time-varying function can be described as a superposition of sinusoidal time-harmonic functions via Fourier transformation [4]. These fields can be represented in complex notation as

$$\vec{E}_c(\vec{r},t) = \vec{E}(\vec{r})e^{-i\omega t}, \qquad \vec{H}_c(\vec{r},t) = \vec{H}(\vec{r})e^{-i\omega t} \tag{2.4}$$

where $\vec{E}$ and $\vec{H}$ are complex vectors independent of time and $\vec{E}_c, \vec{H}_c$ vectors are related to the real fields by

$$\vec{\mathcal{E}}(\vec{r},t) = \mathrm{Re}\{\vec{E}_c(\vec{r},t)\}, \qquad \vec{\mathcal{H}}(\vec{r},t) = \mathrm{Re}\{\vec{H}_c(\vec{r},t)\} \tag{2.5}$$

Because Maxwell's equations are a linear system of partial differential equations, Maxwell's equations are solved for complex vectors $\vec{E}_c, \vec{H}_c$ and then the equations (2.5) are used to obtain $\vec{\mathcal{E}}$ and $\vec{\mathcal{H}}$.

If the electromagnetic field propagates in a material, the interaction of the electromagnetic wave with matter has to be included. Herein it is assumed the material is isotropic, homogenous, linear and non-magnetic without any free charges and free currents. In SI units Maxwell's equations in differential form may be written

$$\nabla \cdot (\varepsilon\vec{E}) = 0 \tag{2.6}$$

$$\nabla \times \vec{E} = i\omega\mu\vec{H} \tag{2.7}$$

$$\nabla \cdot (\vec{H}) = 0 \tag{2.8}$$

$$\nabla \times \vec{H} = -i\omega\varepsilon\vec{E} \tag{2.9}$$

where $\mu = \mu_r\mu_0$ is the permeability (for non-magnetic materials $\mu_r = 1$) and $\varepsilon = \varepsilon_r\varepsilon_o$ is the permittivity. The relative permittivity ε_r represents the response of bound (polarisation) and free charges (conductivity) in a material to the electromagnetic field. Generally, ε_r is a function of ω and has the complex value $\varepsilon_r(\omega) = \varepsilon_1(\omega) + i\varepsilon_2(\omega)$. Relative permittivity is discussed further in section 2.3.1.

From Maxwell's equations it is possible to derive the vector wave equation for both the electric and magnetic fields. The curl operator is applied to equations (2.7) and (2.9), and a vector identity is used for double curl. The resulting equations, also called Hemholtz equations, are written in the form

$$\nabla^2\vec{E} + \omega^2\varepsilon\mu\vec{E} = 0, \qquad \nabla^2\vec{H} + \omega^2\varepsilon\mu\vec{H} = 0 \tag{2.10}$$

An electromagnetic field has an energy which can travel through space. For a harmonic oscillating field with $(\vec{E}, \vec{H})$, the time-averaged Poynting vector can be defined as

$$\vec{\mathcal{S}} = \frac{1}{2}\mathrm{Re}\{\vec{E} \times \vec{H}^*\} \tag{2.11}$$

which specifies the magnitude and direction of the rate of transfer of electromagnetic energy at all points of space.

In the next section, two electromagnetic waves solutions necessary for further discussions, are presented.

2.2.1 Plane wave

The first solution is a homogeneous plane wave which can be written in the form

$$\vec{E}_c(\vec{r}, t) = \vec{E}_0 e^{i\vec{k}\cdot\vec{r} - i\omega t}, \qquad \vec{H}_c(\vec{r}, t) = \vec{H}_0 e^{i\vec{k}\cdot\vec{r} - i\omega t} \tag{2.12}$$

where $\vec{k}$ is the complex wave vector defined as $\vec{k} = (k' + ik'')\hat{k}$, where k' and k" are real numbers and $\hat{k}$ is a normal real vector. The equation $\hat{k} \cdot \vec{r} = constant$ defines the plane of constant phase and amplitude. The plane of constant phase propagates with a phase velocity $v = \omega/k'$ and its wavelength is $\lambda = 2\pi/k'$. There is a restriction on the wave vector $\vec{k}$. Substituting eq. (2.12) in Hemholtz eq. (2.10), a dispersion relation is obtained

$$\vec{k} \cdot \vec{k} = \omega^2 \varepsilon \mu \tag{2.13}$$
$$k' + ik'' = \omega\sqrt{\varepsilon_0 \mu_0}\sqrt{\varepsilon_r \mu_r} = k_0 N$$

where $k_0 = \omega\sqrt{\varepsilon_0 \mu_0}$ is defined as the size of wave vector in vacuum and $N = \sqrt{\varepsilon_r \mu_r} = n' + in''$ is the complex refractive index.

Another restriction on vectors $\vec{k}, \vec{E}_0, \vec{H}_0$ follows substituting plane wave 2.12 in Maxwell's equations (2.6) and (2.8)

$$\vec{k} \cdot \vec{E}_0 = \vec{k} \cdot \vec{H}_0 = \vec{H}_0 \cdot \vec{E}_0 = 0 \tag{2.14}$$

These equations indicate that vectors $\vec{k}, \vec{E}_0, \vec{H}_0$ have to be perpendicular to each other.

2.2.2 Vector spherical harmonics

Solution of Maxwell's equations in spherical co-ordinates $\{r, \theta, \phi\}$, which are needed in further analysis in section 2.3.2, are known as vector spherical harmonics. They can be constructed from the solution of the scalar Hemholtz equation

$$\nabla^2\psi + k^2\psi = 0 \tag{2.15}$$

where $k = \omega^2\varepsilon\mu$. It can be is expressed as [5]

$$\psi^{(i)}_{\substack{e\\o}mn} = \begin{matrix}\cos\\ \sin\end{matrix}(m\phi)P^m_n(\cos\theta)z_n(kr) \tag{2.16}$$

where $P^m_n(\cos\theta)$ is the associated Legendre function of the first kind (n=0,1,...; m=0,,n) and index (i) is associated with the choice of z_n functions, which are spherical Bessel functions (i=1,,4; $j_n, y_n, h^{(1)}_n, h^{(2)}_n$).

Next, vector spherical functions $\vec{M}^{(i)}_{\substack{e\\o}mn}, \vec{N}^{(i)}_{\substack{e\\o}mn}$ are defined as

$$\vec{M}^{(i)}_{\substack{e\\o}mn} = \nabla \times (\vec{r}\psi^{(i)}_{\substack{e\\o}mn}), \qquad \vec{N}^{(i)}_{\substack{e\\o}mn} = \frac{\nabla \times \vec{M}^{(i)}_{\substack{e\\o}mn}}{k} \tag{2.17}$$

These functions expressed in term of elementary functions are given in Appendix A. These functions are divergence free

$$\nabla \cdot \vec{M}^{(i)}_{\substack{e\\o}mn} = 0, \qquad \nabla \cdot \vec{N}^{(i)}_{\substack{e\\o}mn} = 0 \tag{2.18}$$

and as it follows from [6], they are solutions of the vector Hemholtz equation 2.10. By applying the curl operator on $\vec{N}^{(i)}_{\substack{e\\o}mn}$ and knowing that $\vec{M}_{\substack{e\\o}mn}$ is divergence free, the solution of the vector Hemholtz equation, $\vec{M}^{(i)}_{\substack{e\\o}mn}$ can be expressed as

$$\vec{M}^{(i)}_{\substack{e\\o}mn} = \frac{\nabla \times \vec{N}^{(i)}_{\substack{e\\o}mn}}{k} \tag{2.19}$$

Since the vector spherical harmonics which satisfy the vector wave equations are divergence free and since the curl of one spherical function is proportional to the other spherical function, the vector spherical harmonics are solutions of Maxwell's equations (2.6) - (2.9).

Moreover, the set of vector spherical functions is complete [7] (for each set i=1,2 or i=3,4 of bessel functions). This means that any solution of electromagnetic waves can be expanded into these functions

$$\vec{E} = \sum_{n=0}^{\infty}\sum_{m=0}^{n}\sum_{i=1,3}^{2,4}(B^{(i)}_{emn}\vec{M}^{(i)}_{emn} + B^{(i)}_{omn}\vec{M}^{(i)}_{omn} + A^{(i)}_{emn}\vec{N}^{(i)}_{emn} + A^{(i)}_{omn}\vec{N}^{(i)}_{omn}) \tag{2.20}$$

Because all vector spherical harmonics are orthogonal [5] the coefficients in the expansion are of the form

$$B_{emn}^{(i)} = \frac{\int_0^2 \pi \int_0^\pi \vec{E} \cdot \vec{M}_{emn}^{(i)} \sin\theta d\theta d\phi}{\int_0^2 \pi \int_0^\pi |\vec{M}_{emn}^{(i)}|^2 \sin\theta d\theta d\phi} \tag{2.21}$$

with similar expressions for $B_{omn}^{(i)}, A_{emn}^{(i)}, A_{omn}^{(i)}$. A magnetic field is obtained by substituting the electric field in equation 2.7 and using the relationship between $\vec{M}_{\substack{e\\o}mn}^{(i)}, \vec{N}_{\substack{e\\o}mn}^{(i)}$

$$\vec{H} = -\frac{ik}{\omega\mu} \sum_{n=0}^{\infty} \sum_{m=0}^{n} \sum_{i=1,3}^{2,4} (B_{emn}^{(i)} \vec{N}_{emn}^{(i)} + B_{omn}^{(i)} \vec{N}_{omn}^{(i)} + A_{emn}^{(i)} \vec{M}_{emn}^{(i)} + A_{omn}^{(i)} \vec{M}_{omn}^{(i)}) \tag{2.22}$$

2.3 Metal nanoparticles

2.3.1 Optical properties of metals

In this section the optical properties of metals are reviewed. At first, the dielectric constant of metals is defined and, following this, a model describing the microscopic interaction of light with the metal is presented.

When an electromagnetic field is present in matter the electric and magnetic components of that field act on the atoms in the matter. Matter consists of electrically charged particles; the electric field acts on them with a force equal to $\vec{F} = q \cdot \vec{E}$ and will induce polarisation $\vec{P}$ in the matter. The matter is considered linear and homogenously isotropic if the relationship between polarisation $\vec{P}$ and electric vector $\vec{E}$ is

$$\vec{P}(\omega) = \varepsilon_0(\varepsilon_r(\omega) - 1)\vec{E}(\omega) \tag{2.23}$$

where ε_0 is the permittivity of free space and ε_r is the relative permittivity of the medium. If the electric field does not affect the polarisation then $\varepsilon_r = 1$, as is the case for a vacuum. The electromagnetic field in matter is changed by the induced dipole in that it acts as a distribution of charge of density $-\nabla \cdot \vec{P}$ and an equivalent distribution of current density $\frac{\partial \vec{P}}{\partial t}$ ([6] page 12), which are implemented in the Maxwell's equations (2.6) - (2.9). Noble metals do not exhibit any magnetic effects (the magnetic field does not induce any magnetisation in the matter) so the relative permeability is the same as in a vacuum ($\mu_r = 1$).

The dielectric constant of metals can be measured experimentally. The common methods are reflectometry [8] and ellipsometry [9]. Both methods analyse the reflected beams from the material. As an example, the dielectric contants of silver and gold are presented in Figure 2.3 (data taken from ref. [10]).

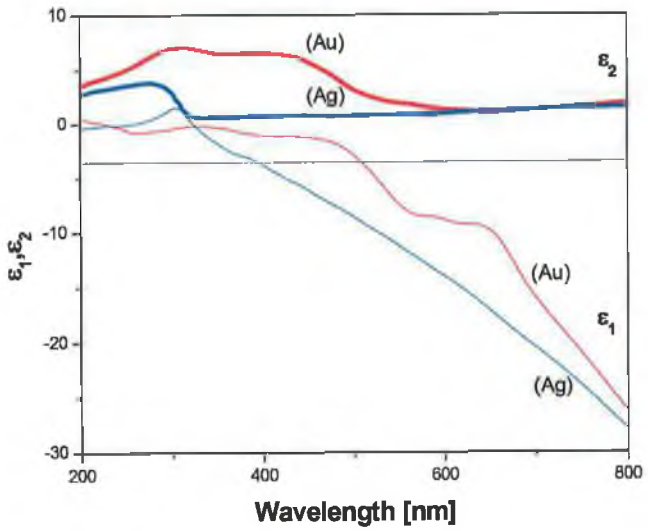

Figure 2.3: Real (ε_1) and imaginary (ε_2) part of dielectric constant for gold and silver. The horizontal line represents ($\varepsilon_1 = -2\varepsilon^{water}$).

The dielectric constant can not be completely arbitrary. Because of the linear dependence of $\vec{P}$ on $\vec{E}$ and due to the principle of causality, the real and imaginary part of dielectric constant have to obey the Kramers-Kronig relationship ([5], page 69). These equations state that if the imaginary part of the dielectric constant is known for the whole spectral range then the real part is already given and vice versa.

Metals are sometimes defined in terms of their conductivity σ rather than their dielectric constant. Conductivity is a quantity which appears in Ohm's law describing the dependence between the conduction current J and the electric field. In most metals $J(\omega) = \sigma(\omega)E(\omega)$. The conductivity and the dielectric constant are not independent and their relationship can be expressed as ([4], page 69)

$$\varepsilon_r(\omega) = 1 + i\frac{\sigma(\omega)}{\omega\varepsilon_0} \tag{2.24}$$

Dielectric constants of metals

To explain the profile of the dielectric constants of metals,a detailed look at the structure of matter is needed. Most metallic materials consist of atoms ordered in a periodic structure (close packed), where the core electrons are bound to the atom's cores and the outer electrons are shared by all atoms. These outer electrons can be considered as a free electron gas and can be described by the Drude model ([5], page 253). In this model an electromagnetic field acts on the electron with a force $e\vec{E}e^{-i\omega t}$ (the magnetic force can be neglected) and the electron is damped by collisions with a force linear to its speed. Therefore, the motion of the electron can be described with the equation

$$\vec{x}'' + \gamma\vec{x}' = \frac{e}{m^*}\vec{E}e^{-i\omega t} \tag{2.25}$$

where m* is an effective mass of the electron and γ is damping constant. This motion will cause a polarisation of the material ($\vec{P} = \rho_e e\vec{x}$, where ρ_e is the density of free electrons) Solving the differential equation above and using equation (2.23) will give the dielectric constant of a metal due to the free electrons, $\varepsilon^f = \varepsilon_1 + i\varepsilon_2$ as

$$\varepsilon_1 = 1 - \frac{\omega_p^2}{\omega^2} \tag{2.26}$$

$$\varepsilon_2 = \frac{\omega_p^2\gamma}{\omega^3} \qquad (\omega >> \gamma) \tag{2.27}$$

where ω_p is called plasma frequency and is given by ${\omega_p}^2 = \rho_e e^2/m^*\varepsilon_0$. The dependence of the dielectric constant on ω agrees with experimental values for metals for lower energy.

For an electromagnetic field with higher energy (shorter wavelength) electrons from the deeper electron bands can be excited (called inter-band absorption) and the excitation will modify the dielectric constant to give an additional term, $\delta\varepsilon$ where

$$\varepsilon_r = \varepsilon^f + \delta\varepsilon^b \tag{2.28}$$

This response of the bound electron to the electromagnetic field can be described with the Lorenz model. In this model, the bound electron is regarded as an harmonic oscillator in the presence of the electric field, with spring constant K. The equation of motion of the electron can be written as

$$\vec{x}'' + \gamma\vec{x}' + \omega_0^2\vec{x} = \frac{e}{m^*}\vec{E}e^{-i\omega t} \tag{2.29}$$

where $\omega_0^2 = K/m^*$ and $\omega_o^2\hbar$ is approximately the energy of bound electrons when they start to be excited. As for free electrons, the motion will give rise to a polarisation of the matter. Therefore, on solving this differential equation the additional term in the dielectric constant can be written (in complex form) as

$$\delta\varepsilon = \frac{\omega_p^2}{\omega_0^2 - \omega^2 - i\gamma\omega} \tag{2.30}$$

Contributions of these different electrons to the dielectric constant are easy to see in a material such as silver. The decomposition of its dielectric constant due to contribution from free and bound electrons is described with equations 2.26 and 2.30 and it is demonstrated in figure 2.4.

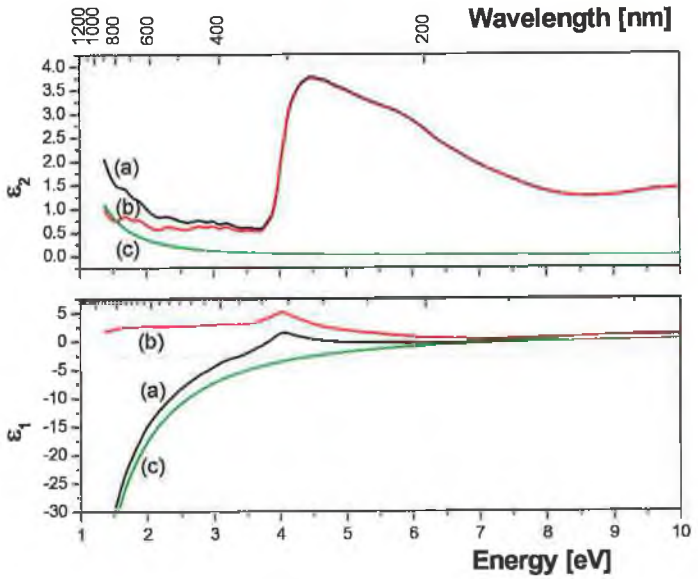

Figure 2.4: Decomposition of dielectric constant of silver (curve a) on contribution from free (curve c) and bound (curve b) electrons. top - real part, bottom - imaginary part. The horizontal line represents ($\varepsilon_1 = -2\varepsilon^{water}$)

The experimentally obtained dielectric constant is generally measured on macroscopic objects and is therefore not exactly valid for nanosized objects. With the decreasing size of the object the surface will start to influence the dielectric constant. One of the reasons for this is due to the limited electron mean-free-path. The damping of the electrons in the Drude model is given by the constant γ

in equation (2.26). This damping is introduced by collisions with other electrons, phonons, etc. If dissipation of energy is mostly by electrons close to the Fermi level (electrons with the highest energy), the damping constant can be written as $\gamma = v_F/l_{\text{inf}}$, where v_F is the fermi velocity of the electrons ($v_F \sim 10^6 m/s$) and l_{inf} is mean free path between two electron collisions. For example, silver has $l_{\text{inf}} = 52nm$ at room temperature (from [11], page 22). If the object of size R is smaller than the mean free path, an additional scattering of the electrons with the surface of the object is added. This can be expressed in the damping constant as ([11])

$$\gamma = \gamma_{\text{inf}} + \Delta\gamma(R) = \frac{v_F}{l_{\text{inf}}} + \frac{4}{3}\frac{v_F}{R} \tag{2.31}$$

Using this modified damping constant and equation (2.26) will give the expression for the size dependent imaginary part of dielectric function

$$\varepsilon_2(\omega, R) = \varepsilon_{2,bulk}(\omega) + \frac{3}{4}\frac{\omega_p^2}{\omega^3}\frac{v_F}{R} \tag{2.32}$$

2.3.2 Localised Surface Plasmon Resonance

In this section, Localised Surface Plasmon Resonance (LSPR) of a metal nanoparticle is defined. At first, an approximate solution of scattering of light by a sphere is presented and the resonance effects are then related to the LSPR. This is followed by an exact electrodynamic solution of the problem for spherical nanoparticles and for spherical nanoparticles with shells. At the end of this section, the results are applied to non-spherical nanoparticles.

Scattering of light by spheres

Let us consider a particle with relative dielectric constant ε^1 located at an origin in a coordinative system and embedded in a non-absorbing medium with dielectric constant ε^m. The particle is illuminated with an incident beam described by electric and magnetic vectors $(\vec{E}_i, \vec{H}_i)$. Next, the electromagnetic fields inside and outside the particle are defined. The field generated inside the particle is denoted by $(\vec{E}_1, \vec{H}_1)$. The electromagnetic field outside the particle $(\vec{E}_2, \vec{H}_2)$ is a superposition of the incident field and the scattered field $(\vec{E}_s, \vec{H}_s)$ induced by the incident beam (see figure 2.5).

$$\vec{E}_2 = \vec{E}_i + \vec{E}_s \qquad \vec{H}_2 = \vec{H}_i + \vec{H}_s \tag{2.33}$$

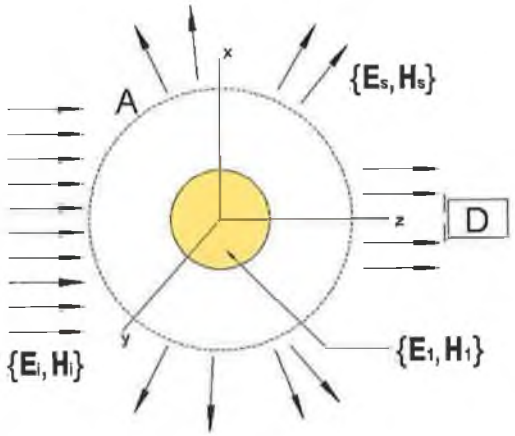

Figure 2.5: A particle at the origin is illuminated with the incident field $\vec{E}_i, \vec{H}_i$. The field inside the sphere is $\vec{E}_1, \vec{H}_1$ and the field outside the particle consists of scattered field $\vec{E}_s, \vec{H}_s$ and the incident field. Surface A represents the surface of an imaginary sphere with $r \rightarrow \infty$ and D is a detector.

The electromagnetic fields have to be a solution of the wave equation (2.10) and have to fulfill the boundary conditions. The derivation of the electromagnetic field inside and outside for a specific particle is content of the following sections, but before this, the relationship between the scattered field and absorption spectra will be highlighted.

Extinction cross section

Let us construct an imaginary sphere of radius r around the particle (see figure 2.5).While the electromagnetic field at the surface A is given $(\vec{E}_2, \vec{H}_2)$, the electromagnetic energy crossing the surface A of this sphere can be written as

$$W_a = -\int_A \vec{S}_2 \cdot \hat{r} dA \tag{2.34}$$

and is the energy rate absorbed in the particle ($W_a > 0$). Using equations (2.11,2.33), the absorbed energy rate is written as the sum of three terms: $W_a = W_i - W_s + W_{ext}$, where

$$\begin{aligned} W_i &= -\int_A \frac{1}{2}\mathrm{Re}\{\vec{E}_i \times \vec{H}_i^*\} \cdot \hat{r} dA = -\int_A \vec{S}_i \cdot \hat{r} dA \\ W_s &= \int_A \frac{1}{2}\mathrm{Re}\{\vec{E}_s \times \vec{H}_s^*\} \cdot \hat{r} dA = \int_A \vec{S}_s \cdot \hat{r} dA \end{aligned} \tag{2.35}$$

$$W_{ext} = -\int_A \frac{1}{2}\mathrm{Re}\{\vec{E}_i \times \vec{H}_s^* + \vec{E}_s \times \vec{H}_i^*\} \cdot \hat{r} dA = -\int_A \vec{S}_{ext} \cdot \hat{r} dA$$

The term W_i is equal to zero, when the embedding medium is not absorbing. The term W_s is the rate at which energy is scattered by the particle. Therefore, W_{ext} is the sum of the energy absorption rate and the energy scattering rate

$$W_{ext} = W_a + W_s \tag{2.36}$$

Suppose a detector is placed behind the particle (see figure 2.5). The term W_{ext} represents the difference of energy rate in the cases where the particle is and is not present. These energy rates can be divided by the irradiance of the incident wave $I_i = |\vec{S}_i|$ to define the extinction cross section $C_{ext} = W_{ext}/I_i$, the absorption cross section $C_{abs} = W_a/I_i$ and the scattering cross section $C_{sca} = W_s/I_i$. From the equation above it follows that

$$C_{ext} = C_{abs} + C_{sca} \tag{2.37}$$

These cross sections have dimensions of area, and in terms of geometrical optics, they can be interpreted as an area of shadow, which is cast on the detector. The cross section is connected with the experimentally measured absorption spectra of the particles. If a solution of nanoparticles with density ρ (where the density is low enough that multiple scattering is avoided) within a cuvette with path-length h is illuminated with incident irradiance I_i then the detected irradiance is attenuated ([5] page 79) as

$$I_t = I_i e^{-\rho C_{ext} h} \tag{2.38}$$

In spectroscopic measurements, it is common to measure absorbance A, which is defined as $A = \log_{10}(I_t/I_i)$. Therefore, the absorbance is related to the extinction cross section as

$$A = 0.434 \rho C_{ext} h \tag{2.39}$$

Cross sections of small spheres

To get the exact solution of the problem formulated above, the wave equation (2.10) together with boundary conditions must be solved. In this part some approximations will be used to tackle the problem. The first restriction is on the size (a) of the nanoparticle. If $a << \lambda$, then the incident electromagnetic wave

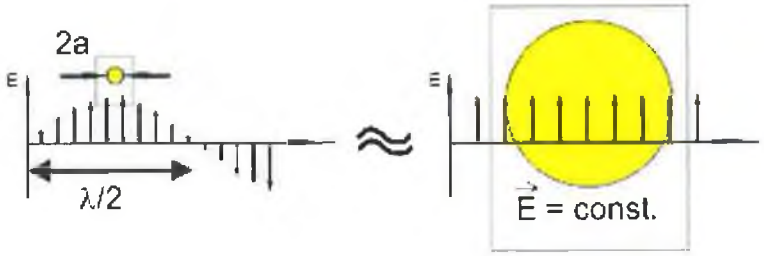

Figure 2.6: Graphical explanation of quasi-static approximation used for scattering of light by a small sphere

can be substituted by a uniform electric field $\vec{E}_0 = E_0\hat{x}$ (see figure 2.6). Next, the problem will be solved for a static field and then the solution will be generalised for a time-varying field. The Laplace equation for a scalar potential with corresponding boundary conditions, describing an electrostatic field, is solved and it leads to the expression for electric field ([12], page 72) inside the sphere $\vec{E}_{int}$ and outside the sphere $\vec{E}_{ext}$.

$$\vec{E}_{int} = \frac{3\varepsilon^m}{\varepsilon^1 + 2\varepsilon^m}\vec{E}_0 \tag{2.40}$$

$$\vec{E}_{ext} = \vec{E}_0 + \frac{1}{r^5}\left[3(\vec{p}\cdot\vec{r})\vec{r} - \vec{p}r^2\right] \tag{2.41}$$

$$\vec{p} = 4\pi\varepsilon^m a^3 \frac{\varepsilon^1 - \varepsilon^m}{\varepsilon^1 + 2\varepsilon^m}\vec{E}_0 \tag{2.42}$$

From these equations it follows that the electric field inside the sphere is uniform and in the direction of the external field $\vec{E}_0$. The equation for the electric field outside the sphere is a composition of two terms. The first one is the external field $\vec{E}_0$ and the second is identical with the electric field of a dipole (see [12] page 41) with the dipole $\vec{p}$ induced by the external field $vecE_0$. This means that the dielectric sphere can be substituted with an electric dipole $\vec{p}$ placed in the center of the sphere.

Now, the solution will be generalised for a time varying field. If the particle is illuminated with an x-plane wave $(E_0 \exp(ikz - i\omega t)\hat{x})$ then the particle behaves as a dipole with

$$\vec{p} = 4\pi\varepsilon^m a^3 g(\omega)\vec{E}_0 e^{-i\omega t} \tag{2.43}$$

$$g(\omega) = \frac{\varepsilon^1(\omega) - \varepsilon^m}{\varepsilon^1(\omega) + 2\varepsilon^m} \tag{2.44}$$

Therefore the dipole radiates an electromagnetic field $(\vec{E}_s, \vec{H}_s)$ ([6], page 435) and using the equation for the extinction cross section leads to the expression

$$C_{ext} = \pi a^2 4ak\mathrm{Im}\{g\} \tag{2.45}$$

Because of the use of the nanoparticles in connection with fluorescence, another useful quantity is the square of the absolute value of the electric field outside the nanoparticle. The expression for $\vec{E}_s$ is quite complex, but for small distances ($r << \lambda$) from the nanoparticle it is identical to the static field of a dipole ([12], page 241). Therefore, $\vec{E}_{ext}$ in equation (2.41) can be used to compute the quantity. If α is defined as the angle between the position vector $\hat{r}$ and $\hat{x}$, then after some manipulation, the following expression is obtained:

$$|\vec{E}_2(r,\alpha)|^2 = E_0^2 \left(3\frac{a^3}{r^3}\cos^2\alpha(|g|^2 + 2\mathrm{Re}\{g\}) + \left|1 - g\frac{a^3}{r^3}\right|^2 \right) \tag{2.46}$$

Surface resonance modes in the nanoparticle

The electric field inside and outside the nanoparticle (equation (2.41)), as well as the extinction cross section of the nanoparticle (equation (2.45)), show resonance behavior whenever the denominator in $g(\omega)$ (equation (2.44)) goes to a minimum:

$$(\varepsilon_1^1 + 2\varepsilon^m)^2 + (\varepsilon_2^1)^2 = Minimum \tag{2.47}$$

If the imaginary part of dielectric constant of the particle is small or slowly varying with the frequency of light then the resonance condition can be rewritten as

$$\varepsilon_1^1 = -2\varepsilon^m \tag{2.48}$$

In section 2.3.1, dealing with the dielectric constant of metals, it was shown that the real part of the dielectric constant is negative and therefore the resonance condition (2.48) can be fulfilled. Moreover, for noble metals the resonance occurs at frequencies which correspond to visible light. As an example, the extinction cross section of gold and silver nanoparticles of the same radius of 5nm in water are presented in figure 2.7. The resonance peaks for metal nanoparticles are clearly visible. For comparison, the absorbance of a silver slab with thickness of

10nm is presented in figure 2.7 as well. It is clear that the absorbance does not show any resonance peak (the increase at short wavelength is due to absorption by bound electrons).

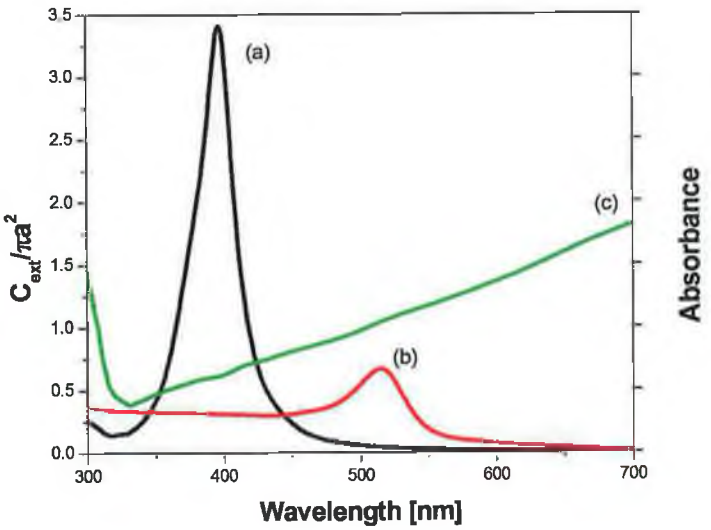

Figure 2.7: Normalised extinction cross section of (a) silver and (b) gold nanoparticles of 5nm radius in water. The plasmon resonance peaks are clearly visible. For a comparison, absorption spectra of a silver slab ,perpendicularly illuminated, of 10nm thickness is presented as well (curve (c)). This curve does not exhibit any peak associated with the plasmon resonance.

Relationship between the resonance and the plasmon modes

The condition for the resonance behavior of the cross sections follows from electromagnetic theory. Any small particle made from a material with dielectric constant equal =-2 at wavelength λ will exhibit the resonance behavior at wavelength λ in vacuum (equation 2.48). However, the origin of the resonance is quite different for a silver nanoparticle illuminated with 390nm compared with that of a magnesium oxide particle with illumination at $17\mu m$.

To explain the origin of the resonance in a metal nanoparticle, one has a to have closer look at the dielectric constant. The dielectric constant of a metal

is governed mainly by the free electrons, as was explained in section 2.3.1. If we restrict the expression for the dielectric constant of metals only to the Drude term (2.26) (as it is case of alkali metals), the resonance condition (2.48) occurs at angular frequency

$$\omega = \frac{\omega_p}{\sqrt{1 + 2\varepsilon^m}} \tag{2.49}$$

It was shown that the electric field inside the particle is uniform (eq. 2.40) and that it changes periodically with the angular frequency ω. The electric field accelerates all the electrons in the particle simultaneously and therefore excites collective oscillations of conduction electrons. This motion has an analogy with a simple oscillator driven by a periodic force. The force is the electric field acting on the electrons and the restoring force of the harmonic oscillator are the polarization charges on the surface of the sphere (see figure 2.8).

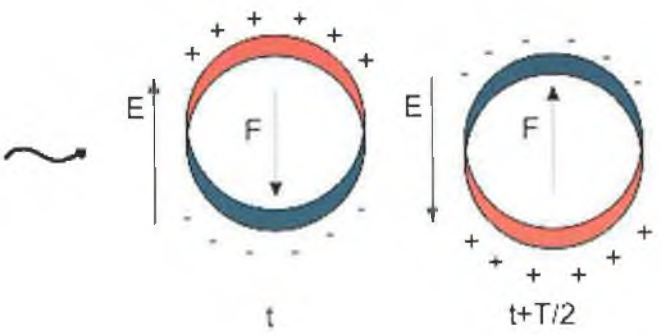

Figure 2.8: The motion of electrons in metal nanoparticle has an analogy with a harmonic oscillator driven by a periodic force. The electric field ($\vec{E}$) accelerates the electron and the restoring force ($\vec{F}$) is given by the polarization charges induced by the motion of the electrons

Collective excitation of the conduction electrons can be observed in bulk metal material. At the frequency $\omega = \omega_p$ the electrons form longitudinal waves in the material ([13], page 278) and the energy quantum of this oscillation is called a plasmon. This plasma oscillation can not be excited by optical excitation, as the electromagnetic field is transverse and therefore high energy electrons are used to excite and study these oscillations (called Electron energy loss spectroscopy). Similarly, a plasmon can be excited at a planar metal surface ($\omega = \omega_p/\sqrt{2}$) or

thin metal film. These surface plasmon modes can be excited by the light [14] under special conditions (angle of incidence and the embedded medium) or by electrons [15]. In analogy to this, the resonance behavior in the metal nanoparticle, in which electrons collectively oscillate, is called localised surface plasmon resonance (LSPR).

Properties of the LSPR

The description of LSPR will be restricted to gold and silver nanoparticles as such nanoparticles were the main focus of the research reported here. As can be seen from figure 2.7, the position of the resonances for 5nm gold and silver nanoparticles are $\lambda = 520nm$ and $\lambda = 390nm$, respectively. As was described earlier, the position is given by equation (2.48) and by the dielectric constant (see figure 2.3, the horizontal line represents the resonance condition (equation 2.48)). These positions are shifted to a longer wavelength compared to the resonance condition for free electrons (equation 2.49). This discrepancy is caused by the influence of bound electrons on the dielectric constant. For example, for silver nanoparticles the bound electrons shift the resonance condition more than 100nm to the longer wavelength (see figure 2.4). The same effect is observed in gold as well. Therefore, plasmon resonance in gold and silver nanoparticles is given by collective oscillation of free and bound electrons.

Further, the silver nanoparticle has a bigger value of the extinction cross section than a gold nanoparticle. The height of the resonance peak is given by the imaginary part of the dielectric constant of the metal. The smaller it is, the smaller the value of the denominator in $g(\omega)$ (equation 2.44) and therefore the nanoparticle exhibits stronger resonance. Indeed, ε_2^{Au} at resonance has a higher value than ε_2^{Ag} at resonance as can be seen from the figure 2.3. The reason for this is that, in the case of the silver, the absorption of the bound electrons (see section 2.3.1) starts at a shorter wavelength ($\lambda = 300nm$) than the wavelength of the resonance, whereas in the case of gold the absorption of the bound electrons starts at a wavelength ($\lambda = 600nm$) longer than the resonance wavelength (see figure 2.3).

As was shown in section 2.3.1, the dielectric constant changes with the size of the nanoparticles. If it is smaller than the electron free mean path then the dielec-

tric constant increases with decreasing size of the nanoparticle (see eq. (2.32)). Therefore, the plasmon resonance is difficult to observe in nanoparticles smaller than few nanometers. Note, this effect does not follow from the electromagnetic theory and therefore it is called intrinsic.

The position of the resonance depends on the embedded medium as follows from the equation 2.48. Because the real part of the dielectric constant of gold and silver decrease as a function of wavelength for $\varepsilon_1 > 2$ (see figure 2.3), the resonance shifts to a longer wavelength for the embedded medium with higher dielectric constant.

Another important aspect is the local field around the nanoparticle. Using equation (2.46), the absolute value of the local field ($|\vec{E}_2/E_0|^2$) around a 5nm radius silver nanoparticle illuminated with light of $\lambda = 400nm$ is presented in figure 2.9. From the figure it follows that a high electric field is formed around the nanoparticle with its maximal value at the surface of the sphere along the polarisation axis ($\alpha = 0, \pi$). In the case of resonance, the value of $|g(\omega)|$ is bigger than 1, and therefore a simplification of equation (2.46) leads to $|\vec{E}_2/E_0|^2_{max} \cong 4|g|^2$ and which quickly drops with increasing distance from the nanoparticle as $|\vec{E}_2/E_0|^2 \propto 1/r^3$.

LSPR in a sphere of arbitrary size

In the preceding section, the concept of the localised surface plasmon resonance was explained by scattering of the light by small particles in the quasi-static limit. The general solution for an arbitrary size particle can be found as well and it was first given by Mie [16]. This section will briefly describe the ideas behind the theory and will show the results important to plasmon resonance.

As in the preceding section, a particle is placed at the origin and illuminated with a x-polarised plane wave (equation (2.12)) propagating in the z-direction ($\vec{E}_i, \vec{H}_i$) (see figure 2.5). The incident field induces a field inside the particle ($\vec{E}_1, \vec{H}_1$) and a field outside the particle ($\vec{E}_2, \vec{H}_2$), which is a composition of the incident and scattered field (eq. (2.33)).

This plane wave can be expressed as (eq. (2.12))

$$\vec{E}_i = E_0 e^{irk\cos\theta}\hat{x} \tag{2.50}$$

Because of the spherical symmetry of the problem, it is more convenient to use

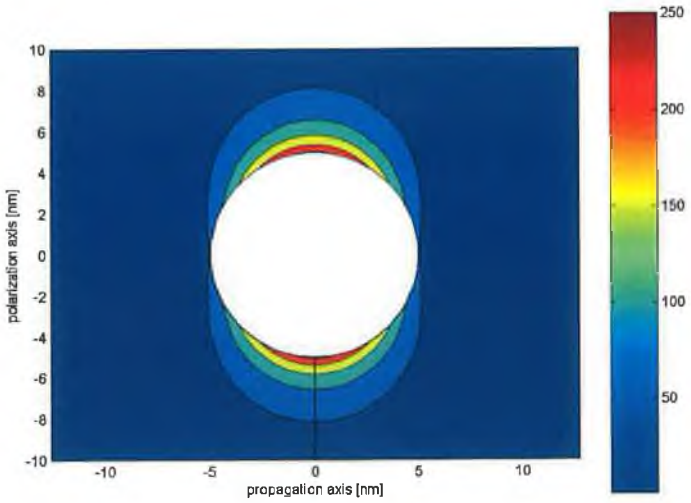

Figure 2.9: Square of the absolute value of electric field around silver nanoparticle radius 5nm calculated by the equation 2.41 for illumination wavelength $\lambda = 400nm$. $|\vec{E}_2/E_0|^2_{max} \simeq 4|g|^2 = 250$

vector spherical harmonics. Using the equation for expansion of any field in vector spherical harmonics and for their coefficients (equations (2.20,2.21)), the plane wave can be expanded as [5]

$$\vec{E}_i = E_0 \sum_{n=1}^{\infty} i^n \frac{2n+1}{n(n+1)} (\vec{M}^{(1)}_{o1n} - i\vec{N}^{(1)}_{e1n}) \tag{2.51}$$

The magnetic component of the field is obtained by equation (2.7). As well as the incident field, the scattered field ($\vec{E}_s$) outside the nanoparticle and the inner field ($\vec{E}_1$) inside the nanoparticle will be expanded into the vector spherical harmonics with unknown coefficients of the expansion as in equations (2.20,2.21). These fields are not independent and have to fulfill the boundary condition on the surface of the sphere [5]

$$(\vec{E}_i + \vec{E}_s - \vec{E}_1) \times \hat{r} = (\vec{H}_i + \vec{H}_s - \vec{H}_1) \times \hat{r} = 0 \tag{2.52}$$

The boundary condition is four linear equations for unknown expansion coefficients of the inner and scattered field. Now, because of the spherical symmetry of the nanoparticle, the equations (2.52) can be integrated over the angles θ, ϕ. From

the orthogonality of the vector spherical harmonics and expansion of the incident field it follows that unknown expansion coefficients of the inner and scattered field are non-zero only for $m = 1$. The boundary condition in equation (2.52) then leads to the four linear equations for two unknown expansion coefficients of the inner field and two unknown expansion coefficients of the scattered field for a given n. Solving these linear equation leads to the expression for the scattered field

$$\vec{E}_s = E_0 \sum_{n=1}^{\infty} i^n \frac{2n+1}{n(n+1)} (ia_n \vec{N}^{(3)}_{e1n} - b_n \vec{M}^{(3)}_{o1n}) \tag{2.53}$$

with the scattering coefficients of the spherical harmonics a_n and b_n equal to

$$a_n = \frac{m\psi_n(mx)\psi_n'(x) - \psi_n(x)\psi_n'(mx)}{m\psi_n(mx)\xi_n'(x) - \xi_n(x)\psi_n'(mx)} \tag{2.54}$$

$$b_n = \frac{\psi_n(mx)\psi_n'(x) - m\psi_n(x)\psi_n'(mx)}{\psi_n(mx)\xi_n'(x) - m\xi_n(x)\psi_n'(mx)} \tag{2.55}$$

where ψ and ξ are Riccati-Bessel functions (see Appendix B, equation B.5) , x is the size parameter and m is the relative refractive index

$$x = ka = \frac{2\pi N_m a}{\lambda} \qquad m = \frac{N_1}{N_m} = \sqrt{\frac{\varepsilon^1}{\varepsilon^m}}. \tag{2.56}$$

Because the distribution of the electric field outside the nanoparticle was obtained, the cross section can be obtained using the expression in equation (2.35)

$$C_{sca} = \frac{2\pi}{k^2} \sum_{n=1}^{\infty} (2n+1)(|a_n|^2 + |b_n|^2) \tag{2.57}$$

$$C_{ext} = \frac{2\pi}{k^2} \sum_{n=1}^{\infty} (2n+1)\mathrm{Re}\{a_n + b_n\} \tag{2.58}$$

As an example, extinction, absorption and scattering cross sections of a silver nanoparticle with a different radius immersed in water is presented in figure 2.10. The extinction cross section of a 5nm particle is entirely caused by absorption, so the particle scatters very little. The peak in the spectrum is given by the increase of the a_1 expansion coefficient of the scattered field; all other expansion coefficients have very low values. For small particles ($a \ll \lambda$), the coefficient can be approximated to $a_1 \simeq ig(\omega)$, which leads to the same resonance condition of equation (2.48) and the same expression for extinction cross section given in the equation (2.45) presented in the electrostatic approximation [5]. The corresponding vector spherical harmonic is $\vec{N}^{(3)}_{e1n}$ and this is the field radiated by an

oscillating electric dipole, which agrees with the electrostatic approximation as well. Therefore, the local field around the particle is similar to the one presented in figure 2.9. With increasing radius of nanoparticle (20nm radius particle), the dipole peak moves to the longer wavelength and the scattering of the particle starts to be significant. For a 50nm radius particle, extinction is already dominated by the scattering. The dipole peak moves to 500nm and a quadrupole resonance given by the expansion coefficient a_2 appears at 400nm. The distribution of the field around the particle in the dipole and quadrupole resonance is shown in figure 2.11. By increasing the size of the particle, higher order resonances a_n, b_n are induced. The resonances associated with coefficient b_n are magnetic modes, and are due to the fact that their relative permeability equals to 1. Hence they have a smaller value than the corresponding a_n coefficients.

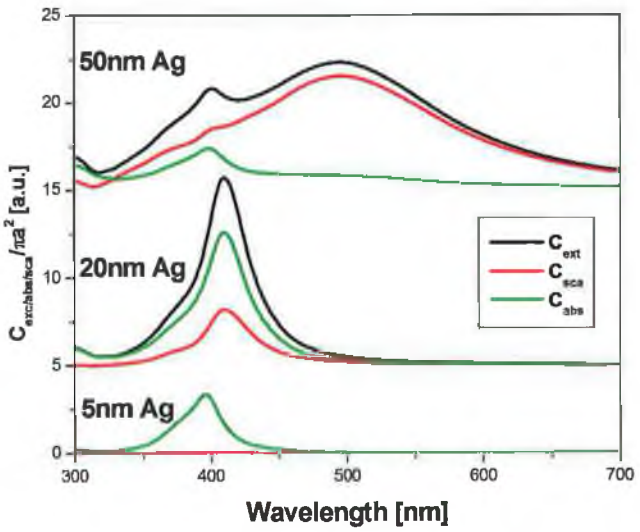

Figure 2.10: Extinction, absorption and scattering cross section (normalised to the profile of the sphere) of silver nanoparticles with different radius (5,20,50nm).

LSPR in a sphere with a shell

An alternative nanoparticle configuration to the solid particle discussed previously is that of a nanoparticle with an outer shell of different dielectric material.

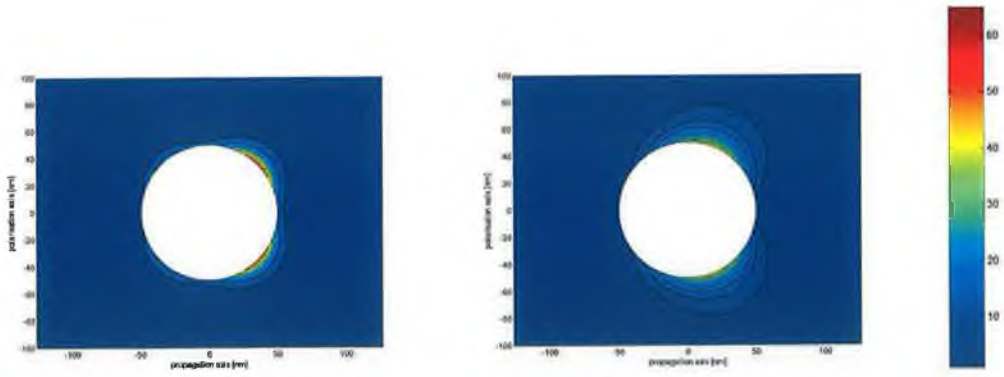

(a) (b)

Figure 2.11: A density graph of electric field around a 50nm radius silver NP by illumination with polarisated light (a)λ = 400nm. The NP is in the quadrupole resonance.(b)λ = 500nm. The NP is in the dipole resonance.

The introduction of the outer shell offers a protective layer, which prevents any objects (such as fluorescent molecules) to be in contact with the nanoparticle. As mentioned in the earlier section, an embedded medium influences the plasmon resonance in metal particles. In the case of a metal nanoparticle the higher dielectric constant shifts the plasmon resonance towards longer wavelengths. The field outside the particle with a shell and its cross section can be obtained with a similar method to that used in the previous section. In this case, an additional field inside the shell has to be taken into account and the boundary conditions in equation (2.52) have to be applied on the particle-shell and shell-embedded medium interface. This again leads to a set of linear equations for the expansion coefficients of the fields. The external field $\vec{E_s}$ is of the same form as in equation 2.53, whereas the analytical expression of the coefficient a_n, b_n is more complicated. The analytical expression is given in appendix B.

As an example, the extinction cross section of a 20 nm radius silver particle with different silica shell thickness (0,3,6,9,12nm) placed in water are presented in figure 2.12. Because the silica shell has a higher dielectric constant than water, the plasmon resonance shifts to longer wavelengths. This shift is non-linear with the shell thickness, where the shift per 1nm thickness of the shell is biggest for the thinnest shells because the field is the strongest at the surface of the particle.

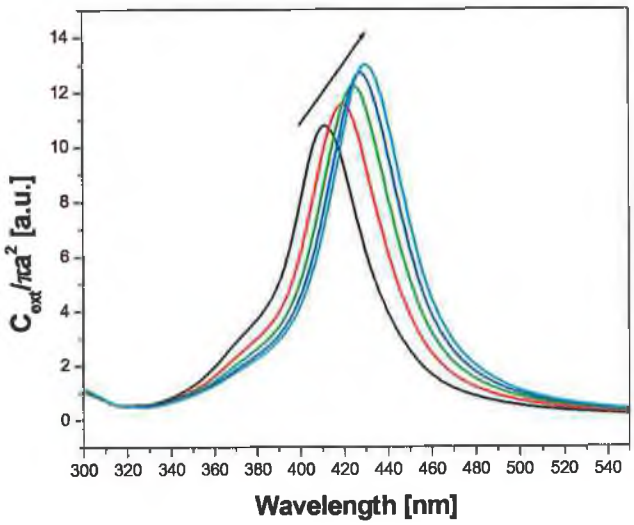

Figure 2.12: Extinction scattering cross section (normalised to the profile of the sphere) of 20nm silver nanoparticles with silica shell of different thickness (0,3,6,9,12nm) in water. The arrow indicates increasing thickness of the shell.

LSPR in non-spherical nanoparticles

For shapes differing from spheres, electrodynamic calculations are much more difficult and often only numerical methods have to be used. To illustrate the effect of non-sphericity on the localised surface plasmon resonance, the problem can also be solved in quasi-static approximation as it was solved for spheres in a previous section.

Let us consider a prolate spheroid with main axes equal $a, b = c < a$. The Laplace equation for a spheroid in a homogenous electric field oriented along one of the main axe is again solved. The solution of the field outside the particle at $r >> a$ is a field of a dipole [5], as in the case of a sphere, whereas the dipole has a different expression and is dependent upon which axis the field is applied. By the same reasoning as in the case of a sphere, the illuminated ellipsoid is substituted for an oscillating dipole (equation (2.43), $a^3 \rightarrow ab^2$), whereas the function $g(\omega)$ (equation (2.44)) is changed to

$$g_i(\omega) = \frac{\varepsilon^1(\omega) - \varepsilon^m}{3\varepsilon^m(\omega) + 3L_i(\varepsilon^1(\omega) - \varepsilon^m)} \qquad i = 1, 2 \tag{2.59}$$

$$L_1 = \frac{1-e^2}{e^2}\left(-1+\frac{1}{2e}\ln\frac{1+e}{1-e}\right) \qquad e^2 = 1-\frac{b^2}{a^2} \tag{2.60}$$

$$L_2 = (1-L_1)/2 \tag{2.61}$$

where index i=1 corresponds to the polarisation axis parallel to the main axis and and i=2 corresponds to the polarisation axis parallel to the minor axis of the spheroid. The parameters L_1, L_2 are given only by the geometry of the spheroid and can have values from 0 to 1. The following cross sections are computed in the same way as the cross section for a sphere (equation (2.45), $a^3 \rightarrow ab^2$). From the equation above, it follows that there are two resonance conditions of LSPR as shown in equation (2.48) (for each orientation of the spheroid)

$$\varepsilon^m + L_i(\varepsilon^1 - \varepsilon^m) = 0 \qquad i = 1,2 \tag{2.62}$$

As an example, the extinction cross section of a silver nanoparticle with the main axis equal to 12nm and different aspect radius values (1:1, 2:1, 3:1, 4:1) for each orientation of the particle are presented in figure 2.13. When the particle becomes more prolate, the plasmon resonance in the direction of the main axis shifts to longer wavelengths and the plasmon resonance in the direction of minor axis moves to shorter wavelengths. Therefore, by changing the aspect ratio it is possible to move the plasmon resonance of the particle and also the plasmon resonance depends on the orientation of the particle.

Demonstration of the plasmon resonance in ellipsoidal nanoparticles can be found in [17, 18]. When the size of the nanoparticle is increased, the quasi-static approximation is no longer valid and additional higher order resonances are seen in the extinction spectra as in the case of large spheres. An observation of the higher order resonances in spheroids is described in [19].

For even more complicated shapes of nanoparticles only numerical methods can be used. Two techniques are now presented, which were considered for the calculation of plasmon resonance in non-spherical nanoparticles. One of the methods is the point matching method [20]. This method is based on Mie theory; the field inside and the scattered field are expanded into the vector spherical harmonics and the boundary conditions are solved. Because of non-spherical objects, the expansion coefficients can not be solved separately for each order n, but the boundary condition is written for k-points at the surface of the particle (k is bigger than the number of unknown coefficients of the expanded fields) and afterwards this

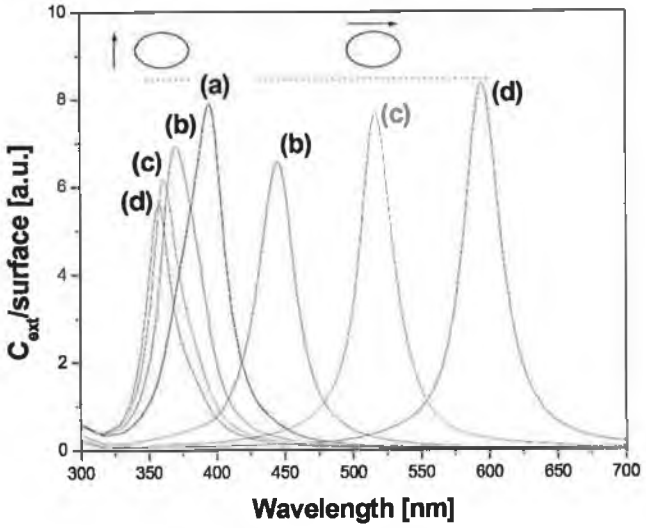

Figure 2.13: Calculated extinction cross section (normalised to the profile of the ellipse) of silver prolate spheroidal nanoparticles with different aspect radius (a-d == 1:1, 2:1, 3:1, 4:1). The length of the main semi-axis was 12nm. Peaks on the right correspond to the polarisation axis in the direction of the main semi-axis; peaks on the left correspond to the polarisation axis in the direction of the minor semi-axis.

system of linear equations is solved. This technique can be improved by expansion of the field into spherical harmonics with multiple origin [21]. Nevertheless, these techniques work well only for a particle with azimuthal symmetry.

Another technique is discrete dipole approximation [22], [23] (DDA). In this method the particle is represented by a three-dimensional array of point dipoles, where the spacing between the dipole is smaller then the wavelength of the incident field. Afterwards, the interaction of each dipole with the incident field and the field generated from other dipoles is calculated. This set of equations leads to the self-consistent solution for the dipole polarizations. A software package based on this method for calculating the extinction spectra of arbitrary spheres is freely available [24] and was used in the calculation of extinction spectra of non-spherical nanoparticles. As an example, the extinction cross section of a silver nanoprism with a side of 60nm and a depth of 26nm illuminated perpen-

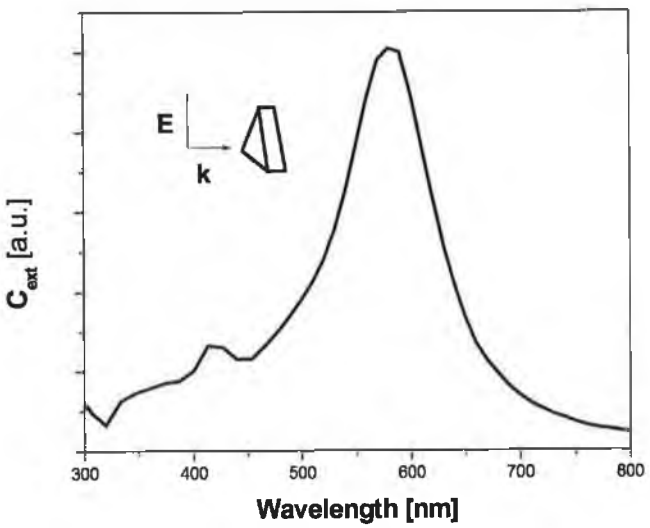

Figure 2.14: Extinction cross section of a silver nanoprism with side 60nm and width of 26nm in water calculated using DDA method. The peak at 590nm corresponds to the dipole resonance and the peak at the 410nm corresponds to the quadrupole resonance in the plane of the prism.

dicularly to the main side in water is presented in figure 2.14. The peak at 590nm can be associated with the dipole resonance and the peak at the 410nm with the quadrupole resonance in the plane of the prism, as it shown in [25]. As in the case of the ellipsoidal nanoparticles, increasing the ratio of length to width of the triangle, the in-plane plasmon resonance shifts to longer wavelengths. The discrete dipole approximation predicts the extinction spectra quite well, but the values of the near field around the particles are dependent on the size of dipole spacing [26]. A detailed list of other methods used to tackle the problem of scattering of light by non-spherical particles can be found in [27].

2.4 A dye molecule in the proximity of a nanoparticle

The focus of this work is on the interactions between LSPR and fluorescent dye. The optical properties of a fluorescent dye can be dramatically changed by the presence of a metal nanoparticle. As explained earlier in this chapter, the fluorescence process consists of the absorption of a photon and subsequently the emission of a photon at lower energy. The presence of a metal nanoparticle in LSPR locally concentrates electromagnetic waves of the incident field and can increase the absorption process of a molecule. This process is analogous to adding an antenna to a receiver. Further, the nanoparticle can also change the electromagnetic field emitted by the fluorescent dye, and therefore influence the emission properties of the dye. If the properties of the nanoparticle and the dye are appropriately chosen, the nanoparticle acts as an antenna increasing the emission rate of the dye. These two effects will be now described in more detail in the following sections.

2.4.1 Enhanced excitation

In terms of electromagnetic theory, a fluorescent dye can be modelled as an oscillating electric dipole $\vec{p}_{ex}$. If the illumination light $(\vec{E}_i, \vec{H}_i)$ is not too strong, the molecule is not in saturation and the absorption rate is proportional both to the intensity of the light ($\propto |E_i|^2$) and to the macroscopically measured molar absorptivity ϵ of the molecule. Additionally, the absorption rate also depends upon the orientation of the molecule to the excitation electric field. Molecules with their dipole moment perpendicular to the vector of electric field are not excited. Therefore, the average excitation rate k_{ex} of the molecule can be written as [28]

$$k_{ex}^{i} \propto \epsilon(\lambda)|\hat{p}_{ex} \cdot \vec{E}_i|^2 \tag{2.63}$$

When a nanoparticle is placed close to the dye, the electric field $\vec{E}_i$ in the above expression has to be changed to the electric field $\vec{E}_1$ generated by the nanoparticle. As mentioned in the previous section, the local field around the nanoparticle can be much bigger than the incident field and therefore the excitation enhancement

factor can be defined as

$$R_{ex} = \frac{|\hat{p}_{ex} \cdot \vec{E}_l|^2}{|\hat{p}_{ex} \cdot \vec{E}_i|^2} \tag{2.64}$$

While the magnitude and the orientation of the electromagnetic field caused by the nanoparticle varies strongly with the position and the illumination wavelength, the excitation enhancement factor will also depend on the position and the orientation of the dipole. In the following section, the excitation enhancement factor for a fluorescent dye in the proximity of a spherical nanoparticle will be presented and then generalised to non-spherical nanoparticles.

Let us consider a fluorescent dye at position (d, θ, ϕ) with the dipole $\vec{p}_{ex}$ in medium with dielectric constant ε^m illuminated with a plane wave polarised along the x-axis and propagating in the z-direction. Next, consider a nanoparticle of radius a $(a < d)$ with dielectric constant ε^1 placed at the origin. While the distribution of the electric field around a nanoparticle was already presented in section 2.3.2, the excitation enhancement can be expressed as

$$R_{ex}(d, \theta, \phi, \hat{p}_{ex}) = \frac{|\hat{p}_{ex} \cdot (\vec{E}_i + \vec{E}_s)|^2}{|\hat{p}_{ex} \cdot \vec{E}_i|^2} \tag{2.65}$$

where electric field $\vec{E}_i$ and $\vec{E}_s$ are described by equations (2.50, 2.53).

In our experiments, fluorescence was not measured from a single molecule, but rather from an ensemble of molecules isotropically distributed over the angles θ, ϕ. Therefore, we define an averaged excitation enhancement as

$$\overline{R_{ex}}(d, \hat{p}_{ex}) = \frac{\int_{r=d} |\hat{p}_{ex} \cdot (\vec{E}_i + \vec{E}_s)|^2 dS}{\int_{r=d} |\hat{p}_{ex} \cdot \vec{E}_i|^2 dS} \tag{2.66}$$

Next, the orientation of the dipole has to be specified. At the beginning, the dipole will be oriented perpendicularly to the surface of the nanoparticle $(\hat{p}_{ex} || \hat{r})$, which allows us to evaluate integrals in the averaged excitation enhancement. Using equations (2.51, 2.53) for the fields expressed in spherical harmonics and the orthogonality of the spherical harmonics, the averaged excitation enhancement can be simplified to

$$\overline{R_{ex}} = \frac{3}{2} \frac{1}{(kd)^2} \sum_{n=1}^{\infty} (2n+1)(n+1)n \cdot \\ [|h_n(kd)|^2 |a_n|^2 - 2j_n(kd)(j_n(kd)\mathrm{Re}\{a_n\} + y_n(kd)\mathrm{Im}\{a_n\})] \tag{2.67}$$

where $k = 2\pi\sqrt{\varepsilon^m}/\lambda$ and the expansion coefficients a_n are from computed from equation (2.54).

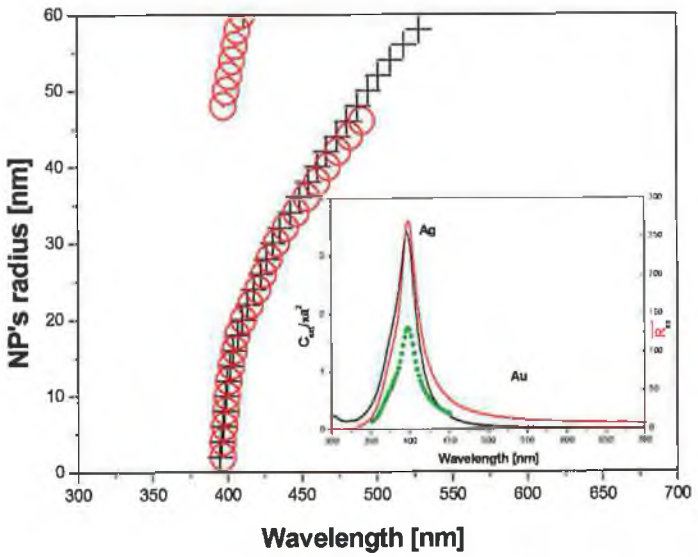

Figure 2.15: Dependence of the maxima of the extinction cross section C_{ext} (cross) and excitation enhancement $\overline{R_{ex}}$ (circle) on the wavelength and the radius of silver nanoparticles immersed in water. Inset: Profile of the extinction cross section (black line) and excitation enhancement ($\hat{p}_{ex}||\hat{r}$ - red line, $\hat{p}_{ex}$ isotropically oriented - green dots) for 5nm silver nanoparticles.

As an example, the enhancement factor for a silver nanoparticle of 5nm radius immersed in water and with the dipole placed at the surface of the sphere is presented in the inset of figure 2.15. The enhancement factor has a sharp peak around at 400nm, which corresponds with the peak in the extinction cross section of the nanoparticle. The positions of the peak of the extinction cross section and the enhancement factor were than calculated for different nanoparticle radius values and the results are plotted in figure 2.15. It can be seen that the maxima are very close to each other up to the radius of 45nm and then slightly shift to longer wavelength. For a bigger radius, the higher order excitation field (see figure 2.11 (a)) becomes more intense, giving broader peaks and the maxima of extinction and enhancement no longer coincide.

The absolute value of the excitation enhancement as a function of wavelength

and the nanoparticle radius is plotted in figure 2.16. We can see that the enhancement factor is largest for very small particles (optimal around 10nm) and with increasing size the enhancement decreases. For larger nanoparticles, the peak from the quadrupole excitation of around 400nm is visible.

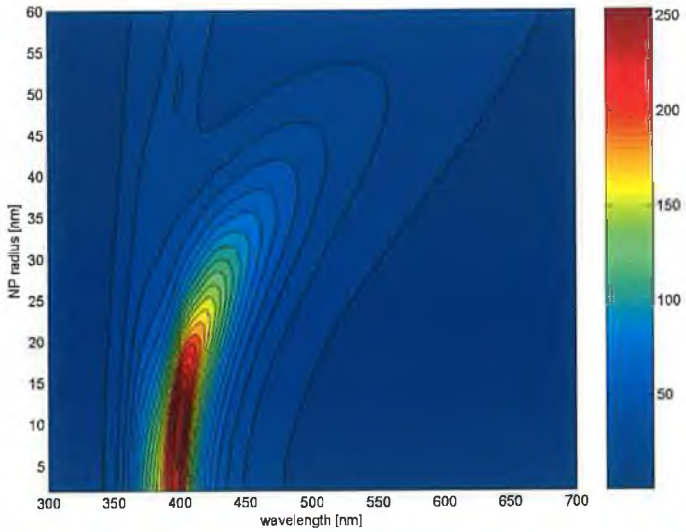

Figure 2.16: Density graph of the excitation enhancement $\overline{R_{ex}}(d = r)$ on wavelength and radius of silver nanoparticle immersed in water.

Another aspect of the excitation enhancement is the dependence on the distance of the dipole from the nanoparticle. As was shown in figure 2.9, the electric field is localised in the vicinity of the nanoparticle and therefore, the excitation enhancement will decrease with the increasing distance of the dye from the nanoparticle. The distance dependence of the excitation enhancement on the dye-nanoparticle separation for different nanoparticle radii is plotted in figure 2.17. We can see that for small nanoparticles the enhancement is the largest (as was shown from the figure 2.16) for zero distance, but very quickly decreases with increasing distance. In contrast, a larger nanoparticle will generate smaller enhancement at zero distance but the enhancement does not drop so quickly with increasing dye-nanoparticle separation.

For the case of a gold nanoparticle, the excitation enhancement again correlates with the extinction cross section (for small nanoparticles λ 520nm, see

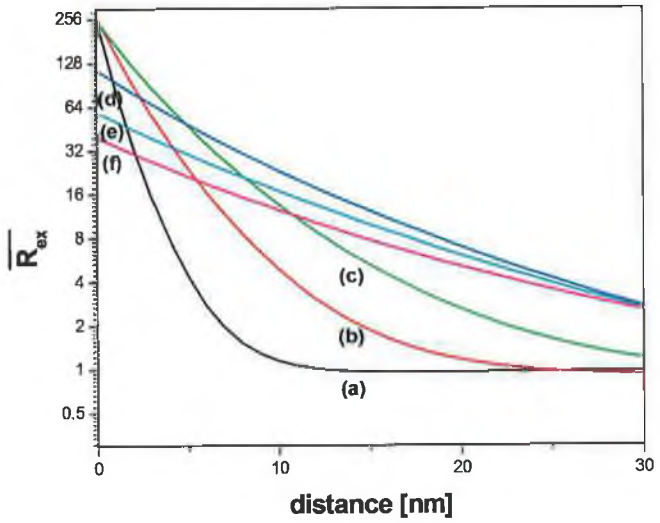

Figure 2.17: Graph of the excitation enhancement $\overline{R_{ex}}$ as a function of the distance of the dye from the nanoparticle for different NP's radius (a)-5nm; (b)-10nm; (c)-15nm; (d)-30nm; (e)-40nm; (f)-50nm.

figure 2.7 (b)). Nevertheless, the maxima of the enhancement reaches only one tenth of the enhancement for the silver nanoparticles. This is caused by the core electrons in the gold, as was explained in a previous section.

In the case where the orientation of the dipole is not fixed, the excitation enhancement should be averaged over all possible orientations of the dipole. For a particular space with electric field $\vec{E}$ the expression $|\hat{p} \cdot \vec{E}|$ averaged over all orientations of the dipole is equal to $1/3|\vec{E}|$. Therefore, using equation (2.66), the averaged excitation enhancement factor for isotropic orientation of the dipole can be defined as

$$\overline{R_{ex}}(d) = \frac{1}{4\pi|\vec{E}_i|^2} \int_{r=d} |\vec{E}_i + \vec{E}_s|^2 dS \tag{2.68}$$

This expression can not be simplified and a numerical integration has to be used to evaluate it. As an example, the enhancement factor for 5nm radius silver nanoparticles in water with the dipole isotropically distributed at the surface of the nanoparticle is presented in the inset of figure 2.15. We can see that the profile for radial and isotropic enhancement is similar, whereas the value for isotropic

orientation of the dipole is much smaller. This is caused by the fact that the radial component of the electric field close to the nanoparticle is the largest.

2.4.2 Enhanced emission

The presence of a nanoparticle can influence the emission properties of a fluorescent dye, such as the quantum yield ϕ and the fluorescence life time τ. This can be explained by adding de-excitation rates caused by the presence of the nanoparticle into the equation for the quantum yield. Therefore, the quantum yield of a free dye expressed by equation (2.2) changes to

$$\phi_m = \frac{k_r + k_r^m}{k_r + k_{rn} + k_r^m + k_{nr}^m} \tag{2.69}$$

where k_r and k_{nr} are radiative and non-radiative de-excitation rates of a free dye and k_r^m and k_{nr}^m are the new radiative and non-radiative de-excitation rates due to the nanoparticle. The corresponding fluorescence life time τ (equation (2.3)) changes to

$$1/\tau^m = k_r + k_{nr} + k_r^m + k_{nr}^m \tag{2.70}$$

From this equation it follows that in the presence of a nanoparticle the fluorescence life time is shorter ($\tau^m < \tau$).

An enhanced fluorescence can be achieved if the modified quantum efficiency ϕ_m is larger than the initial quantum efficiency of a dye. The emission enhancement R_{em} can be defined as

$$R_{em} = \frac{\phi_m}{\phi} \tag{2.71}$$

To evaluate the emission enhancement one must calculate the de-excitation rates k_r^m and k_{nr}^m. This is in general very complicated and some special cases are given, for example in references [29, 30, 31].

A simpler theory describing the radiative and non-radiative decay rates in the small particle limit was described in [32]. The fluorescent molecule is described as an oscillating dipole at wavelength λ_{em}. When the dye is placed close to a nanoparticle, energy from the dye is coupled to the surface modes of the nanoparticle which then re-radiate the energy into the space. From the theory it follows that the radiative rate of the dye-nanoparticle system is proportional to the enhancement of the local field at the fluorescence wavelength and can be

approximately expressed as

$$k_r + k_r^m = k_r R_{ex}(\lambda_{em}) \tag{2.72}$$

where R_{ex} is evaluated at the emission wavelength. From the results of the excitation enhancement we can conclude that the biggest enhancement of the radiative rate is achieved if the plasmon resonance wavelength of the nanoparticle coincides with the emission wavelength of the dye and also if the dye is very close to the nanoparticle.

The main quenching mechanism in the nanoparticle-dye system is excitation of lossy surface waves that dissipate energy through coupling to the bulk scattering processes. It is especially important for a very small nanoparticle-dye separation. In the approximation of small distance limit, the non-radiative rate can written as [33]

$$k_{nr}^m = \frac{k_r A}{l^3} \tag{2.73}$$

where A is constant and l is the nanoparticle-dye separation. Therefore, for very small distances (a few nanometers) the non-radiative de-excitation rates reach very large values and the quantum efficiency (ϕ_m) drops to zero (see equation 2.69) The same effect occurs also by placing a dye molecule close to a metal surface (known as metal-fluorophore quenching [34]).

The emission enhancement strongly depends on the quantum efficiency of the dye ϕ. A dye with a low quantum efficiency has a non-radiative rate much larger than the radiative rate ($k_{nr} >> k_r$). When a nanoparticle is at a distance such that the non-radiative rate is not increased ($k_{nr}^m << k_{nr}$) the emission enhancement from this dye can be approximately expressed as

$$R_{em} = R_{ex}(\lambda_{em}) \tag{2.74}$$

Nevertheless, this enhancement can not be larger than the value $1/\phi$, as it follows from its definition and the definition of the quantum efficiency (quantum efficiency can not be bigger than 1). From this it also follows that the fluorescence emission can not be increased significantly for a dye with high quantum efficiency and the only effect will be in shortening of the fluorescence lifetime τ time, which can lead to increased photostability of the dye [35].

To summarise, the emission from a dye can be increased by the presence of a nanoparticle. If the plasmon resonance of the nanoparticle matches the emission

wavelength of the dye, the emission rate of the dye can be increased leading to an increase of quantum efficiency. Nevertheless, the proximity of a nanoparticle to the dye with a high quantum efficiency can not lead to the significant enhancement, while the quantum efficiency can not be bigger than one. Moreover, a nanoparticle too close to the dye molecule can lead to a decrease of the quantum efficiency of the dye and therefore to a decrease of the fluorescent signal.

2.4.3 Optimisation of the enhanced fluorescence

From the preceding section it is obvious that the plasmonic enhancement of fluorescence strongly depends on the properties of the nanoparticle, properties of the dye, and their relative positions. Therefore, nanoparticles will need to be tailored to match dye spectral properties in order to increase fluorescence. From the results of the previous section we can conclude some general rules for designing of such nanoparticles.

Generally, the properties of the dye, such as excitation and emission wavelength, molar absorptivity and the quantum efficiency of the dye are given and can not be changed. Therefore, the parameters which can be varied are nanoparticle shape, size, material, and the nanoparticle-dye separation. It was pointed out earlier that there are two effects of enhancement: an increase in excitation and an increased in quantum efficiency. These enhancements are functions of the plasmon resonance of the nanoparticle. The excitation enhancement is maximum if the plasmon resonance coincides with the peak excitation wavelength of the dye and the emission enhancement is maximum if the plasmon resonance coincides with the peak emission wavelength. Therefore, the plasmon resonance should be tuned to one of these wavelengths. The plasmon resonance can be varied by the material, size and shape of the nanoparticle. As the maximum emission enhancement is always smaller than the excitation enhancement (and in the case of high quantum efficiency is insufficient), the plasmon resonance is preferably set to the excitation wavelength. Another important parameter is the nanoparticle-dye distance. For very small distances the non-radiative decay rate is very large and all the fluorescence is quenched. On the other hand, if the distance is too large, the excitation increase and the increase of the radiative de-excitation rate (k_r^m) are minimal. The optimum distance differs for each system, but generally

it is between 1-10nm. The next parameter that can be varied is the size of the nanoparticle. As well as changing the plasmon resonance of the nanoparticle, it influences the decrease of the excitation enhancement and the radiative de-excitation rate with nanoparticle-dye distance. The largest enhancement is for small nanoparticles ($<$ 10nm) at the surface , but the enhancement is too confined around the nanoparticle and is insignificant at the distance which overcomes dye-quenching, whereas very large ($>$ 100nm) nanoparticles do not exhibit any significant enhancement.

2.5 Conclusion

This chapter describes the theory underlying the plasmonic enhancement of fluorescence. In the first part, a brief explanation of the phosphorescence effect in molecules was explained. In the next part, the interaction of electromagnetic waves with a metal nanoparticle was described in the framework of electromagnetic theory. The resonance modes in the absorption spectra of the nanoparticles were then associated with the localised plasmon resonance and their properties were elucidated in detail for the case of spherical nanoparticles. Further, some conclusions were made for the localised surface plasmon resonances in non-spherical nanoparticles. In the last section, the effect of the presence of a metal nanoparticle on the fluorescence from a dye was described. Two types of enhancement (excitation enhancement and emission enhancement) were defined and their dependence on nanoparticle and dye parameters were studied. From these results, some general rules for optimising the plasmonic enhancement of fluorescence could be concluded.

Bibliography

[1] J R Lakowicz. *Principles of Fluorescence Spectroscopy.* 1999.

[2] G Shenk. *Absorption of Light and Ultraviolet Radiation: fluorescence and phosporescence emission.* Allyn and Bacon chemistry series. Allyn and Bacon, Inc, Boston, 1973.

[3] D Rendell. *Fluorescence and Phosphorescence.* John Wiley & Sons Ltd, 1987.

[4] H C Chen. *Theory of Elecromagnetic Waves.* R. R. Donnelley & Sons Company, 1983.

[5] C F Bohren and D R Huffman. *Absorption and Scattering of Light by small Particles.* John Willey & Sons, Inc., 1983.

[6] J A Stratton. *Elecromagnetic theory.* International series in pure and applied physics. McGraw-Hill Book Company, Inc., 1941.

[7] D Sarkar and N J Halas. General vector basis function solution of maxwell's equations. *Physical review E*, 56:1102–1112, 1997.

[8] P B Johnson and R W Christy. Optical constants of the noble metals. *Physical review B*, 6(12):4370–4379, 1972.

[9] K Stahrenberg, T Hermann, K Wilmers, N Esser, and W Richter. Optical properties of copper and silver in the energy range 2.5-9.0 ev. *Physical review B*, 64:115111, 2001.

[10] E. D. Palik. *Handbook of Optical-Constants*, volume 1 of *Journal of the Optical Society of America a-Optics Image Science and Vision.* Academic Press Inc., 1984.

[11] U Kreibig and M Vollmer. *Optical properties of Metal Clusters.* Springer Series in Materials Science. Springer-Verlag Berlin Heidelberg, 1995.

[12] J B Marion and M A Heald. *Classical electromagnetic radiation.* Academic Press, Inc., 1980.

[13] C Kittel. *Introduction to Solid State Physics.* John Wiley & Sins, Inc., New York, 1996.

[14] H Raether. *Surface plasmons on smooth and rough surfaces and on gratings*, volume 111 of *Springer tracts in modern physics.* 1988.

[15] A Adams, J C Wyss, and P K Hansma. Possible observation of local plasmon modes excited by electrons tunneling through junctions. *Physical review letters*, 42(14):912–915, 1979.

[16] G Mie. Beitrage zur optik trueber medien speziell kolloidaler metalloesungen. *Ann. Phys.*, 25:377–445, 1908.

[17] S. W. Kennerly, J. W. Little, R. J. Warmack, and T. L. Ferrell. Optical-properties of heated ag films. *Physical Review B*, 29(6):2926–2929, 1984.

[18] P. Orfanides, T. F. Buckner, M. C. Buncick, F. Meriaudeau, and T. L. Ferrell. Demonstration of surface plasmons in metal island films and the effect of the surrounding medium - an undergraduate experiment. *American Journal of Physics*, 68(10):936–942, 2000.

[19] J. R. Krenn, G. Schider, W. Rechberger, B. Lamprecht, A. Leitner, F. R. Aussenegg, and J. C. Weeber. Design of multipolar plasmon excitations in silver nanoparticles. *Applied Physics Letters*, 77(21):3379–3381, 2000.

[20] K Joo and M F Iskander. A new procedure of point-matching method for calculating the absorption and scattering of lossy dielectric objects. *IEEE Transactions on antennas and propagation*, 38(9, September):1483–1490, 1990.

[21] H M Al-Rizzo and J M Tranquilla. Electromagnetic wave scattering by highly elongated and geometrically composite objects of large size parameters: the generalized mulipole technique. *Applied Optics*, 3502(34):18, 1995.

[22] DB Goodman, B T Draine, and P J Flatau. Application of fast-fourier-transform techniques to the discrete-dipole approximation. *Optics Letters*, 16(15):1198–1200, 1991.

[23] K Shimura and T D Milster. Vector difraction analysis by discrete-dipole approximation. *Journal of Optical Society of America A*, 18(11):2895–2900, 2001.

[24] B T Draine and P J Flatau. User guide for the discrete dipole approximation code ddscat.6.0., 2003.

[25] K. L. Kelly, E. Coronado, L. L. Zhao, and G. C. Schatz. The optical properties of metal nanoparticles: The influence of size, shape, and dielectric environment. *Journal of Physical Chemistry B*, 107(3):668–677, 2003.

[26] E Hao and G C Schatz. electromagnetic fields around silver nanoparticles and dimers. *Journal of chemical physics*, 120(1, 1 January):357–366, 2004.

[27] M I Mishchenko, L D Travis, and A A Lacis. *Scattering, Absorption, and emission of light by small particles.* Cambridge university press, 2002.

[28] J Enderlein. Electrodynamics of fluorescence, 2003.

[29] P Anger, P Bharadwaj, and L Novotny. Enhancement and quenching of single-molecule fluorescence. *Physical Review Letters*, 96:113002, 2006.

[30] J Enderlein. Theoretical study of single molecule fluorescence in a metallic nanocavity. *Applied Physics Letters*, 80(2):315–317, 2002.

[31] P C Das and A Puri. Energy flow and fluorescence near a small metal particle. *Physical Review B*, 65:155416, 2002.

[32] J. Gersten and A. Nitzan. Spectroscopic properties of molecules interacting with small dielectric particles. *Journal of Chemical Physics*, 75(3):1139–1152, 1981.

[33] J. Kummerlen, A. Leitner, H. Brunner, F. R. Aussenegg, and A. Wokaun. Enhanced dye fluorescence over silver island films - analysis of the distance dependence. *Molecular Physics*, 80(5):1031–1046, 1993.

[34] R.R. Chance, A. Prock, and R. Silbey. Molecular fluorescence and energy transer near interfaces. *Adv. Chem. Phys.*, 60:1–65, 1978.

[35] J R Lakowicz, B Shen, and I Gryczynski. Intrinsic fluorescence from dna can be enhanced be metallic particles. *Biochem. Biophis. Res. Commun.*, 286:875–879, 2001.

Chapter 3

Fluorescence enhancement using metalnanoislands

This chapter describes two methods for the preparation and characterisation of nano-structured surfaces and also describes the associated dye fluorescence enhancement effects. In both techniques, metal layers were deposited onto surfaces via vacuum deposition techniques and their nano-structuring was carried out either by thermal annealing or by a novel lithographic technique called nanosphere lithography. The aim was to look at the versatility of these techniques and to investigate the incorporation of nano-structures prepared by these techniques in fluorescence-based bio-sensors.

3.1 Thermally evaporated metal on glass substrates

Vacuum thermal evaporation of metal onto glass substrates [1, 2, 3, 4] is a very simple method for the preparation of metal nanostructures that exhibit localised surface plasmon resonance. Because of the high mobility of metal atoms on the glass substrates during the evaporation, for metal films less than 15nm thick, the materials are deposited at nucleation points thereby producing isolated metal islands. This type of layer formation is known as *island growth* and is common for deposition of a metal on dielectric substrates. In order to achieve better plasmon resonance effects, these isolated films can be transformed into more ellipsoidal

shaped structures by annealing the substrates at high temperatures. This phenomenon is caused by the high metal-glass surface tension. The schematics of the method are shown in figure 3.1.

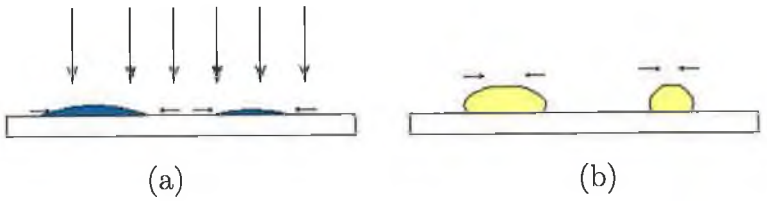

Figure 3.1: Schematic illustrating the principle of the formation of metal nanoislands on glass substrates. In the first step (a) metal is deposited in a vacuum chamber. Isolated metal films are created due to the mobility of the metal atoms on the substrate. In the next step (b) the substrate is annealed to form ellipsoidal-shaped nanoislands. The growth is due to the high metal-glass surface tension.

In chapter 2 it was explained that the spectral position of the localised plasmon resonance is an important factor in the plasmonic enhancement of fluorescence. Therefore, this technique was examined from the point of view of the versatility of the plasmon resonance.

3.1.1 Experimental

Deposition technique

Glass microscope slides were employed as substrates for the thermal evaporation of metals. The slides were cleaned using a 10 M solution of NaOH in deionised water. After drying in a flow of nitrogen, the samples were placed in a deposition chamber (Edwards Coating System E306A). After reducing the pressure to at least 10^{-5} mbar, a layer of metal was evaporated. Evaporation rates were varied from 0.02nms^{-1} to 0.2nms^{-1}, resulting in thicknesses of evaporated material in the range of 3nm to 8nm. After evaporation, the samples were annealed in an oven at 200 ^{o}C. Two metals, silver and gold, were used to form the nanoislands.

Optical characterisation

The UV-VIS extinction spectra were measured in transmission mode. A beam from a halogen lamp (LS1 Ocean Optics, Inc) was focused on the sample into

an area of approximately 3 mm^2. Unpolarised light was used. Transmitted light was collected with a fibre, which was coupled to a spectrometer (S2000 Ocean Optics, Inc). The slide was mounted in a holder that allowed motion in the plane perpendicular to the beam.

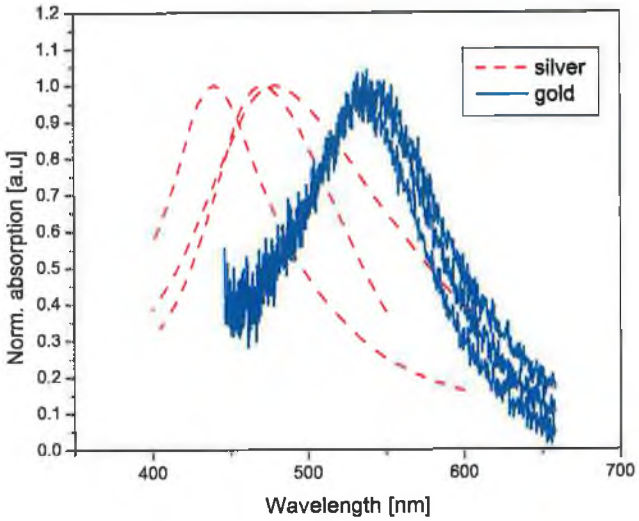

Figure 3.2: Normalised absorption spectra of NPs prepared using thermal evaporation. λ_{res} varies with changing layer thickness, annealing temperature, annealing time and evaporated material.

3.1.2 Results

These glass substrates were visually inspected and the deposited metal films were observed to be uniform over a large area, with all samples exhibiting LSPR absorption. Typical normalised absorption spectra are shown in figure 3.2. The gold NPs exhibited weaker LSPR than the silver NPs. This is due to the higher imaginary dielectric constant of gold in the visible region and probably poor NP formation caused by a higher melting temperature than silver. The wavelength of LSPR for the silver NPs was approximately λ=450nm and for the gold NPs it was approximately λ=550nm. The silver formed ellipsoidally-shaped NPs on the substrate, as had been observed by Royer at al [5]. Due to the ellipsoidal

shape, the NPs showed a shift in the LSPR to longer wavelengths in comparison to spherical NPs.

In order to form metal nanoislands of different shapes, and consequently tune the plasmon resonance, the speed of deposition of the metal, the total amount of the deposited metal and the annealing time were all varied. Particular success was achieved for silver NPs, where variation of the annealing time and amount of deposited material caused the LSPR wavelength to vary from 430nm to 480nm. However, the technique was not very reproducible and the plasmon resonance changed from sample to sample. Despite using either gold or silver, the plasmon resonance ranged only from 430nm to 550nm and therefore the plasmonic effect would be minimal for dye that absorbs in the red region, which is a region of particular interest in bio-sensing. Therefore, it was decided to pursue an alternative deposition technique.

3.2 Nanosphere lithography technique

Nanosphere lithography is a process employed for fabricating 2D arrays of identical metal nanoparticles on a flat substrate. This technique was first used by Decker [6] and its main advantage is the low-cost production of well defined periodic nanostructures with resolutions similar to very expensive techniques such as e-beam lithography [7]. As a result, this technique, or variations of it, has been employed in numerous applications [8, 9, 10, 11, 12, 13, 14].

The technique involves three steps (see figure 3.3). Firstly, a layer of polystyrene beads is deposited on a substrate. Due to the self-assembly mechanism, the beads order on the surface in close-packed formation. In the second step, a metal layer of a controlled thickness is thermally evaporated over the sample. The ordered layer of the beads acts as a mask, which consists of triangular shaped holes between the beads. After the deposition, the polystyrene beads are removed, leaving an ordered array of metal nanoparticles on the surface.

The most difficult step in this procedure is the formation of an ordered closed-packed layer of polystyrene beads. This is dependent on the self-assembly ability of the beads. Initially, a suspension of beads is spread over the substrate. This can be achieved via various coating techniques (spin-coating, dip-coating, drop-coating). In the work presented here, dip-coating was employed. In this technique

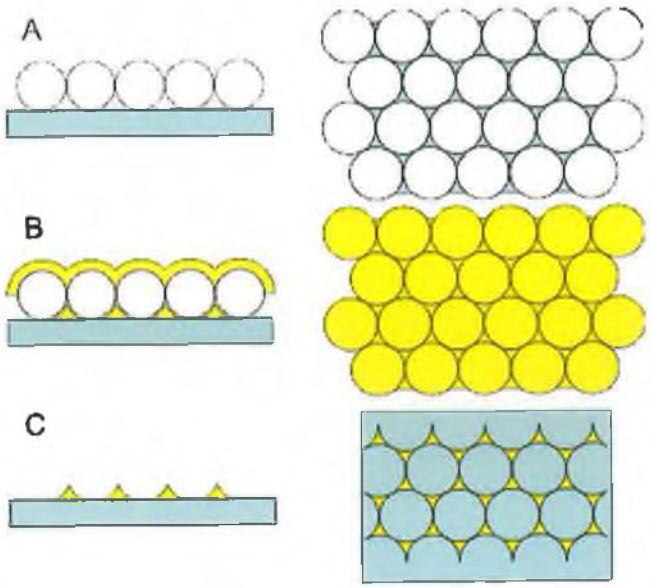

Figure 3.3: Schematic diagram of the steps involved in the nanosphere lithography technique. In step A a single layer of close-packed polystyrene spheres is formed. In step B a layer of metal is vacuum deposited over. In the last step C the layer of polystyrene beads is removed leaving triangular structures on the substrate.

the substrate is immersed in a suspension of beads and slowly withdrawn from the solution (figure 3.4 (a)). This results in the formation of a layer of beads on the substrate. Due to the capillary forces, which causes an aggregation of the beads (figure 3.4 (b)), the beads start to order. This ordered area grows further through convective particle flux caused by the water evaporation from ordered arrays that have already formed [15].

Using this technique it was possible produce nanoparticles of varying sizes by controlling the bead size and the quantity of deposited metal. Investigation were also carried out to determine the feasibility of using this technique to produce nanoparticles suitable for use in the plasmonic enhancement of fluorescence.

3.2.1 Experimental

Deposition procedure

Prior to depositing the polystyrene beads (PB), glass slides were cut into rectangles with approximate dimensions of 15x26 mm^2. The slides were cleaned by

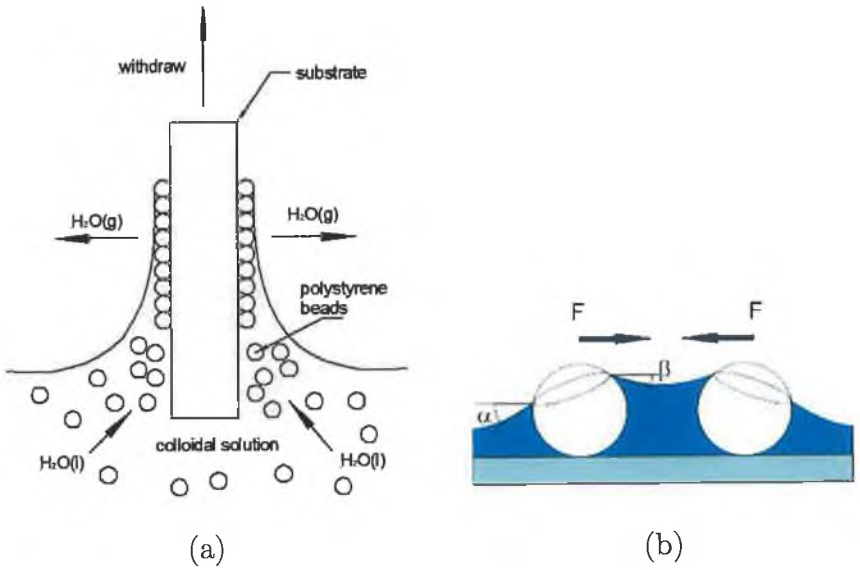

Figure 3.4: (A) Schematic image of processes by a withdrawal of a substrate from colloidal solution. (B) Schematic image of the forces acting on beads resulting in a self assembly process.

immersion in Piranha solution (3 : 1 H_2SO_4 : 27%H_2O_2), which was heated at 60°C for 1 hour. Afterwards, the slides were rinsed with deionised water and sonicated for 1 hour in a solution of H_2O : NH_4OH : 27%H_2O_2 (5:1:1) to enhance the hydrophilic nature of the surface. The cleaned slides were stored in a beaker of deionised water. A custom-made dip-coating system, with a dipping speed resolution of 1 mms^{-1}, was used for the deposition of the PBs. The cleaned glass slides were mounted in a holder, immersed in a suspension of PBs and subsequently withdrawn at low speed. The speed of withdrawal required to form a monolayer of PBs was found to be dependent on the diameter of the PBs and the temperature of the suspension. The optimum withdrawal speeds for forming an ordered monolayer of PBs at room temperature were determined to be $3-4$ μms^{-1} for 500nm PBs and $6-7$ μms^{-1} for 350nm PBs. After dip-coating, the samples were placed in a deposition chamber (Edwards Coating System E306A). A silver or gold layer with graduated thickness was deposited using an in-built shutter. Immediately after deposition, the samples were sonicated for approximately 5 minutes in pure ethanol to remove the PBs and were than dried in nitrogen (N_2). For the preparation of an enhancement chip, the sample was placed in the depo-

sition chamber again and a thin layer of SiO_x (thickness 6nm) was evaporated. This layer increased the adhesion of the NPs and produced a spacer layer on which the fluorescent dye was later deposited. As expected, the nanoparticles produced had a triangular cross sections due to the triangular spaces present in the PB layer.

Characterisation techniques

SEM images were taken using an S-3000N Hitachi (Hitachi Science Systems, Ltd) instrument. The applied voltage on the cathode was 25kV. Prior to taking images from samples with dielectric surfaces, a thin layer of silver (5nm) was deposited on the sample using a deposition chamber (Edwards Coating System E306A).

AFM images were collected using a Nano-R AFM (Pacific Nanotechnology). Si-tips in contact mode were used for the acquisition. The images were processed using WSxM 4.0 (Nanotec Electronica S.L.) software. Samples were scanned under ambient conditions.

The optical characterisation was carried out as described in section 3.1.1.

3.2.2 Results

Morphology of the layers

Using this technique, the most difficult element in the production of the nanoparticles was the formation of a monolayer of PBs on the glass substrate. After optimising this process, it was possible to obtain uniform monolayers over areas of $0.5cm^2$. Due to the effect of optical interference, it was possible with the naked eye to distinguish between different numbers of PB layers. After the thermal deposition of the metal, the formation of the PB layer was examined using SEM. A representative image is shown in figure 3.5, with the hexagonal packing of the PBs clearly visible (a). Displacements in the 2D ordered structure is observable at lower magnifications (b). Images of the NPs were obtained using the AFM. The triangular shape of the NPs is shown in figure 3.6. In figure 3.6 (b) some defects due to non-ideal ordering of the PBs are obvious.

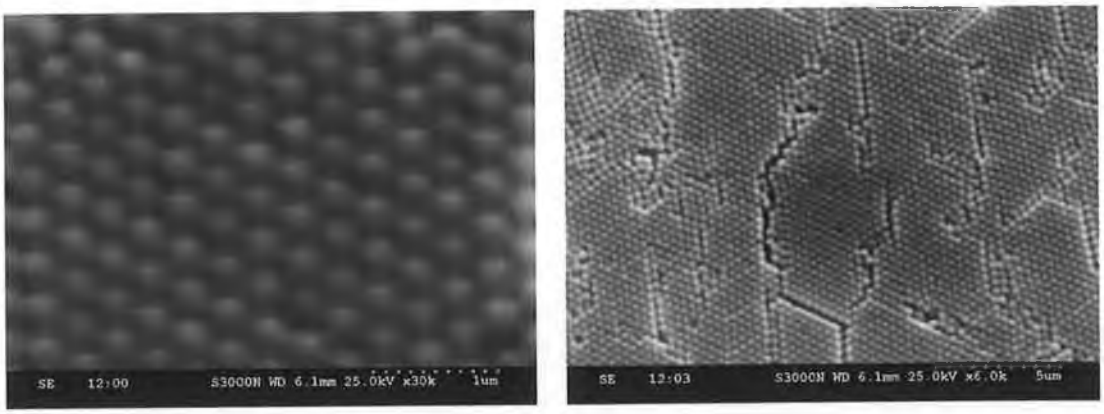

(a) (b)

Figure 3.5: (a) SEM image of the polystyrene bead layer (diameter of PB 300nm) formed on a glass slide. The beads form a hexagonal packaging. (b) lower magnification.

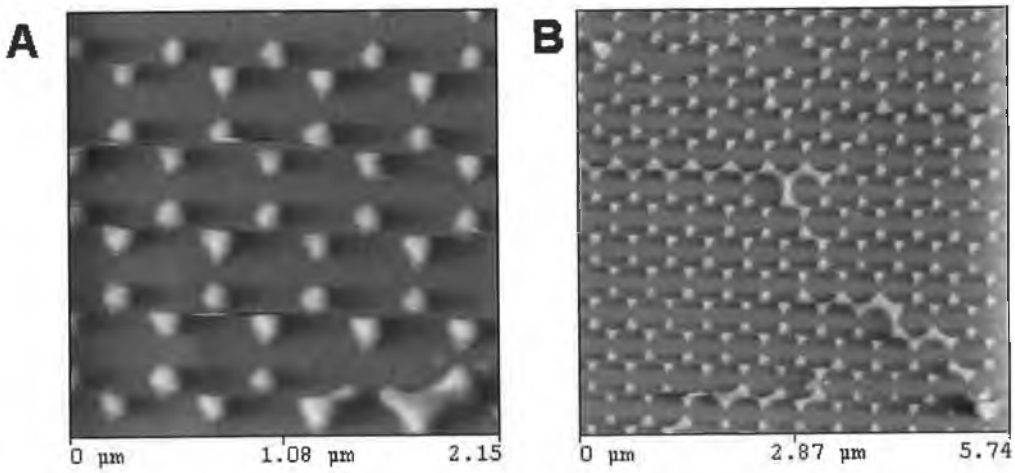

Figure 3.6: Images from Atomic Force Microscope. In image (a), the triangular shape of the nanoparticles (NPs) is visible. In image (b), a larger area of NPs is presented. The lines observed are due to displacements in the PB's layer.

Optical properties of the nanoparticle layers

The optical properties of NPs of different dimensions were examined. As explained in section 2.3.2, localised plasmon resonance is affected by the geometry of the nanoparticle. The less spherical a particle becomes the more the localised plasmon resonance is shifted to longer wavelengths. The absorption spectra of

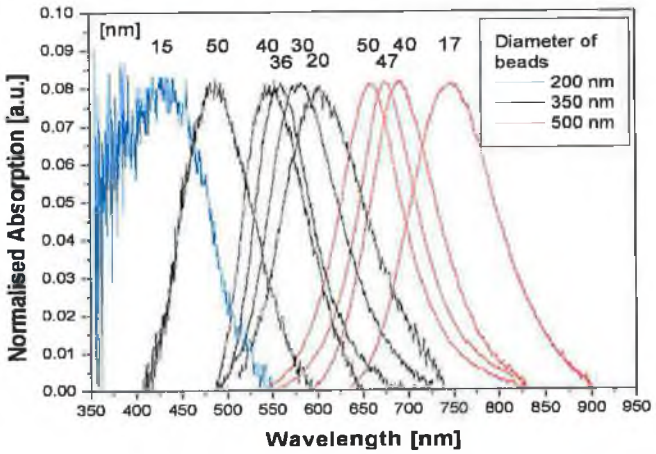

Figure 3.7: Normalised absorption spectra of NPs of different shapes. The horizontal size was varied by employing PBs of different diameters. The numbers shown above the peaks give the actual height of the NPs. The λ_{res} was varied over the entire visible spectrum.

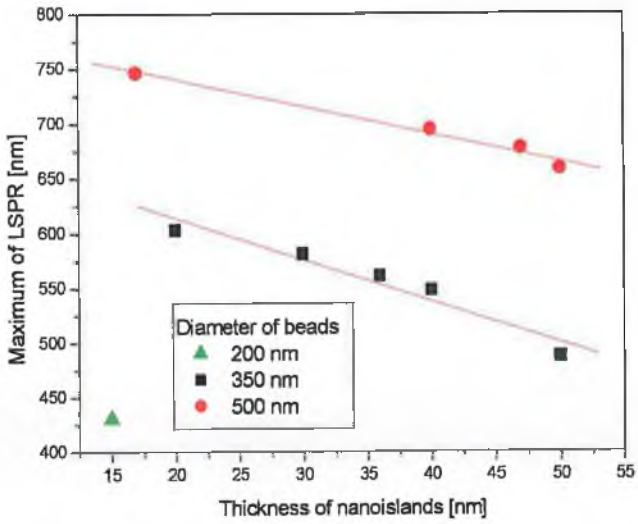

Figure 3.8: Dependence of λ_{res} on the thickness and diameter of the NPs. A linear fit was applied to the data.

the silver nanoparticles produced via the nanosphere lithography technique are shown in figure 3.7, with only the dipole peak presented. The position of the absorption peak was tuned by varying the diameter of the PBs. It was possible to shift the λ_{res} to the red region by increasing the diameter of the PBs. Moreover λ_{res} could also be tailored by varying the height of the NPs. Because the thermal evaporation of metal enables precise control of the height of NPs, it was possible to tailor λ_{res} with nanometer precision. Figure 3.8 shows the variation of λ_{res} as a function of PB size and metal layer thickness.

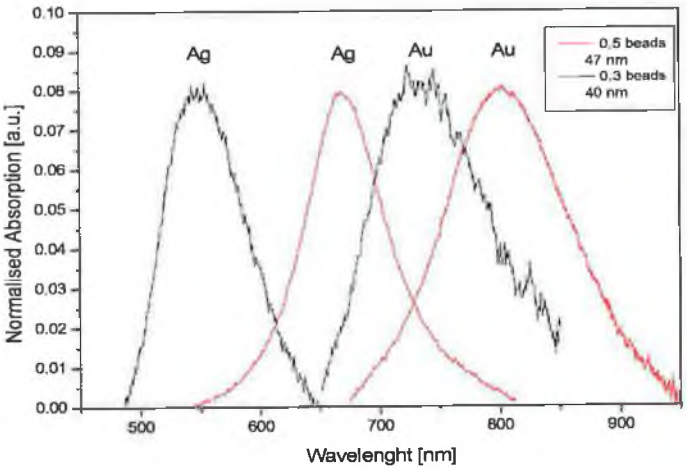

Figure 3.9: Normalized absorption spectra of NPs made from different materials.

The effect of the material on the plasmon resonance was also examined. Layers of triangular nanoparticles of the same shape but made from silver and gold were prepared and their optical properties were measured. The absorption spectra are presented in figure 3.9. The plasmon resonance of gold nanoparticles was shifted to longer wavelengths and it was much weaker than in the case of silver, which is in agreement with the theory. Therefore, only the silver nanoparticles were used in the subsequent experiments.

It was found that there was weak adhesion of the prepared NP layers to the glass substrate. Differences were observed in the absorption spectra of samples that were scanned before and after immersion in water (then dried in a flow of N_2). There was a shift in λ_{res} of about 150 nm towards shorter wavelengths and

a spreading of the peak. It was deduced that this was due to removal of the outer tips of the nanoparticles and this is in agreement with theoretical calculations [16].

Generally, the adhesion of silver to the glass substrate is poor. This can be improved by depositing a chromium layer between the glass and silver, which has better adhesion to the glass. However, NPs consisting of two metals display reduced SPR. To avoid this, a different method was used, whereby a thin layer of SiO_x was deposited over the substrate containing the NPs. This additive dielectric layer influenced the SPR wavelength but, in this case, there was a red shift of only approximately 20 nm in λ_{res} (which is in agreement with previously reported results [17]). These samples did not exhibit any shifts and spreading of the plasmon resonance peak after immersion in water and subsequent drying with N_2. In addition, the SiO_x layer later functioned as a spacer layer between the NPs and the fluorescent dye.

By using the dip-coating method for the formation of the monolayer of PB and by using the SiO_x protecting layer, it has been possible to optimise the technique further in order to produce well-defined NP structures over a large area, in which the NP size can be accurately tailored to any dye spectral properties.

3.3 Fluorescence enhancement experiments

The main motivation for the investigation of the plasmonic effect is to utilise the NP-enhanced dye fluorescence to produce more efficient optical biochips. For this purpose, experiments were focused initially on the Cy5 dye, which is one of the most widely used fluorescent dyes for the labelling of biological molecules in immunoassays and biochip arrays. The absorption and the emission wavelengths are in the red spectral region($\lambda_{abs} = 649nm, \lambda_{em} = 670nm$), which is sufficiently removed from the intrinsic fluorescence of most biological materials, thereby suppressing the background noise. The nanosphere lithographic method was chosen as an appropriate method for the production of nanostructured substrates and the dependence of the enhanced fluorescence on the nanoparticles' plasmon resonance wavelength was studied. Two methods for the deposition of the fluorescent dye were used. The first was based on pin-printing fluorescent dots onto the substrate and the second was based on the non-specific adsorption of dye labelled antibodies onto the substrate.

3.3.1 Experimental

Fluorescence detection

The fluorescence signal from the enhancement chips was recorded at the emission wavelength of Cy5 ($\lambda_{em} = 670nm$) via a fluorescence laser scanner (GMS 418 Array Scanner, Genetic MicroSystems). The intensity of the fluorescence signal was represented using gray-scale mapping.

Pin-printing method

1 μg of Cy5 was diluted in 16ml of deionised water and was stored in a fridge at 4^{O}C. Small dots of the Cy5 solution were printed onto the nanoparticle-coated glass slides using a MicroSys 5100 pin-printer (Cartesian Technologies) . The dots were printed in an array with a spacing of 0.5mm x 0.5mm. The diameter of the dots was approximately 0.1mm.

Labelled antibodies

Upon deposition of a NP layer onto a glass slide, as described above, the slide was silanised using a 10% v/v solution of glycidoxypropyltrimethoxysilane mixed with a 50:50 solution of methoxyethyl ether in pH 1water. Cy5-labelled antiBSA antibodies were attached using a polydimethylsiloxane (PDMS) flow-cell. The antibody solution was left for 1 hour to attach and the cell was than flushed with deionised water. The slide was then dried with N_2. For this experiment, a portion of the slide was not coated with NPs in order to act as a reference.

3.3.2 Results

Dependence of the enhancement on plasmon resonance wavelength

Figure 3.10: A scan of pin-printed Cy5 dots on a slide covered with NPs (λ_{res}=686nm). The last 3 columns are printed on the plain substrate.

In the first experiment, the fluorescence enhancement due to the NPs was confirmed. Nanoparticles with λ_{res} =686 nm were deposited on a glass slide via nanosphere lithography. Subsequently,several dots of the aqueous solution of Cy5 were pin-printed onto both the NP-coated and reference area of the slide. The fluorescence scan of such a sample is shown in figure 3.10. In the figure, the first 9 columns are printed onto the NP-coated substrate and last 3 columns are printed on the plain the substrate. The difference between the fluorescence intensity from the dye with and without nanoparticles was clearly visible.

In the next step, several chips with NP-layers were prepared, where λ_{res} was varied by adjusting the nanoparticle size. Nanoparticles with λ_{res} spanning the absorption and emission regions of the Cy5 dye, were generated using PBs with a diameter of 500 nm and varying the thickness of the deposited silver layer (see figures 3.7 and 3.8). Columns of Cy5 dots were printed onto chips, which were covered with NPs of gradually increasing λ_{res}. In addition, a few columns of Cy5 dots were printed onto the part of the chips which was not covered with NPs, for

use as a reference. The fluorescence from the dots was then recorded using fluorescence scanner. The fluorescence was integrated over a 1 mm^2 area around each dot (dot diameter 0.1 mm^2). After background subtraction, the fluorescence was compared with an average fluorescence signal from the reference dots. The data from different samples were averaged and the resulting experimental dependence of the enhancement factor on the position of the plasmon resonance is shown in Figure 3.11. A maximum enhancement factor of approximately 8 was achieved for values of λ_{res} ranging from 645 nm to 695 nm. This corresponds to the maximum overlap with the emission and absorption wavelengths of Cy5. There is a steady decrease in the enhancement factor for values of λ_{res} greater than 695 nm and there is no significant enhancement above 760 nm.

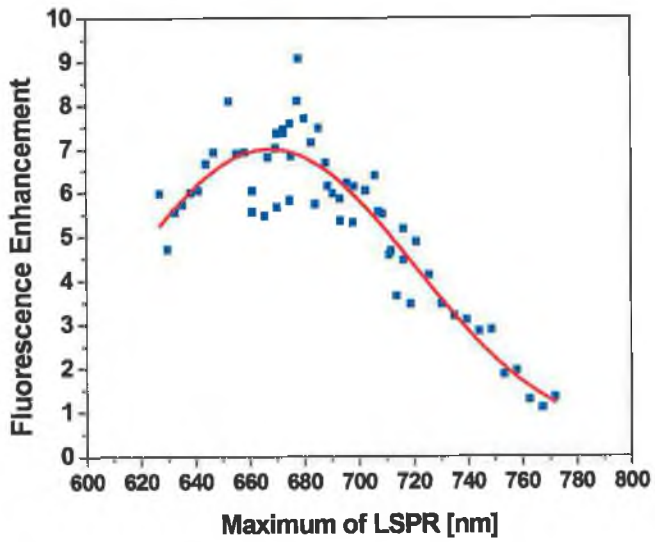

Figure 3.11: The dependence of the enhancement factor on λ_{res}.

Enhancement of fluorescence from dye labelled antibodies

Alternatively to the pin printing dyes on the substrates and measuring the plasmonic enhancement effect, the dyes were conjugated to the antibodies, which were than adsorbed to the substrate. This approach more closely corresponds to the detection process in biosensors. Figure 3.12 shows an image of the fluores-

cence from a slide coated with Cy5-labelled antibodies. In this image, part A corresponds to a reference area of labelled antibodies on glass without NP, while part B shows the fluorescence from antibodies immobilised on the metal NP layer. Clearly, the fluorescence from part B is considerably enhanced compared to part A.

Figure 3.12: Image of fluorescence from labelled antibodies on the chip. Part A: antibodies on the plain region of the substrate (reference) Part B: antibodies on the NP-coated region of the substrate (λ_{res} =674nm).

3.4 Conclusion

In this chapter, two methods of production of metal nanoparticles were introduced. The ability to produce nanoparticles supporting localised surface plasmon resonance at a range of wavelengths was examined, as well as the impact of the λ_{res} on the effectiveness of the fluorescence enhancement effect. Using the thermal evaporation method, large areas of silver and gold nanoparticles exhibiting plasmon resonance were prepared. However, nanoparticles prepared with this method exhibited plasmon resonance over only a narrow range of the visible spectrum and the method did not facilitate a high degree of variation of the nanoparticle size. In contrast, nanostructured films supporting localised plasmon resonance over a broad range of wavelengths were prepared using nanosphere lithography. In order to use this technique, a dip-coating apparatus was built and the process of layer self-assembly was optimised. The experimental dependence of the plasmon resonance on the geometrical size of the nanoparticle was measured. The disadvantages of this technique are its long duration and the restriction that only

very flat substrates can be used due to the self-assembly process. Subsequently, the ability of such layers to enhance fluorescence from dyes emitting in the red region of the visible spectrum was examined. The results obtained confirmed the enhancement of fluorescence from Cy5 dye that was placed in the proximity of NP layers that were correctly tuned to the optical properties of the dye. Additionally, an enhanced fluorescent signal from dye labelled antibodies was observed, which indicated the possibility of using the nanostructured platforms in bio-sensing applications.

Bibliography

[1] S. W. Kennerly, J. W. Little, R. J. Warmack, and T. L. Ferrell. Optical-properties of heated ag films. *Physical Review B*, 29(6):2926–2929, 1984.

[2] P. Orfanides, T. F. Buckner, M. C. Buncick, F. Meriaudeau, and T. L. Ferrell. Demonstration of surface plasmons in metal island films and the effect of the surrounding medium - an undergraduate experiment. *American Journal of Physics*, 68(10):936–942, 2000.

[3] A. Werner and H. Hibst. Particulate au and ag films for optical-recording. *Applied Optics*, 28(7):1422–1428, 1989.

[4] K. Baba, Y. Ohkuma, T. Yonezawa, and M. Miyagi. Silver-based compound metal island films for write-once optical data-storage media. *Applied Optics*, 40(16):2796–2804, 2001.

[5] P. Royer, J. P. Goudonnet, R. J. Warmack, and T. L. Ferrell. Substrate effects on surface-plasmon spectra in metal-island films. *Physical Review B*, 35(8):3753–3759, 1987.

[6] H. W. Deckman and J. H. Dunsmuir. Natural lithography. *Applied Physics Letters*, 41(4):377–379, 1982.

[7] J. R. Krenn, G. Schider, W. Rechberger, B. Lamprecht, A. Leitner, F. R. Aussenegg, and J. C. Weeber. Design of multipolar plasmon excitations in silver nanoparticles. *Applied Physics Letters*, 77(21):3379–3381, 2000.

[8] J. C. Hulteen and R. P. Van Duyne. Nanosphere lithography: A materials general fabrication process for periodic particle array surface. *J. Vac. Sci. Tachnol. A*, 13(3):1553–1558, 1995 May/Jun.

[9] T. R. Jensen, M. L. Duval, K. L. Kelly, A. A. Lazarides, G. C. Schatz, and R. P. Van Duyne. Nanosphere lithography: Effect of the external dielectric medium on the surface plasmon resonance spectrum of a periodic array of sliver nanoparticles. *Journal of Physical Chemistry B*, 103(45):9846–9853, 1999.

[10] C. L. Haynes and R. P. Van Duyne. Nanosphere lithography: A versatile nanofabrication tool for studies of size-dependent nanoparticle optics. *Journal of Physical Chemistry B*, 105(24):5599–5611, 2001.

[11] Z. P. Huang, D. L. Carnahan, J. Rybczynski, M. Giersig, M. Sennett, D. Z. Wang, J. G. Wen, K. Kempa, and Z. F. Ren. Growth of large periodic arrays of carbon nanotubes. *Applied Physics Letters*, 82(3):460–462, 2003.

[12] H A Bullen and S J Garrett. Tio2 nanoparticle arrays prepared using a nanosphere lithography technique. *Nano Letters*, 2(7):739–745, 2002.

[13] F. Burmeister, W. Badowsky, T. Braun, S. Wieprich, J. Boneberg, and P. Leiderer. Colloid monolayer lithography-a flexible approach for nanostructuring of surfaces. *Applied Surface Science*, 145:461–466, 1999.

[14] W Frey, C K Woods, and A. Chilkoti. Ultraflat nanosphere lithography: A new method to fabricate flat nanostructures. *Advanced Materials*, 12(20):1515–1519, 2000.

[15] P A Kralchevsky and N D Denkov. Capillary forces and structuring in layers of colloid particles. *Current Opinion in Colloid & Interface Sci.*, 6:383–401, 2001.

[16] K. L. Kelly, E. Coronado, L. L. Zhao, and G. C. Schatz. The optical properties of metal nanoparticles: The influence of size, shape, and dielectric environment. *Journal of Physical Chemistry B*, 107(3):668–677, 2003.

[17] T. R. Jensen, M. D. Malinsky, C. L. Haynes, and R. P. Van Duyne. Nanosphere lithography: Tunable localized surface plasmon resonance spectra of silver nanoparticles. *Journal of Physical Chemistry B*, 104:10549–10556, 2000.

Chapter 4

Plasmonic enhancement effects of colloidal metal nanoparticles in solution

This chapter describes the preparation and characterisation of colloidal nanoparticles (NPs) as well as the influence of the NPs on the emission properties of an adjacent dye molecule. Preparation of the colloidal nanoparticles was performed using a wet chemistry approach. The main advantages of this method are inexpensive production of nanoparticles in large quantities. A variety of chemical procedures was used to produce spherical nanoparticles of different sizes and compositions. Therefore, this method was examined for possible application in the enhancement of biosensors. At first, spherical nanoparticles of different composition and radius were synthesised, characterised and the optical properties were compared with theoretical predictions. Next, their plasmonic effects on a model dye, which was attached to a nanoparticle, were experimentally and theoretically studied.

4.1 Nanoparticle preparation and characterisation

The aim was to prepare nanoparticles with different characteristics and then to measure their plasmonic effects on a model dye. The model dye in our experi-

ment was the Ruthenium (II) tris (4,7 diphenyl-1,10 phenanthroline dichloride) complex (abbreviated to Ru-dpp$_3$), which has advantages of absorption at short wavelengths and a large Stokes shift. These features allowed us to use spherical gold/silver nanoparticles and, in particular, the large Stokes shift allowed us to focus only on the excitation enhancement effect. Gold/silver alloy nanoparticles with a plasmon resonance wavelength which coincides with the absorption spectrum of the Ru-complex dye were prepared by tuning the metal composition. Next, different sizes of the alloyed nanoparticles of the given composition were prepared.

4.1.1 Tuning of the plasmon resonance - theory

The extinction spectra of the spherical nanoparticles can be theoretically predicted using equations (2.58)-(2.39). If the nanoparticle is without a shell then the expansion coefficients a_n, b_n are calculated using equations (2.54)-(2.55). If the nanoparticle has a shell then expressions for the coefficients (B.1)-(B.2) (as given in appendix B) are used. Therefore, if the dimensions of the nanoparticle and its dielectric constant are known, the position of the plasmon resonance can be predicted. The plasmon resonance shifts to longer wavelength with increasing nanoparticle size and increasing thickness of the silica shell as was explained in the theory chapter (section 2.3.2).

Change of nanoparticle composition

A plasmon resonance occurs in small spherical nanoparticles if the dielectric constant of the nanoparticle is equal to minus twice the dielectric constant of the surrounding medium (see equation (2.48)). By changing the composition of the nanoparticle the dielectric constant is changed, and therefore the position of the plasmon resonance is shifted.

To calculate the extinction cross section of nanoparticles of different gold/silver ratios, the dielectric constant has to be known. For pure silver and gold the experimental values of the dielectric constants are to be found in reference [1]. But in the case of the alloy, the dielectric constant was experimentally measured only for some concentrations and wavelengths [2]. Some authors [3] use a simple model, where the dielectric constant of the alloy ε^{all} is expressed as a linear combination

of the dielectric constant of gold and silver

$$\varepsilon^{all}(x,\omega) = x\varepsilon^{Au}(\omega) + (1-x)\varepsilon^{Ag}(\omega) \tag{4.1}$$

where $x = M_{Au}/(M_{Au} + M_{Ag})$ is the gold molar ratio in the alloy. This model predicts successfully the shift of the plasmon resonance, but the profile of the peak is distorted. This is due to the fact that, using such an expression, two d-electron bands in the alloy are introduced (d-electron bands are explained in theory chapter, part 2.3.1). Therefore, we used a modified model for the dielectric constant [4] which deals separately with the contribution of d-electrons to the dielectric constant.

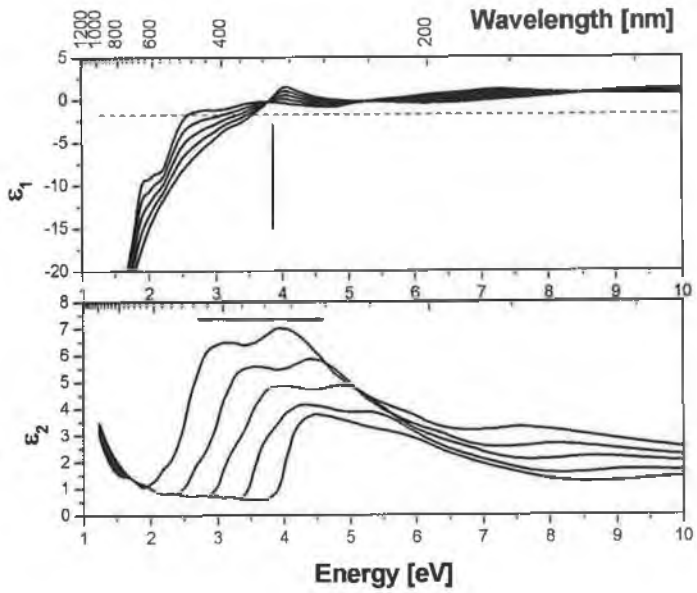

Figure 4.1: Dielectric constant of gold/silver alloy of different molar concentration based on the model described in the text. The arrow indicates the change of gold molar concentration ($x = 1, 0.75, 0, 5, 0.25, 0$). The horizontal line represents LSPR condition

In this model, confirmed by experimental values, the edge of the d-band electron absorption of the alloy ω_d^{all} depends linearly on the gold molar ratio:

$$\omega_d^{all} = x\omega_d^{Au} + (1-x)\omega_d^{Ag} \tag{4.2}$$

where ω_d^{Ag},ω_d^{Au} are the absorption edges of d-electrons in Ag and Au. The absorption edges in Ag and Au are 3.9 eV and 1.9 eV respectively. The d-band

absorption profile of the alloy for $\omega \geq \omega_d^{all}$ is described as:

$$\varepsilon_1^{all}(x,\omega) = x\varepsilon_1^{Au}(\omega_d^{Au} - \omega_d^{all} + \omega) + (1-x)\varepsilon_1^{Ag}(\omega_d^{Ag} - \omega_d^{all} + \omega) \tag{4.3}$$

For lower energy, only the s-electrons, described by the Drude model of free electrons, contribute to the dielectric constant, and so the previous model of linear combination of the dielectric functions of gold and silver is used as in equation 4.1. The real part of the dielectric constant of the alloy is calculated using the linear model.

Examples of dielectric constants of different gold/silver molar concentrations x using this model are shown in figure 4.1. The real part of the dielectric constant is in the upper graph and the imaginary part of the dielectric constant is in the lower graph. The plasmon resonance condition in equation (2.48) is represented by the dashed line in the upper section. In the graph it is clearly seen that the plasmon resonance shifts from 390nm to 520nm as a function of x. The shift of the absorption edge of d-band electrons is seen in the lower graph.

4.1.2 Experimental

Synthesis of gold/silver nanoparticles

Gold silver alloy nanoparticles with varying plasmon absorption wavelengths were prepared using the procedures reported in the literature [5, 3]. To prepare pure gold colloids, 2 ml of 1 wt % sodium citrate solution was added dropwise to a boiling solution of 5 mg of $HAuCl_4$ dissolved in 95 ml of deionised water with rapid stirring. The solution was stirred for a further 30 minutes in which time the solution changed from a light blue to a deep red colour. Gold silver alloys were prepared in the same way by substituting a predetermined number of moles of gold atoms with the equivalent number of moles of silver atoms in the form of silver nitrate $AgNO_3$. Pure silver nanoparticles could not be prepared this way.

Next, gold/silver alloy NPs with a molar ratio of 4 silver atoms to every gold and with 4 different radii were synthesized. In this case 2 ml of 1 wt % sodium citrate was added dropwise with rapid stirring to a boiling solution of silver nitrate (20.3 mmol) and chloroauric acid (5.08 mmol) dissolved in 95 ml of deionised water. The solution was stirred for a further 30 minutes in which time the solution changed from a light blue to a light red to a dark yellow colour. The

final concentration of colloid was $3.2 \cdot 10^{10}$ particles per ml. The calculation was done by dividing total amount of metal used in the synthesis and the amount of metal per one nanoparticle.

The three larger diameter NPs were synthesized using a seeded growth method whereby a seed solution containing the NP synthesized above was added with sodium citrate to an aqueous solution of chloroauric acid and silver nitrate [6]. The reduced gold and silver atoms precipitate onto the NPs in preference to the formation of new nucleating sites, thereby increasing the size of the NP seeds. For this procedure, 75 ml of boiling silver/gold seed NPs from the above procedure and 2.5 ml of 1 wt % sodium citrate was added simultaneously and with rapid stirring to a boiling solution of 23.5 mmol silver nitrate and 5.88 mmol chloroauric acid dissolved in 75 ml of deionised water. The solution was stirred for a further 30 minutes during which the solution darkens slightly in colour. The final concentration of colloid was $1.6 \cdot 10^{10}$ particles per ml with a molar ratio of 4 silver atoms to every gold and a particle radius of 27 nm. This procedure was repeated a further two times using the NP's from the previous synthesis to generate gold/silver alloy NP's with average radii of 36 nm and 40 nm.

Synthesis of the silica shell around the NP's

The formation of a silica shell upon a NPs provides a protective layer, which prevents molecules from directly attaching to the NPs and will be used in section 4.2 to tune NP-dye separation. Nanoparticles were coated with a silica shell by precipitation from a sodium silicate solution [7]. An aqueous solution of 0.5 ml of 1 mM (3-amino propyl)trimethoxysilane (APTS) was added to 100 ml of each nanoparticle sol under vigorous stirring and allowed to stand for a further thirty minutes to ensure attachment of the APTS ligand to the surface of the nanoparticles. Separately a solution of activated silica was prepared by lowering the pH of a 0.54 wt % sodium silicate solution to 10.5 with progressive additions of the cationic exchange resin. Finally, 4 ml of the activated silica solution was added to the nanoparticle solution with vigorous stirring and allowed to stand for a further 24 hours. Shell thicknesses of 5 nm were achieved using this method.

Characterisation techniques

The UV-VIS extinction spectra of the nanoparticles in water solution were measured with a Cary 50 Scan UV-Visible Spectrophotometer (Varian Ltd) in transmission mode.

TEM micrographs were obtained using a Hitachi 7000 transmission electron microscope operated at 100 kV. Images were captured digitally using a Megaview 2 CCD camera. Specimens were prepared by dropping aqueous solutions onto formvar carbon coated copper grids.

4.1.3 Nanoparticle characterisation

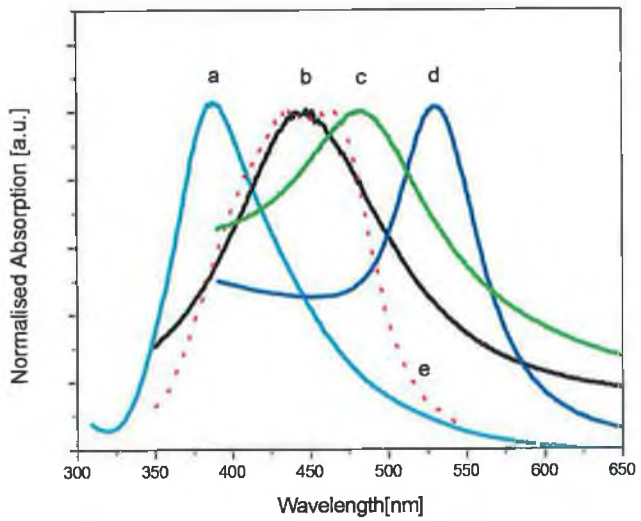

Figure 4.2: Absorption spectra of prepared silver/gold nanoparticles (radius 13nm). The peaks are around 435nm (b) and 480nm (c) correspond to 90% and 30% silver respectively. In the graph are also absorption spectra of pure silver (395nm) (radius 4nm) (a) and pure gold (530nm) (radius 13nm) (d) nanoparticles together with excitation spectra of Ru-complex dye (e).

At first the dielectric constant was tuned via different gold/silver composition in order to produce NPs with varying plasmon resonance wavelengths. Samples of gold/silver alloy and gold nanoparticles were successfully prepared (radius

13nm). Absorption spectra of the nanoparticles were measured and a selection of these spectra are presented in figure 4.2. The shift from 520nm for pure gold nanoparticles to the shorter wavelength with decreasing gold molar ratio x is clearly seen. For clarity, absorption spectra of pure silver nanoparticles (radius 4nm) (synthesis described in section 5.1) are presented in the graph as well. Figure 4.2 also includes the absorption spectrum of the Ru-complex used in later experiments to show enhanced fluorescence. A gold molar ratio of about 20% corresponded to an absorption maximum of the nanoparticles at 435nm, which most closely matched the absorption peak of the Ru-complex. As this condition of overlapping the plasmon resonance with absorption is needed for one mode of fluorescence enhancement, nanoparticles with this gold molar ratio (x=0.2) were used in further experiments.

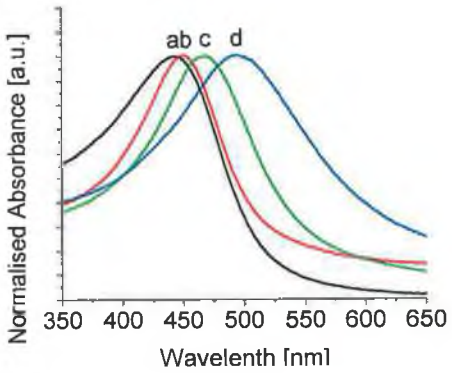

Figure 4.3: Absorption spectra of the gold/silver nanoparticles (a-13nm, b-27nm, c-36nm, d-40nm).

Next, gold/silver alloy NPs, with x of 0.2, with increasing sizes ranging from 13nm to 40 nm radius, were synthesized. The absorption spectra of all NPs were measured and the data is shown in figure 4.3. It can be seen that there is a clear LSPR peak for each size of NP and that the peak wavelength shifts to longer wavelengths with increasing size. When the 5 nm silica shell was added to the NPs, a small red shift was observed, as predicted. The presence of this shift helped to confirm the presence of the shell on the NPs. Evidence of this shift can be seen in figure 4.5. TEM microscopy was also carried out to determine exact particle size and also shell thickness. A selection of TEM images is shown in figure 4.6.

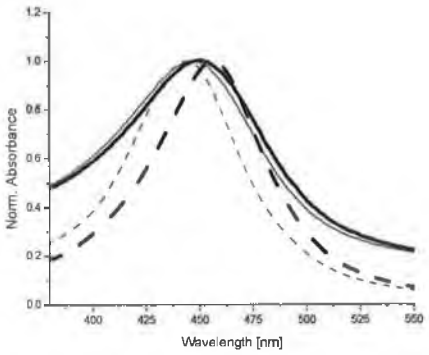

Figure 4.4: Experimental (solid line) and theoretical (dashed line) absorption spectra of the nanoparticle with radius 27nm with (thick black line)/without (thin blue line) 5nm silica shell.

	Sample1	Sample2	Sample3	Sample4
NP radius	$13 \pm 2nm$	$27 \pm 3nm$	$36 \pm 6nm$	$40 \pm 4nm$
SiO_2 thickness	$4 \pm 0.4nm$	$4.8 \pm 0.7nm$	$5.7 \pm 0.9nm$	$7.8 \pm 1.3nm$

Table 4.1: Sizes of the nanoparticles and thickness of their SiO_2 shells

These data confirm that the particles are mainly spherical and that they have a small variation in size. Average particle size and shell thickness values were measured from those data. Table 4.1 documents average NP radius and average shell thickness. Figure 4.4 shows a comparison of the theoretically computed absorption spectrum (also shown in figure 4.3) with the experimental absorption data for a NP with radius of 27 nm where the NP dimensions were measured from the TEM data. The experimental spectra are broader due to the small amount of polydispersity present. Computed and experimental data (position of LSPR peak) for all NP sizes are shown in figure 4.5. Here an average shell thickness of 5 nm was assumed for all NPs. Clearly there is close quantitative agreement between theory and experiment.

To summarise this section, nanoparticles of different gold/silver composition and sizes were prepared. Additionally, thin silica shells around the nanoparticles was synthesised. By choosing the gold molar ratio x=0.2, the plasmon resonances of nanoparticles of different sizes were positioned in the absorption spectrum of

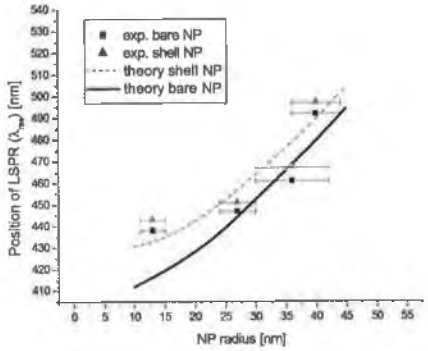

Figure 4.5: Experimental measured and theoretical predicted maxima of the absorption peaks of nanoparticle with/without silica shell (λ_{res}).

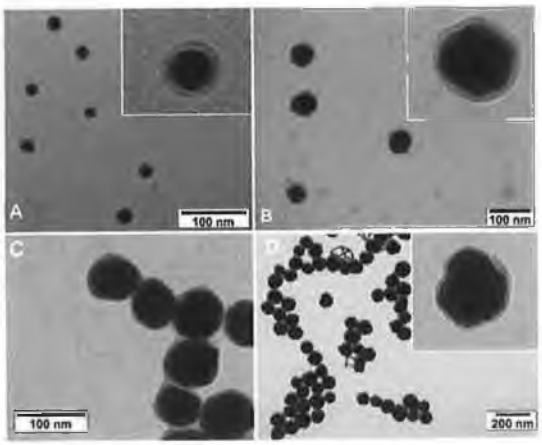

Figure 4.6: TEM images of gold/silver nanoparticles (A-Sample1, B-Sample2, C-Sample3, D-Sample4).

Ru-complex. The experimentally measured absorption spectra of the nanoparticles closely corresponded with the theoretically computed and therefore the model calculating distribution of the electric field could be applied to the computation of the excitation enhancement effect of these nanoparticles in the next section.

4.2 Fluorescence enhancement experiments

In this section, data from experiments measuring the influence of metal nanoparticles on fluorescence from a dye attached to the nanoparticles are presented. The experiments were carried out on gold/silver nanoparticles of different sizes surrounded by a silica shell (as characterised in previous section). First, fluorescence from a prepared solution of a known quantity of Ru complex was measured. Then the same measured concentration of the dye was attached to the nanoparticles and the fluorescence was again measured. The ratio of these two values represented the enhancement effect of the nanoparticle on the dye fluorescence. The maximum achievable enhancement for this system was theoretically predicted and compared with the experimentally measured values. Additionally, the experiments were repeated with silica nanoparticles in order to determine the influence of dye attachment on the emission.

4.2.1 Model description

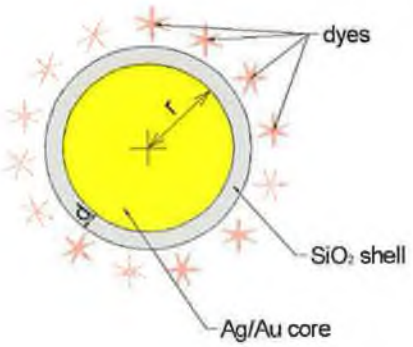

Figure 4.7: Schematic of the nanoparticle-dye system. The nanoparticle core is a gold/silver alloy (20% gold) of different radii (r=13-40nm); the shell is silica of thickness d=5nm; Ru dye molecule are attached uniformly to the silica shell with isotropic orientation of the dipole.

Based on our experimental protocol, we consider Ru complex molecule attached to the nanoparticle with a silica shell. The nanoparticle is composed of a gold/silver alloy with a gold molar ratio x=0.2 and the radius varies from 13nm to 40nm. The thickness of the silica shell is set to 5nm. Further, the orientation

of the dipole of the fluorescent dye is considered to be isotropically distributed. A schematic of the nanoparticle-dye system is shown in figure 4.7. The excitation spectra of the dye complex is quite flat from around 410 to 490nm and the maximum of emission is at 620nm (see figure 4.10, dashed line). The quantum efficiency of the dye is around 0.5.

As explained in section 2.4 of chapter 2, there are two major plasmonic enhancement effects: excitation enhancement and emission enhancement. The excitation enhancement is caused by the increase of the electric field of the incident field. Due to the geometry of the system (figure 4.7), the average excitation enhancement is the ratio of fluorescence excitation of dyes isotropically distributed over the nanoparticle with isotropic distribution of the dipole orientation and the fluorescence excitation of free dyes. This enhancement, $\overline{R_{ex}}$, is calculated using equations (2.68),(2.53), (B.1), (B.2).

The emission of the dye is altered also. The fluorescence does not increase if the quantum efficiency of the dye is too high and if the plasmon resonance does not coincide with the emission wavelength. However, the quantum efficiency of the dye can decrease due to the non-radiative de-excitation resulting from dye-NP proximity [8]. For this reason, the dyes were not attached directly onto the nanoparticle but a silica shell of 5nm thickness was added. At such distances the excitation enhancement is still significant and should overcome the negative effect of the quenching, which is much less than at zero distance [9, 10, 11]. Therefore, the numerically calculated excitation enhancement $\overline{R_{ex}}$ is the maximum enhancement of the fluorescence for this system and, depending on the strength of the quenching, the experimentally measured enhancement will be less than this.

4.2.2 Experimental

Protocol for normalized fluorescence measurement

The fluorescence enhancement is measured by comparing the signal from the NP-dye system to that of the equivalent dye concentration without the NPs. Firstly, the optimum concentration of NPs in solution must be chosen in order to take account of inner filter effects [12] which are caused by the strong absorption of the NP's. If the NP concentration is too high, the intensity of illumination rapidly decreases throughout the sample which makes it impossible to compare it to

the solution without NP's. On the other hand, too low a concentration of the nanoparticles would mean too low a concentration of the dye which would be undetectable. Hence, an optimum NP dilution was established empirically based on the two limiting situations discussed above. This optimum dilution corresponds to an absorbance of the NP solution in a 1 cm cuvette of approximately 0.3. The resulting concentration of nanoparticles in solution was about $3 \cdot 10^9$ particles per ml. Next, the dye concentration required to form a monolayer on the NP surface was estimated from the concentration of colloids and from the geometrical size of the dye and found to be 10^{-7} M. The reference solution used was a 10^{-5} M solution of the dye in ethanol since the dye is not very soluble in water at high concentration. Self-quenching of the dye was not expected because of the large Stokes shift. The details of the fluorescence measurement are as follows for each NP diameter: 1 ml of the NP solution and 1ml of deionised water were stored in Eppendorf tubes. 10 ml of 10^{-5} M ruthenium dye standard was added to the tubes. Aliquots of 100 ml were placed in black microplate wells and the fluorescence was measured with a Safire (Tecan) microplate reader. For the NP-dye and pure dye solutions, the excitation wavelength matched both the LSPR of the NPs and the absorption band of the dye.

Synthesis of the silica nanoparticles

Monodispersed samples of silica nanoparticles were prepared using a micro emulsion method [13]. The radius of the silica nanoparticles was 30nm. Nanoparticles were redispersed in deonised water to a concentration matching that of gold-silver alloys.

4.2.3 Enhancement results

Calculated enhancement

Figure 4.8 shows the dependence of the calculated enhancement factor on excitation wavelength for different NP sizes, each surrounded by a silica shell of 5nm thickness. From data, it can be seen that for each NP size, there is a maximum wavelength of the enhancement. From the data in figure 4.8, the dependence of enhancement at maximum enhancement wavelength with NP radius can be

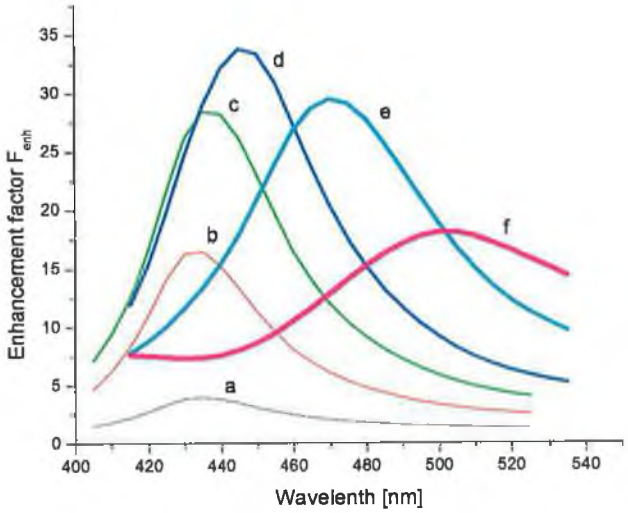

Figure 4.8: Calculated dependence of the enhancement factor $\overline{R_{ex}}$ on the excitation wavelength for different nanoparticle sizes. Parameters: gold/silver molar extinction x=0.2, thickness of the silica shell d=5nm. Radius of the nanoparticles a-5nm, b-10nm, c-15nm, d-20nm, e-30nm, f-40nm.

plotted. This is shown in figure 4.9 and indicates that maximum fluorescence enhancement should occur for a radius in the region of 20-25 nm. This dependence on NP size is explained as follows: if the NP is much smaller than the illumination wavelength, the E-field amplitude on the surface does not depend on the NP size and is inversely proportional to the ratio of NP-dye distance and NP radius. This corresponds to the electrostatic approximation. Therefore, for a constant NP-dye distance, the E-field amplitude increases with NP radius up to a point where the electrostatic approximation no longer holds. This is the case for larger NP sizes (radius $\sim$ 0.1 times the wavelength) where the LSPR effect is weaker and the amplitude of the field decreases (see section 2.4.1 in theory chapter).

This excitation enhancement will be decreased by the decrease of the quantum efficiency of the dye. In the approximation of a small distance limit (section 2.4.2 in theory chapter) the decrease should not depend on the size of the nanoparticle and, therefore, the dependence of the total enhancement on the nanoparticle size should be similar to the dependence of the excitation enhancement on the size as

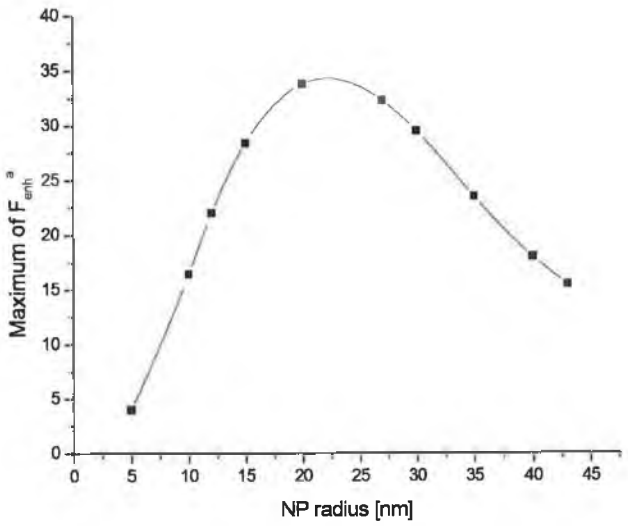

Figure 4.9: Calculated dependence of the maximum enhancement on the nanoparticle size. Parameters: gold/silver molar extinction x=0.2, thickness of the silica shell d=5nm.

in figure 4.9.

Estimation of fluorescence enhancement factor

The protocol for measurement of the fluorescence enhancement factor was described in the previous subsection. Both emission and excitation spectra were measured for (i) the NP-dye combination in solution and (ii) the same concentration of dye in solution without the NPs. In these experiments, the excitation spectra were measured at an emission wavelength of 620 nm and the emission was measured for excitation wavelengths corresponding to the maximum in excitation spectra. Figure 4.10 shows the data for a NP of radius 27 nm . It can be seen from the data that there is an enhancement factor of 4 in both excitation and emission. The fluorescence enhancement, defined as the ratio between the emission intensity of NP-dye and that of dye alone, has been measured for all NPs and is plotted in figure 4.11 as a function of NP radius. From this, it can be seen that the maximum enhancement factor is 4 for NP of radius 27nm, while no enhancement was measured for the smallest NP (radius = 13nm). The

enhancement also drops off after a radius of 27 nm.

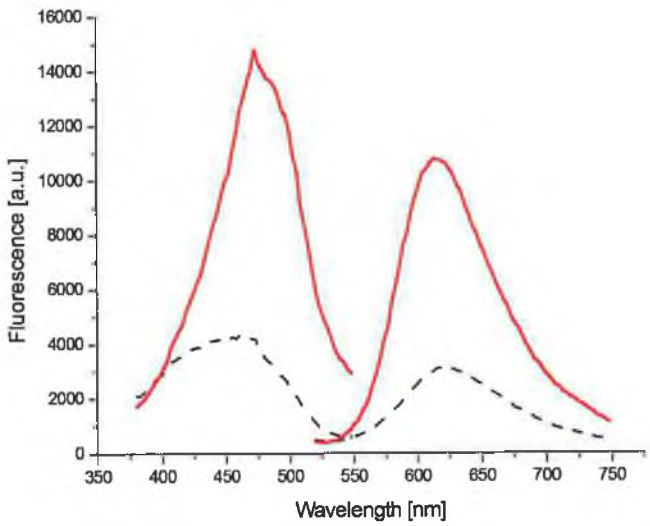

Figure 4.10: Excitation and emission spectra of the Ru-dye in a water solution (dashed line) and in the solution with 27nm radius nanoparticles (solid line) Sample2.

In a separate experiment it was confirmed that the enhancement of the fluorescence was due to the LSPR and that the enhancement factor was not influenced by the attachment of the fluorescent dye to the surface of the silica shell coating the NPs. Prior to the experiment, silica nanoparticles were prepared as described in section 4.1.2. The size of the silica nanoparticles was chosen to be approximately the same as the size of metal nanoparticles giving the biggest enhancement (radius 27nm). The silica nanoparticles were analysed by TEM (see figure 4.12) and the diameter of the nanoparticles was determined to be 60nm. In the next step, the protocol for measurement of the fluorescence enhancement factor was repeated where, instead of metal nanoparticles (radius 27nm), silica nanoparticles (radius 30nm) of the same concentration were used. The recorded fluorescence spectra from the dye attached to the silica NPs and from free dye in solution were almost identical. This indicated that the attachment of the dye to the silica does not influence the emission properties of the dye (quantum efficiency) and therefore the observed enhancement of the fluorescence from the dye attached to

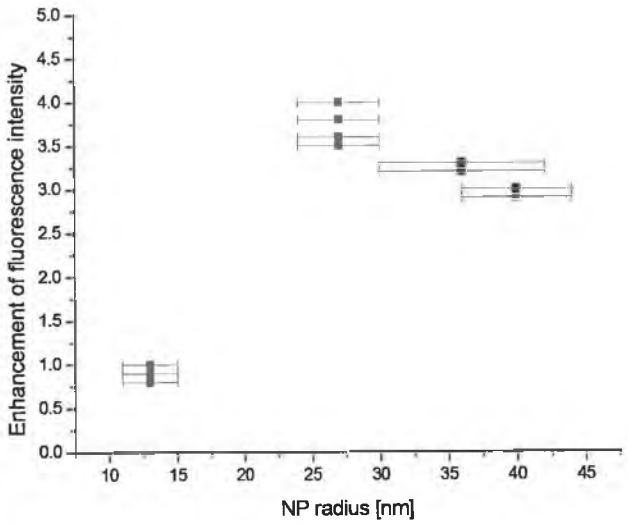

Figure 4.11: Experimentally measured dependence of the fluorescence enhancement on the size of the nanoparticles.

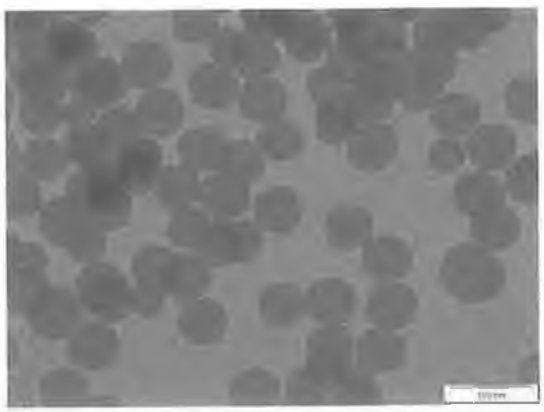

Figure 4.12: TEM image of silica nanoparticles. Average radius of the nanoparticles is 30nm.

gold silver NPs coated with a silica shell is only due to the LSPR.

Next, the experimental data in figure 4.11 were compared with the maximum achievable enhancement values in figure 4.9. There is qualitative agreement with respect to the dependence on NP size and the measured enhancement factor is about 9 times less than that predicted. This indicated that the induced

non-radiative de-excitation rates are still quite significant at the nanoparticle-dye distance 5nm leading to the decrease of the quantum efficiency of the dye. Further, from the similar dependence of the enhancement on the nanoparticles' size it follows that the quenching does not significantly vary with the nanoparticles' size in the range between 13nm to 40nm. This estimation of the quenching could also depend on effects such as the presence of some unbound dye. In this case, the unbound dye will not contribute to the enhancement due to the increased separation.

4.3 Conclusion

In this section, experiments studying the plasmonic effect of colloidal nanoparticles on fluorescent dyes in solution were carried out. First, colloidal spherical nanoparticles with different optical properties were synthesised. The focus was on gold/silver alloy nanoparticles, where by changing the gold molar ratio, the plasmon resonance was tuned over 100nm. Next, gold/silver alloy nanoparticles with gold molar ratio x=0.2 of four different radii were synthesised and a silica shell of desired thickness was produced. All these nanoparticles were characterised by absorption spectroscopy and transmission electron microscopy. The absorption spectra compared well with those computed theoretically. Second, the enhancement of fluorescence due to the presence of the nanoparticles in solution was experimentally observed, and the dependence of the fluorescence enhancement on the size of the nanoparticles was measured. The biggest enhancement was achieved for nanoparticles with 27nm radius, which coincides with the calculated optimum radius. The experimental values of the enhancement were on average 9 times lower than the theoretically predicted value. This is most likely an indication of the presence of a quenching effect due to dye-NP proximity.

Bibliography

[1] E. D. Palik, *Handbook of Optical-Constants*, vol. 1 of *Journal of the Optical Society of America a-Optics Image Science and Vision*. Academic Press Inc., 1984.

[2] K. Ripken, "Die optischen konstanten von au, ag und ihren legierungen im energiebereich 2.4 bis 4.4 ev," *Z. Physik*, vol. 250, pp. 228–234, 1972.

[3] S. Link, Z. L. Wang, and M. A. El-Sayed, "Alloy formation of gold-silver nanoparticles and the dependence of the plasmon absorption on their composition," *Journal of Physical Chemistry B*, vol. 103, no. 18, pp. 3529–3533, 1999.

[4] M. Gaudry, J. Lerme, E. Cottancin, M. Pellarin, J. L. Vialle, M. Broyer, B. Prevel, M. Treilleux, and P. Melinon, "Optical properties of (auxag1-x)(n) clusters embedded in alumina: Evolution with size and stoichiometry," *Physical Review B*, vol. 6408, no. 8, pp. art. no.–085407, 2001.

[5] J. Turkevich, P. C. Stevenson, and J. Hillier, "A study of the nucleation and growth processes in the synthesis of colloidal gold," *Discuss. Faraday Soc.*, vol. 11, p. 55, 1951.

[6] K. R. Brown, D. G. Walter, and M. J. Natan, "Seeding of colloidal au nanoparticle solutions. 2. improved control of particle size and shape," *Chemistry of Materials*, vol. 12, no. 2, pp. 306–313, 2000.

[7] L. M. LizMarzan, M. Giersig, and P. Mulvaney, "Synthesis of nanosized gold-silica core-shell particles," *Langmuir*, vol. 12, no. 18, pp. 4329–4335, 1996.

[8] T. Huang and R. W. Murray, "Quenching of [ru(bpy)3]2+ fluorescence by binding to au nanoparticles," *Langmuir*, vol. 18, pp. 7077–7081, 2002.

[9] P. Anger, P. Bharadwaj, and L. Novotny, "Enhancement and quenching of single-molecule fluorescence," *Physical Review Letters*, vol. 96, p. 113002, 2006.

[10] C. Mayer, N. Stich, T. Schalkhammer, and G. Bauer, "Slide-format proteomic biochip based on surface-enhanced nanocluster-resonance," *Fresenius Journal of Analytical Chemistry*, vol. 371, pp. 238–245, 2001.

[11] K. Sokolov, G. Chumanov, and T. M. Cotton, "Enhancement of molecular fluorescence near the surface of colloidal metal films," *Analytical Chemistry*, vol. 70, no. 18, pp. 3898–3905, 1998.

[12] D. Rendell, *Fluorescence and Phosphorescence.* John Wiley & Sons Ltd, 1987.

[13] S. Santra, K. Wang, R. Tapec, and W. Tan, "Development of novel dye-doped silica nanoparticles for biomarker application," *JOURNAL OF BIOMEDICAL OPTICS*, vol. 6, no. 2, pp. 160–166, 2001.

Chapter 5

Plasmonic enhancement of NPs on planar substrates

This chapter describes the preparation and characterisation of substrates coated with NPs as well as the influence of the NPs on the emission properties of an adjacent dye molecule. Techniques for synthesis of large silver spherical NPs and silver triangular-shaped NPs of different sizes are presented. In addition, layer-by-layer deposition techniques for the deposition of nanometer thick polymer films upon substrates is introduced and characterisation of these deposited layers is undertaken. Subsequently, these polymer layers are used for immobilisation of NPs on the substrates. The topography of these NP-modified films and the dependence of the localised surface plasmon resonance upon various parameters are studied. In the last part of the chapter, experiments dealing with enhanced fluorescence from dyes conjugated in polymers films and deposited on the NP-structured substrates are described. The dependence of the fluorescence intensity on various parameters such as type of NP, the NP-dye separation, and the specific type of dye used was investigated.

5.1 Colloidal silver nanoparticles

In chapter 4 the preparation of gold/silver alloy NPs in a solution was presented. In this section another procedure for synthesis of pure silver spherical NPs, as well as production of triangular shaped NPs of different sizes is introduced. After

the synthesis of these NPs, they were characterised by absorption spectroscopy and by transmission electron microscopy techniques.

5.1.1 Spherical nanoparticles

This section describes the preparation and characterisation of large silver NPs, where a diameter of around 60nm was chosen according to the results of the preceding chapter. An advantage of this method is that this synthesis requires fewer steps than the formation of gold/silver NPs of the same size.

Synthesis

Silver NPs, 60 nm ± 11 nm in diameter were prepared by reducing silver nitrate with sodium citrate in the presence of aniline [1]. Briefly, 4 ml of $AgNO_3$ (0.02 M) and 4 mL of aniline (0.02 M) were dissolved in 104 mL of deionised water and purged with nitrogen. The solution was heated to boiling and 8 mL of 1 wt % sodium citrate added with rapid stirring. The solution was refluxed for thirty minutes during which time the solution changed colour from clear to dark brown. The solution was centrifuged at 4500 rpm for 2 hours and doubly concentrated in deionised water. The colloid was stored in a polystyrene bottle at 4 ^{o}C. The final concentration of colloid was estimated to be $1.6\text{x}10^{13}$ particles per mL and the sample had an absorption band at 440 ± 60 nm.

Characterisation of the NPs

After synthesis these NPs were characterised via transmission electron microscopy. An image of the NPs is shown in figure 5.1, section (b). The average diameter of 60±11 nm was obtained by measuring the size of the NPs from micrographs. Absorption spectra of the NPs exhibited a clear plasmon resonance peak at 440nm (figure 5.1, section (a), black solid line) and this agreed closely with the theoretically computed absorption spectra of 60nm silver NPs (red dotted line). The small shift of about 10nm and the broader peak in the LSPR was probably caused by the polydispersity of the sample.

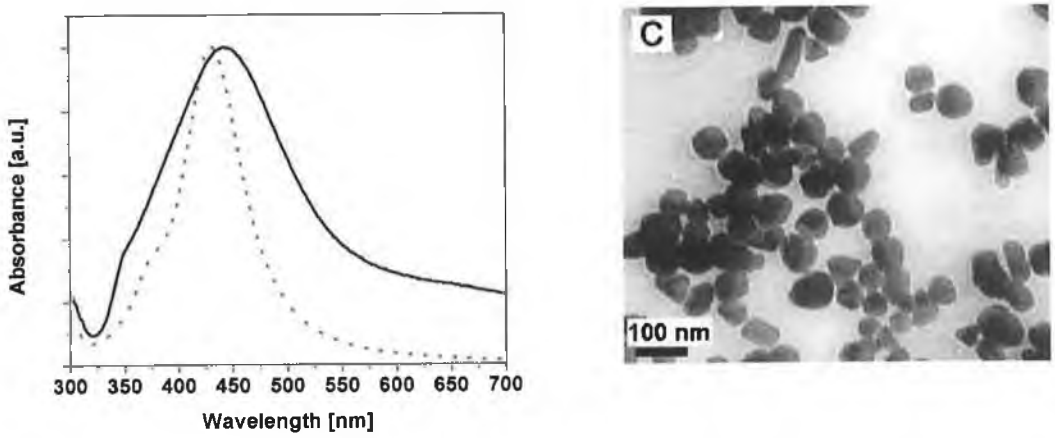

a b

Figure 5.1: (a) Experimentally measured (black solid line) and theoretically predicted (red dashed line) absorption spectra of silver NPs (60±11nm). (b) Transmission electron micrographs of the silver NPs.

5.1.2 Triangular-shaped nanoparticles

The disadvantage of these spherical NPs is that the spectral position of the plasmon resonance can not be significantly shifted and is restricted to the short wavelength region of the visible spectrum (section 2.3.2). Therefore, non-spherical NPs have to be used if the spectral position of the localised plasmon resonance is required to be in red part of the visible spectrum (section 2.3.2). There are several publications describing the synthesis of colloidal non-spherical NPs and an overview of different methods for production of nanotriangles, nanorods or nanocubes is given, for example,in reference [2]. In these experiments it was decided to use a photo-conversion method for production of triangular NPs [3, 4]. This method is based on a wet chemistry approach, where, in the first step, small silver spherical NPs are synthesised and, afterwards, the solution is illuminated by monochromatic light, which causes the transformation of the spherical NPs into triangular shaped NPs.

Figure 5.2: Process of formation of triangular shaped NPs. First, spherical NPs are split into nanometer size clusters after illumination. Second, triangular shaped NPs are formed from these clusters by illumination.

Photoconversion process

The production of triangular shaped NPs can be described in two steps. First, tiny colloidal silver NPs (diameters $\sim$ 8nm) are synthesised. Next, the solution is illuminated with a 'monochromatic' light source for several hours. Depending on the illumination wavelength, triangular shaped NPs of different sizes are produced. The exact principle of the growth of tringular shaped NP from spherical NP is still a matter of debate, but the process of the formation of the nanoprisms follows the scheme depicted in figure 5.2 [3]. First, spherical NPs are split into nanometer size clusters ($\sim$2nm) at the beginning of the illumination. Second, triangular shaped NPs are formed from these clusters by the aggregation of the clusters, where the size of the nanoprism formed, and therefore their localised plasmon resonance depends on the illumination wavelength. The longer the illumination wavelength the larger the size of the NPs. The influence of the light on the formation of NPs is observed not only in the solution by the wet chemistry approach, but also by formation of NPs by vacuum deposition [5].

We postulate that the photoconversion process is due to the plasmon resonance in the nanoprisms. The evidence for this is that the illumination wavelength coincides closely with plasmon resonance of the formed nanoprism. Therefore, the NPs can maximise the dissipation of the light energy, which is a process that is energetically preferable in physical systems.

An effect occurring during the photoconversion is the aggregation of the nanoprisms, which influences the size distribution of the NPs. Some nanoprisms in the solution aggregate and form triangles of a double size consisting of four initial triangles. This larger triangle exhibits LSPR at longer wavelengths, which is then observable in the absorption spectrum. This kind of aggregation can

be avoided by simultaneous illumination of the solution by UV-light during the photoconversion process as reported in reference [3]. The authors state that the prevention of the aggregation is caused by inducing quadrupole LSPR in the nanoprisms, which is in the UV-region of the spectrum. However, we discovered experimentally that if the sample is illuminated with the UV-light prior to the photoconversion process then the aggregation is also minimised. From this observation we suggest that the UV-light promotes the splitting of the spherical NPs into small clusters (see figure 5.2), which in turn speeds up the self photoconversion process and therefore avoids the aggregation.

Experimental procedure

Small silver NPs were synthesised using a similar procedure to that used in reference [3]. Initially, all glassware was siliconised using chloroform prior to the wet chemistry fabrication, so that the glassware would be hydrophobic. 2ml of 5mM silver nitrate ($AgNO_3$) was combined with 1ml of 30mM trisodium citrate (a weak reducing agent) in 95ml of H_2O under a nitrogen atmosphere. In parallel, a 50mM sodium borohydride solution ($NaBH_4$) (strong reducing agent) was prepared separately in ice-cold water. 1mL of this $NaBH_4$ solution was than quickly added via syringe to the silver-citrate solution in the round-bottomed flask under vigorous stirring. Following 15-30 seconds of stirring, 1mL of 5mM bis(p-sulfonatophenyl)phenyl phosphine dipotassium dihydrate (BSPP) was added to the colloid. The BSPP provides the protecting groups avoiding segregation. The colloid was then stirred for another 15 minutes.

Next, the solution of the NPs was transferred into plastic cuvettes illuminated with an array of ultra bright UV-LEDs (illumination wavelength 376nm) for around 6 hours. In the following step the cuvettes were placed in one of the illumination chambers consisting of arrays of ultra-bright LEDs. Three chambers with illumination wavelengths of 460nm, 550nm and 600nm were constructed. The chambers consisted of LEDs, which had an illumination intensity from 5 to 10 cd depending on the illumination wavelength. An example of such a chamber is shown in figure 5.3. The NP solution remained in the chamber until there was no change in the absorption of the solution. This indicated the termination of the photoconversion process. The total time varied with the intensity of the illu-

Figure 5.3: LED chamber with 2 x 20 ultra bright LEDs with wavelength 550nm powered by a current source.

mination, the illumination wavelength, and the quality of the spherical colloidal solution. On average, the termination time was 10 hours, 24hours and 50 hours for illumination wavelength 460nm, 550nm and 600nm respectively.

Results of the photoconversion process

Small silver spherical NPs were synthesised and their absorption spectrum is shown in figure 5.4 (curve a). The NP solution exhibits LSPR at 395nm. By comparing the absorption spectra with theoretically computed spectra, the average NP diameter was determined to be 10nm. Following the protocol described in the previous section, three different types of triangular NPs were produced. Their absorption spectra are shown in figure 5.4 (curves B,C,D). The absorption spectra of the triangles exhibit three peaks corresponding to the dipole resonance in plane, quadrupole resonance in plane and, quadrupole resonance out of the plane (for example curve c 548,420,338nm respectively) as identified in reference [6] (see also section 2.3.2). The positions of the dipole LSPR in these three solutions were 480nm, 548nm and 705nm respectively. The nanoprisms were also analysed by transmission electron microscopy. The micrographs are shown in figure 5.5. The triangular shape of the NPs is clearly visible, and the change of the size with the illumination wavelength was also confirmed. The NPs are not completely monodisperse. In the solutions there were present some small triangles, whose growth was terminated by the lack of small spherical NPs in the solution, and large triangles (especially using 600nm illumination) which were caused by the

aggregation process described earlier. Excluding these triangles from the analysis, the average size of the triangles was estimated to be 20nm, 99nm and 163nm for illumination wavelength 460nm, 550nm and 600nm, respectively.

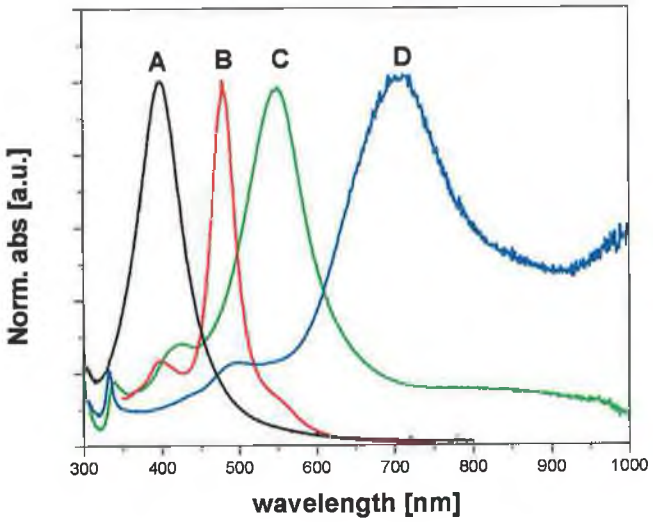

Figure 5.4: Absorption spectra of spherical silver NPs (A) and triangular NPs. Illumination wavelengths were (B) 460nm, (C) 550nm, (D) 600nm.

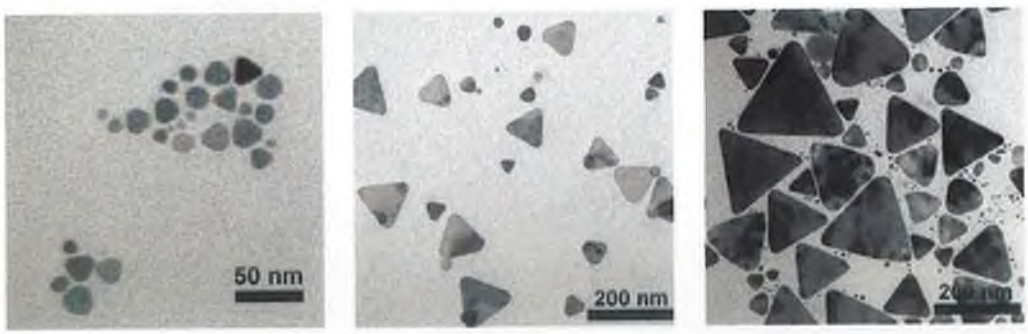

Figure 5.5: Transmission electron micrographs of triangular silver NPs prepared by photoconversion. Illumination wavelengths: a 460 nm, b 550 nm, c 600 nm.

5.2 Layer-by-layer deposition technique

In the preceding experiments in chapters 3 and 4 inorganic silicon oxide layers were used to control the distance between NPs and dye. The vacuum deposition of silicon monoxide or the precipitation of sodium silicate in aqueous solution was used, but these techniques have been found to have certain restrictions. The vacuum deposition technique was too cumbersome and the adhesion of the layers was not optimal. The precipitation method lacked the possibility of the thickness control over a wider range. In recent years, a new technique called Layer-by-Layer deposition (LbL) has been reported and this enables the formation of ultra thin layers on substrates, where the thickness is controlled with nanometer precision. A review of this technique is given in references [7, 8, 9, 10, 11]. Moreover, this technique allows the modification of substrates such that the NPs, dyes or bio-molecules can be attached to them [12, 13, 14, 15].

In order to deposit these layers reproducibly (and with the desired thickness range and roughness of the layers) several parameters in the experimental procedure were optimised and the layers were characterised via ellipsometry and atomic force microscopy. Furthermore, polyelectrolytes with conjugated dyes were synthesised and their deposition was confirmed via absorption spectroscopy.

5.2.1 Principles of the LbL technique

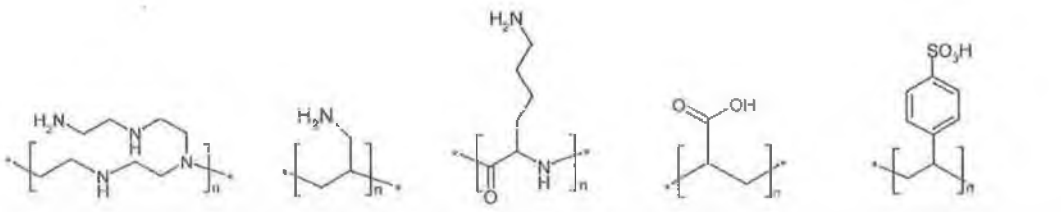

Figure 5.6: Chemical structure of different types of poly-electrolytes. PEI,PAH, PLL are positively charged; PSS, PAC are negatively charged at pH=7.

The principle of this technique is based on the properties of polyelectrolytes (PEL), which are water soluble charged polymers. Examples of the chemical

structures of some polyelectrolytes used in the LbL technique are shown in figure 5.6. Depending on their chemical structure, the polyelectrolytes can be either positively or negatively charged at a given pH. The essential technique is based on self-assembly processes of polymers involving electrostatic interactions. The schematic depicting the steps in the LbL technique is shown in figure 5.7. Prior to deposition, a substrate is charged followed by immersion of the substrate in a suitable solution of poly-electrolyte with an opposite charge to the charge on the substrate (a). The strong electrostatic interaction between the substrate and the polymer causes the deposition of the polymer layer of nm thickness on the substrate . This process leads to change of the charge on the surface avoiding further deposition of the polymer (b). Next, the substrate is repeatedly rinsed with deionised water and immersed in a polymer solution of an opposite charge (c). This again leads to the deposition of a polymer layer of given thickness and the change of the charge on the substrate (d). These steps can be repeated to build poly-electrolyte layers of desired thickness. Several parameters, such as the pH of the solution, salt concentration in the solution and type of PEL significantly influence the properties of the layers, such as the thickness of the layers [16, 17] and porosity [18].

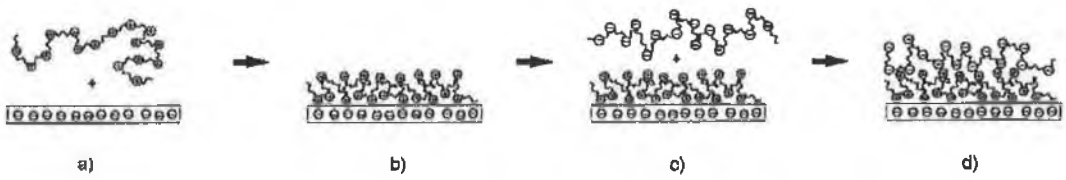

Figure 5.7: Schematics of deposition PEL layers (explanation in text).

Apart from using the LbL technique for deposition of a layer with a well defined thickness, the LbL technique can also be used for immobilisation of fluorescent dyes onto surfaces [12]. In this method, the desired dye is conjugated with one of the PEL and the above process for the deposition of PEL layers is applied. In our experiments, Ru dye complexes were conjugated with the positively charged polymer Poly(Alylamine)(colloquially known as PAH).

5.2.2 Experimental procedures

LbL procedure

Glass substrates were cleaned by immersion in Piranha solution (3 : 1 H_2SO_4 : 27%H_2O_2). The solution was heated at 60 °C for 1 hour. Afterwards slides were rinsed with deionised water. Solutions of PEI, PSS and PAH were prepared at 2mg mL^{-1} in 0.5 M NaCl aqueous solution and dissolved by sonication at room temperature for 25 minutes. The cleaned glass substrates were then immersed in the solutions of polyelectrolytes with an incubation time of 15 minutes using the following sequence PEI/$[PSS/PAH]_x$, where x is the number of bilayers. The substrates were then rinsed with deionised water between immersions into the PEL solution.

Synthesis of dye conjugated PEL

The ruthenium dye and PEL were conjugated via the facile formation of a thiourea bond between the amine group of the polyelectrolyte, poly(allyamine) hydrochloride and the isothiocyanate group of the ruthenium complex needs reference . Briefly, 4.7 mg of PAH ($5x10^{-5}$ mols of monomer) and 2.1 mg of sodium hydrogen carbonate ($25x10^{-5}$ mols) were dissolved in 0.25 mL of water. Separately 4.9 mg of Ru-ITC ($5x10^{-6}$ mols) was dissolved in 1 mL of DMF. The two solutions were mixed at 4 °C under rapid stirring and aged in the dark for a further 2 hours. Ru-PEL precipitated on the addition of acetone and was separated by filtration. The final concentration of polyelectrolyte was assumed to contain 1 ruthenium complex per ten monomer units. The quantum efficiency of the dye determined against pure tris(2,2'-bipyridyl)dichlororuthenium (II) hexahydrate was calculated at 0.031 and the extinction coefficient determined using absorption spectroscopy was 12335 $M^{-1}cm^{-1}$. The excitation and emission maxima for the Ru-PEL were 464 and 606 nm,respectively, with a Stokes shift of 142nm.

Ellipsometry

The ellipsometric measurements were carried out on a white light ellipsometer (DeltaPsi 2, Jobin Yvon, group Horiba). The data were acquired in reflection mode with angle of incidence of 60^0. The measurements were carried out for

wavelengths in the range from 300nm to 800nm with a 5nm step. The acquisition time for each wavelength was 1s and the data ware averaged over 5 measurements. A program supplied with the ellipsometer was used to fit parameters of the layers (thickness, refractive index) so that the theoretically predicted ellipsometric coefficients Δ, Ψ correspond to the measured coefficients Δ, Ψ.

Absorption spectroscopy

Samples were prepared in the following way: first, on a glass substrate seven preliminary PEI/$[PSS/PAH]_3$ layers were deposited, which generated a uniform positive charge on the substrate. Next, four [PSS/Ru-PAH] bilayers were deposited, and after each bi-layer deposition the absorption spectrum of the sample was taken. Because the sample was immersed in the solution, PEL layers were formed on both sides of the glass substrate, and therefore the absorption spectra were recorded for 2,4,6 and 8 bilayers. Absorption spectra were measured using a UV-VIS spectrometer (Tecan, Inc).

5.2.3 Layer characterisation

PEL layers

Different numbers of polyelectrolyte layers were deposited on glass substrates. The number of the PEL layers was 0,5,10,16. The samples were then placed in the ellipsometer and the ellipsometric parameters Δ, Ψ of each sample were obtained. The acquired data are shown in figure 5.8. The refractive index and the thickness of the layers can be then obtained, if an appropriate model of the layers on the substrate is applied and the theoretical parameters Δ, Ψ are fitted to the data in figure 5.8 [19]. The fitting procedure was as follows: first, from the data for a bare glass slide the refractive index of the glass was obtained. Next, data from the sample with 16 PEL layers were analysed, where the assumed model consisted of (1) a glass substrate (with refractive index obtained from previous measurement) at the base, (2) a PEL layer (of unknown refractive index and thickness), (3) a PEL/void layer (of unknown refractive index and thickness). This third layer represents the roughness of the PEL layers. The dispersion relation for the refractive index of PEL was modelled by an absorbing Cauchy

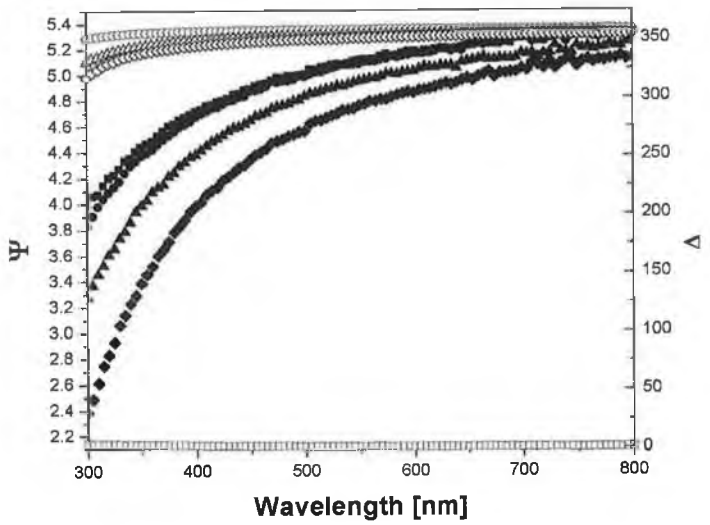

Figure 5.8: Experimental data of Ψ (filled symbols) and Δ (open symbols) for samples: substrate (□), substrate/5PEL (o), substrate/10PEL (△), substrate/16PEL (◇)

function [19]. By fitting the parameters obtained via this model, the refractive index, the thickness and the roughness of PEL layers were obtained. Finally, the same model was applied to the remaining samples (5,10 PEL layers) to obtain the thickness and roughness, where the refractive index of PEL obtained from previous measurements was used. The data are summarised in figure 5.9. The thickness of the layers increase with the number of the deposited PEL layers. Interpolating the data leads to the averaged thickness of one PEL layer equal to 1.5nm. The surface roughness of the samples was around 2nm and slightly increased with increasing number of PEL layers (the roughness is represented by the vertical error bars in figure 5.9). This roughness of the layers was also independently confirmed by AFM measurements. In figure 5.9 (a) the averaged refractive index of the PEL layers is shown.

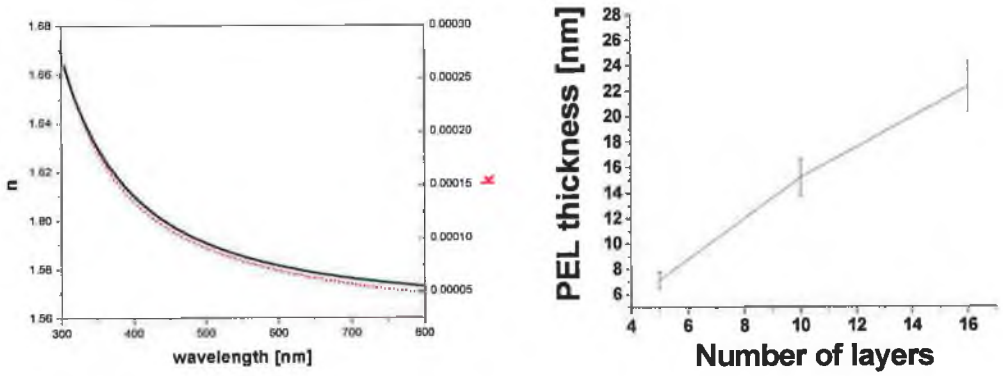

a b

Figure 5.9: (a)Refractive index (n,k) of PEL layers as a function of wavelength obtained from ellipsometer data. (b) Variation in the PEL thickness with number of layers of polyelectrolyte determined from the ellipsometer fit parameters. The error bars relate to the surface roughness used in the ellipsometer model and are not determined from multiple experiments.

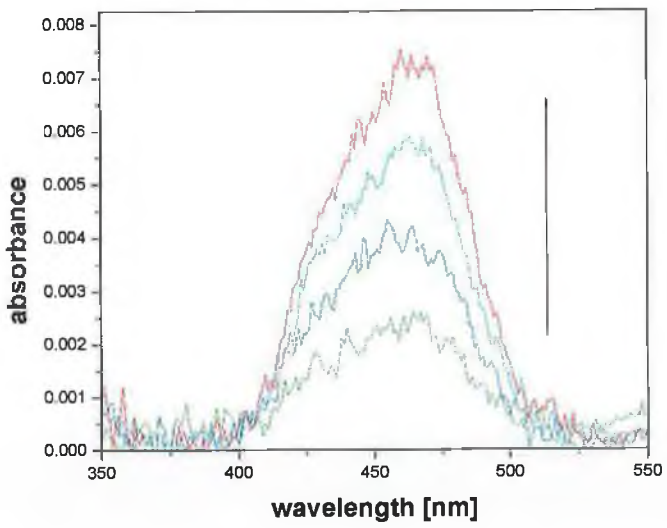

Figure 5.10: Absorption spectra of PEL-dye conjugated layers (glass/PEL7/[Ru-PAH/PSS]$_x$). x increases in the direction of the arrow (x=2,4,6,8)

Dye conjugated PEL

In order to verify the growth of polymer layers with the dye-conjugated PEL, Ru-dye conjugated PEL (Ru-PAH) layers were deposited onto a substrate and the absorbance of the layers was measured. The absorption spectra of Ru-dyes from the samples with different numbers of the [Ru-PAH/PSS] bilayers are given in figure 5.10 (the background signal is substracted). The peaks from 400nm to 500nm wavelengths correspond to the absorption of Ru-complex dye (see figure 4.10) and the data confirms that the absorbance is also increasing with the increasing number of the bilayers. Since the absorbance is linearly increasing with the number of the bilayers, this indicates the successive deposition of identical Ru-dye conjugated PEL layers. From the Beer-lambert law in equation (2.1) the average density of the dye in the Ru-PAH films was estimated to be 50 molecules per 10nm x 10nm surface area.

5.3 Nanoparticle attachment

Several methods have been developed for deposition of metal NPs onto substrates. The most common methods are physisorption of NPs, which are spin-coated [20, 21] or ink-printed [22] onto substrates or the immobilisation of the NPs by applying functional coupling agents (thiol or amine groups) between NPs and a surface [23, 24]. However, PEL layers can also be used for immobilisation of metal NPs onto substrates [25, 15, 26]. The method is based on electrostatic attraction of mostly negatively charged NPs in solution to the oppositely charged PEL layers assembled onto the substrates. The main advantage of this method is that the NPs can be attached to any substrate, where PEL layer deposition is possible. Therefore, this technique allows the deposition of NPs on glass substrates as well as on plastic substrates.

This section describes a series of experiments investigating the attachment of different NPs onto substrates followed by their characterisation with absorption spectroscopy and atomic force microscopy.

5.3.1 Experimental

On a glass substrate five preliminary layers of PEI/$[PSS/PAH]_2$, which generated a uniform positive charge on the surface, were deposited following the procedure described in section 5.2.2. These substrates were than immersed in a colloidal NP solution for 12 hours. The colloidal solutions consisted of either 60nm silver spherical NPs or triangular shaped NPs with average size of 99nm (see section 5.2.2 for the NP description). Prior to the immersion of the slides, the colloids were centrifuged and re-dispersed in deionised water in order to remove unattached protective groups from the solution, which would otherwise decrease the NP attachment due to their charge. This additional process also allowed the increase of the concentration of the NPs. After incubation with the colloids, the slides were rinsed with deionised water and dried with N_2.

Absorption measurements were carried out with a UV-VIS spectrometer (Tecan, Inc). AFM images were collected on a Dimensions 3100 AFM (Digital instruments Ltd) in tapping mode using silicon tips purchased from Veeco Instruments. Samples were scanned under ambient conditions. The images were processed using

the WSxM 4.0 (Nanotec Electronica S.L.) software.

5.3.2 Characterisation of the NP attachment

Metal NPs were successfully attached onto the glass substrates, where the colloid solution was either 60nm silver spherical NPs or silver triangular shaped NPs with a size of 99nm. These NPs were characterised as reported in the previous section and their absorption spectra are shown in figure 5.1 and figure 5.4 for spherical and triangular NPs, respectively. The change in the color of the samples due to the LSPR of the NP was visible by the naked eye and was uniform over all of the samples.

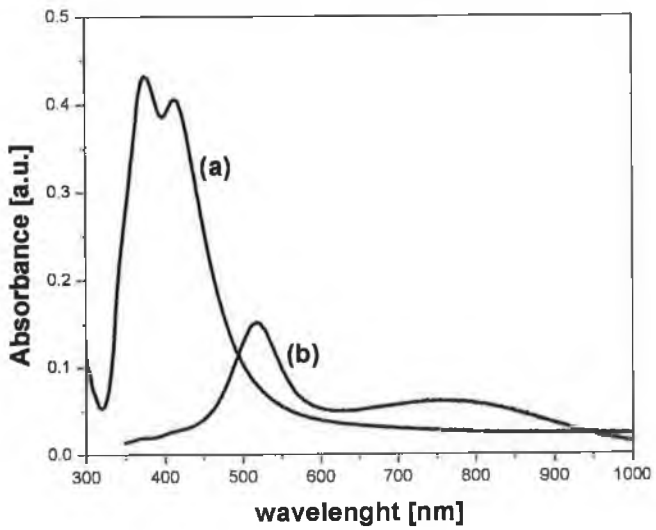

Figure 5.11: Absorption spectra of glass slides with poly-electrolyte layers and silver spherical (curve a) or silver triangular (illumination 550nm) (curve b).

These samples were further characterised by absorption spectroscopy. The absorption spectra of the glass slides with the NPs are shown in figure 5.11. The spectra exhibit distinct peaks corresponding to the localised surface plasmon resonance of metal NPs, but the peaks differ from that obtained in solution (figures 5.1 and 5.4).

In the case of 60nm spherical NPs, the plasmon peak shifted from 442nm to

415nm and the absorption spectra exhibits another peak at 374nm. The shift can be explained by the change of the refractive index of the medium surrounding the NPs. If the NPs are in a solution, the refractive index of the embedded medium is equal to the refractive index of the solution (in the case of water n=1.33). If the NPs are attached to a substrate with refractive index $n_{substrate}$ and the substrate is in a medium with refractive index n_{medium} then it can be approximated that the NPs are in a medium with the effective refractive index n_{eff}, which is a combination of $n_{substrate}$ and n_{medium} [27, 28, 29]. Using a simple model the effective refractive index can be described as [30]

$$n_{eff} = \alpha n_{substrate} + (1 - \alpha) n_{medium} \tag{5.1}$$

where α is the appropriate weighting factor, lying in the range from 0 to 1. In our case, the n_{eff} was obtained by fitting theoretically computed absorption spectra to measured absorption spectra of the NPs. The effective refractive index of the 60nm silver NPs attached to the glass substrate was estimated to be n_{eff}= 1.27. The origin of the second peak at 374nm is less obvious. It is thought that the second peak is due to the quadrupole resonance in the metal NPs. The position of this peak corresponds well with the model for a 60nm silver spherical when the effective refractive index equal 1.27 is used. The discrepancy lies in the intensity of the peak. In the theoretical model the peak is barely visible, whereas in the experiment the peak is larger than the dipole peak. This increase of the quadrupole resonance could be attributed to the coherent interaction between large NPs in two-dimensional array [31].

In the case of triangular NPs, the dipole plasmon peak in the absorption spectrum in figure 5.11 (curve b) is shifted from 548nm to 517nm. This can be again explained by the change of the effective refractive index n_{eff}. A second small broad absorption peak around 761nm probably originates from small amount of the larger triangles attached onto the substrate.

The topology of the samples was assessed by atomic force microscopy. The images of the sample with 60nm silver spherical NPs are shown in figure 5.12 (a,b). The AFM images confirmed the homogenous distribution of the NPs on the substrates. The vertical resolution of the AFM images was quite accurate giving the height of the NPs to be around the expected value of 60nm, whereas the horizontal resolution of the NPs in the AFM images was influenced by the

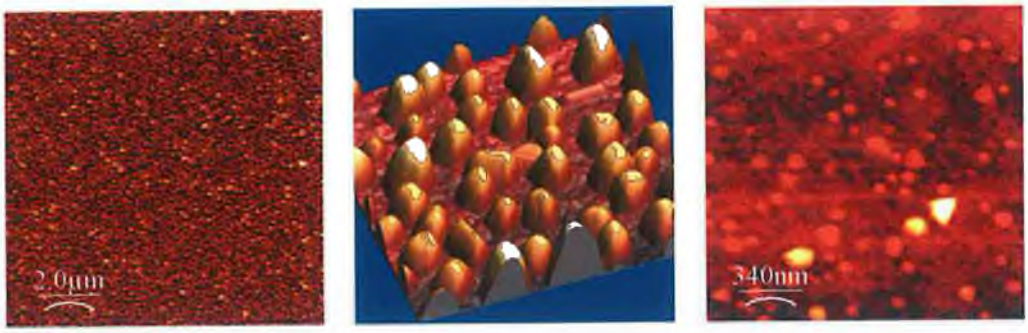

a b c

Figure 5.12: AFM images of glass slides with NPs. (a) A glass slide covered with 60nm silver spherical NPs. (b) 3D view on a smaller section of the image (a). (c) A glass slide covered with silver triangular shaped NPs with the size of 99nm.

finite width of the AFM tip. Therefore, the NPs seemed larger and longer in the dragging direction of the AFM tip than they really were. The average surface density of the NPs was estimated to be 65 particles per 1 μm^2. The average surface coverage of 12% was estimated by assuming the average NP radius to be 30nm. This gave the average space between two particles of about the size of the particles themselves. This coverage is close to the maximal achievable via this technique. The NPs can not be packed more closely due to the negative charge on the NPs causing repulsion of the NPs on the substrate. The image of a sample with attached silver triangular NPs with a 99nm size is shown in figure 5.12 (c). The height of the triangular NPs was around 12nm. From the AFM images the surface density of the triangular NPs was estimated to be 30 particles per 1 μm^2.

5.4 LSPR from nanostructured substrates

In this section, the experiments were focused on reproducible deposition of different NPs onto plastic substrates, and reproducible deposition of polyelectrolytes over the attached NPs. Plastic microtiter plates made from polystyrene were chosen as a suitable substrate for these experiments investigating NP attachment, since multiple experiments could be carried out only small volumes of solution were required. The reproducibility of the deposited layers was determined by measuring the localised surface plasmon resonance over large number of samples. While the LSPR is very sensitive to the refractive index surrounding the NPs (see section 2.3.2), the dependence of the LSPR on the number of deposited PEL layers over the NPs was also measured. A schematic illustrating the different structures prepared in the microtiter plate is shown in figure 5.13.

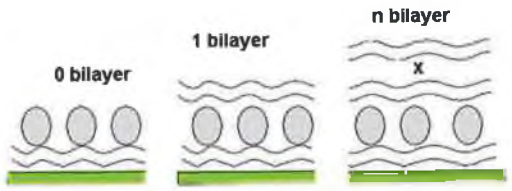

Figure 5.13: Schematic of NPs structured layers in microtiter plate.

5.4.1 Experimental

Nanoparticles synthesis

Spherical gold and gold/silver NPs were prepared using the method described in section 4.1.2. The silver spherical NPs were prepared using the method described in section 5.1.1.

Microtiter plates preparation

Microtiter plates (obtained from Greiner bio-one International) had a polystyrene coated surface. To activate each well for deposition of polyelectrolyte the plate was plasma-treated for five minutes under vacuum using a Harrick, model PDC-200, plasma chamber. In the first instance, five preliminary layers of polyelec-

trolyte were deposited onto each well to generate a uniform surface of amine groups for attachment of NPs. Five layers is the minimum amount of preliminary layers required; any less leads to a surface with incomplete polyelectrolyte coverage and ambiguous charge. Solutions of PEI, PSS and PAH were prepared at 2mg mL^{-1} in 0.5 M NaCl aqueous solution and dissolved by sonication at room temperature for 25 minutes. Polyelectrolyte solutions were deposited into each well at volumes of 150 μL with incubation times of 15 minutes using the following sequence PEI/PSS/PAH/PSS/PAH. The wells were rinsed with deionised water between the addition of each PEL layer.

Each NP solution was deposited into 16 wells of the microtiter plate at well volumes of 150 μL. The plate was sealed with parafilm to stop evaporation and incubated for 12 hours. The top two rows of wells were coated with gold / silver alloy NPs, the middle two rows with pure gold NPs and the bottom two rows with silver NPs. After rinsing, absorbance measurements were performed under dry conditions and with 150 μL of water added. Each set of 16 wells was further divided into sets of 4 wells and a series of (PAH/PSS)x spacer bilayers deposited using the same procedure as that for the deposition of the preliminary layer, where x = 0, 1, 4 and 8 bilayers.

Absorbance measurements

The absorption spectra of the microtiter plate were taken using microtiter plate reader Cary 50 scan UV-Visible spectrophotometer (Varian Ltd) in transmission mode.

5.4.2 Results

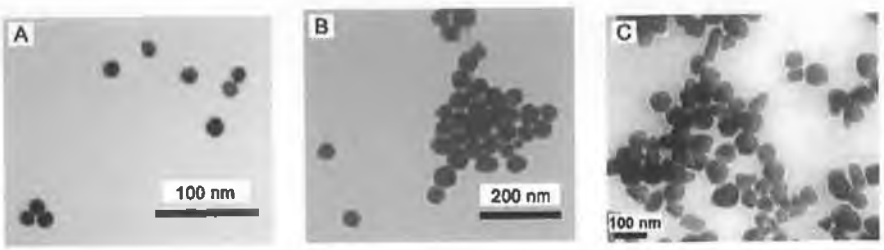

Figure 5.14: Transmission electron micrographs of gold (A, 15 nm +/- 1), gold/silver alloy (B, 47 nm +/- 5) and silver (C, 60 nm +/- 11) nanoparticles.

Gold, gold/silver and silver NPs were successfully prepared. The samples were analysed by transmission electron microscopy and the average size of gold, gold/silver and silver NPs was 15 ± 1nm, 47 ± 5nm, 60 ± 11nm, respectively. The SEM images are shown in figure 5.14.

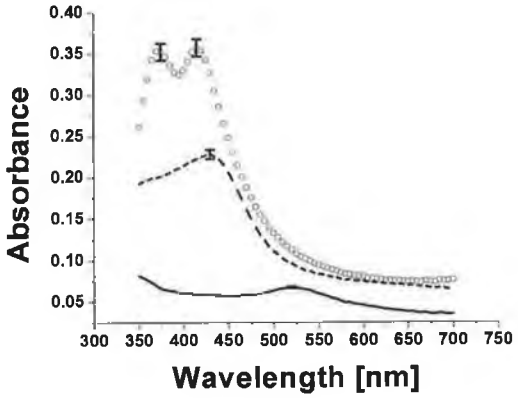

Figure 5.15: UV-Vis absorbance of pure silver NPs, (o), gold/ silver alloy NPs, (dashes) and pure gold NPs (solid line) coated onto polyelectrolyte activated microplate wells analysed at room temperature in air. Forty eight wells were examined in total, sixteen for each NP type.

These particles were then attached onto the microtiter plate, where each set of NPs was attached onto 16 wells. Each set of 16 wells coated with one type of NPs exhibited a specific color, which was uniform over the wells. The absorption spectra of the dried plate were recorded and the results are shown in figure 5.15. The three spectra represent the average absorption from 16 wells for each type of NP and the error bars indicates the standard deviation at the peak's maximum. The silver NPs exhibit a double peak at 375 and 415 nm, where the peak at 415nm ($A_{375} = 0.351$) is due to the LSPR of single NPs and the peak at 375nm is thought to be due to the coherent interaction between large NPs in two-dimensional array as discussed in the previous section 5.3.2. The attached gold/silver NPs and gold NPs exhibit a single absorption at 430nm ($A_{430} = 0.228$) and 520nm ($A_{520} = 0.067$), respectively. In all three cases the reproducibility from well to well was very good and the variation of the absorption spectra was less than 3%. The difference in the maxima of the absorption peaks is given by the NPs' surface coverage and by the value of the normalised extinction cross section ($C_{ext}/\pi r^2$),

which was biggest for the 60nm silver NP, lower for the 47nm gold/silver NPs and smallest for the 15nm gold NPs.

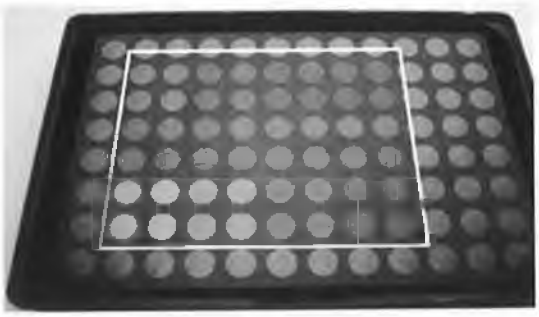

Figure 5.16: Photograph of an upturned microplate coated with three different NP overlayed with PEL layer. The polyelectrolyte layer thickness increases from right to left with two columns per a given PEL thickness(0, 3, 12 and 24 nm).

Next, layers of PEL were attached over the NPs in the microtiter plate. Two, four and eight bilayers of PEL were deposited in four wells for each set of NPs. The image of such a dried plate is shown in figure 5.16. The top two rows of wells are coated with gold / silver alloy NPs, the middle two rows with pure gold NPs and the bottom two rows with silver NPs. It is clearly seen that the absorption of the NPs in the wells changes, which confirmed the PEL layers attachment onto the NPs. The color was again quite homogenous over the whole surface of the wells. The absorption spectra of these wells were measured. The evolution of the absorption spectra of the 60nm silver NPs with the number of the PEL layers is shown in figure 5.17. The average absorption spectra for each set of PEL layer is plotted and the bars represents the standard deviation at the maximum of the LSPR peak. From the graphs it follows that the LSPR peak shifts to longer wavelength and the absorbance increases. This is due to the high sensitivity of the LSPR peak to the change of the refractive index of the embedded medium (see section 2.3.2 in theory chapter). The absorption spectra of LSPR of gold/silver and gold NPs due to the presence of the PEL layers are shown in figure 5.18. Similarly, the LSPR peaks in the absorption spectra shift to longer wavelengths and the absorbance increases.

Next, the absorption spectra of the wells with different NPs and numbers of PEL layers were again measured, but in this case the wells were filled with

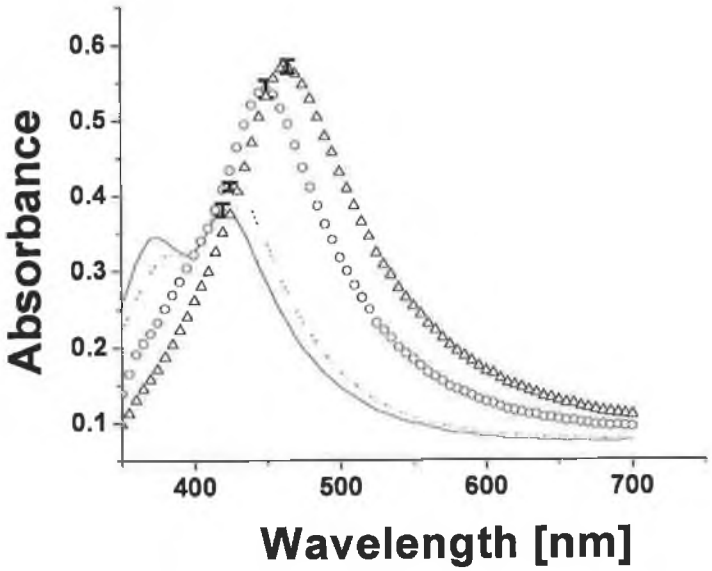

Figure 5.17: UV-Vis absorbance of pure silver NPs coated with additional [PAH/PSS] bilayers analysed at room temperature in air. As the number of bilayers increased (0, solid; 1, dash; 4, o; 8, △) the LSPR band shifted to a longer wavelength and increased in intensity.

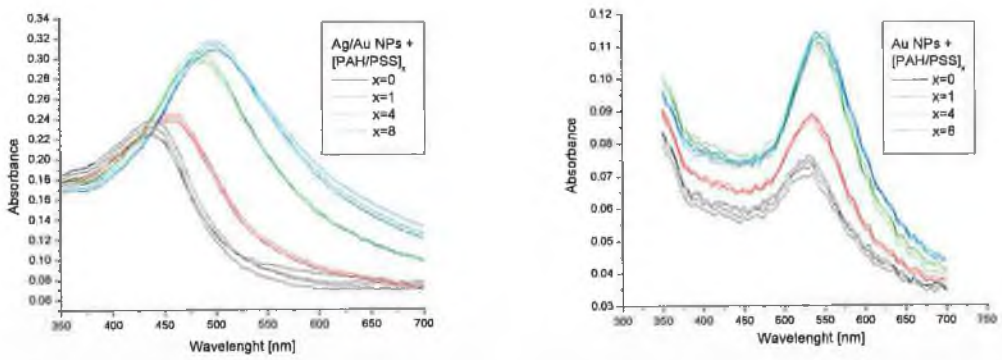

a b

Figure 5.18: UV-vis absorbance of gold silver (a) and gold (b) NPs coated with additional [PAH/PSS] bilayers analysed at room temperature in air. As the number of bilayers increased the LSPR band shifted to a longer wavelength and increased in intensity.

water, which caused a shift of the plasmon resonance. The shift of the LSPR of the NPs is dependent on the thickness of the PEL layers for dried and wet wells as shown in figure 5.19 (a). Because the thickness of PEL films on a plane substrate prepared by the same procedure was 3 nm per bilayer (see section 5.2), the thickness of the PEL layers on the NPs was assumed to be 3nm per bilayer also. From the graphs it follows that LSPR in all three types of NPs shifts to longer wavelengths and the LSPR in water is shifted to the longer wavelengths compared to the same system in air. Further, the largest change of λ_{res} with the increase of the PEL layers (slope in the graph) is for bare NPs and decreases with increasing thickness of the PEL layers. The shift of λ_{res} is also more significant in silver and gold/silver NPs than in gold NPs.

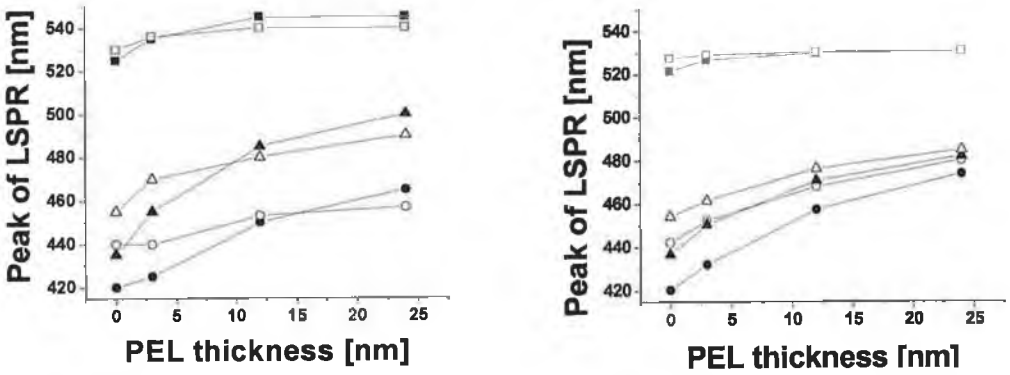

Figure 5.19: Shift of the peak of the LSPR with changing thickness of the polyelectrolyte layer measured using UV-vis absorbance spectroscopy (a). Samples were analysed in air (filled symbols) and under water (open symbols) where gold NPs are □; alloy NPs, △; and silver NPs, o. Theoretical calculated shift is in part (b)

This dependence of the LSPR on the thickness of the PEL layer was also theoretically calculated using the theory described is section 2.3.2. The PEL layers were modelled as a shell around the NPs with thickness corresponding the thickness of the PEL layer and with refractive index of PEL n≐1.6 obtained in the previous characterisation (see section 5.2). The effect of the the substrate on the LSPR was modelled by the effective refractive index n_{eff} (see section 5.3.2), where the value of n_{eff} was chosen in such a way that absorption spectra of NPs without PEL overlayers fit to the theoretical spectra. The resulting theoretical

dependence of the LSPR of different NPs in air and in the water on the thickness of the PEL layer is shown in figure 5.19, (b). The theoretical spectra qualitatively agree with that measured experimentally, showing the shift of LSPR to longer wavelengths with increasing thickness of the PEL; the largest shift of LSPR is for the first PEL layers and this shift is larger for the silver and gold/silver NPs than for gold NPs. The discrepancy between the theoretical and experimental spectra is that the curves for the same NP in air and in water does not cross in the theory but they do in the experiments. This could be explained by the lower refractive index of PEL in water than in air (the refractive index of PEL was measured only on air (see section 5.2)) which was not taken into account.

Experiments described in this section demonstrated the high reproducibility of attachment of different NPs onto microtiter plates, and reproducible deposition of the PEL spacer layer on the top of the NPs. The presence of the PEL layer was confirmed by observing a shift of LSPR to the longer wavelength with increasing thickness of the PEL. The shift was more significant for large silver and large gold/silver NPs than for small gold NPs.

5.5 Fluorescence enhancement experiments

In the preceding sections, a suitable method for uniform deposition of different types of nanoparticles and deposition of a fluorescent dye layer at given distance from the nanoparticles was established. Because of the flexibility of this method, different nanoparticle-dye configurations could be prepared and the effect on the fluorescence due to the presence of the nanoparticles could be studied. Several experimental investigations of the effect of the plasmonic enhancement of fluorescence are described in the literature [32, 33, 34, 35, 36, 37, 38, 39, 40]. However, these reported methods lack the flexibility of our methodology that allows the evaluation of the dependence of plasmonic enhancement on various parameters simultaneously. The experiments described here deal with the dependence of the enhanced fluorescence on the nanoparticle-dye separation, on the optical properties of the nanoparticles, on the NPs' size, the surface coverage, and on the type of fluorescent dye.

5.5.1 Dependence of enhanced fluorescence on nanoparticle-dye separation for nanoparticles with different LSPR wavelength

The plasmonically enhanced fluorescence is very sensitive to the dye-nanoparticle distance as explained in section 2.4. Briefly, the fluorescence should be totally quenched for a very small dye nanoparticle separation (less then few nanometers). If the dye is placed beyond this quenching zone the fluorescence enhancement should reach a maximum and then decrease with increasing separation. Based on the deposition technique developed and described in previous sections, the following experiment deals with distance dependence of enhanced fluorescence for nanoparticles with different LSPR wavelengths.

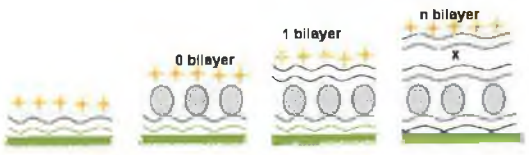

Figure 5.20: Schematic of layers in a well.

In these experiments the microtiter plate prepared in section 5.4 was used. The plate consists of wells covered with three different type of nanoparticles and covered with spacer layers of four different thicknesses (see figure 5.16). Additionally, Ru-complex conjugated polyelectrolyte was deposited over the spacer layers and this was followed by a measurement of the fluorescence signal from the wells. The schematic of the wells is shown in figure 5.20.

Experimental

Ru-dye conjugated PEL layers (characterised in section 5.2.3) were attached to the bottom of the wells of the mircotiter plate prepared and characterised in section 5.4 using the following procedure: Ru-PEL solution was deposited into each well at volumes of 150 μL with a concentration of 2.8x10^{-5} M of ruthenium complex and 0.5 M NaCl. The Ru-PEL solution was left to react for 15 minutes and then each well was rinsed thoroughly with deionised water. In the wells where no spacer layer was present, prior to the deposition of a positively charged Ru-PEL, a solution of PSS (negatively charged PEL) was applied in order to obtain a negative charge on the surface between the NPs.

Instrumentation

Fluorescence measurements were performed on a Safire (Tecan) microplate reader. The emission wavelength was set to match the maximum emission of the Ru-PEL at 620 nm. The excitation wavelength was varied from 350nm to 550 nm to cover both the LSPR of the NPs and the absorption band of the dye. Self quenching of the dye was not expected because of the large Stokes shift.

Fluorescence images were taken using a standard Olympus Upright Microscope with an excitation filter in the range from 470nm to 490nm and barrier filter at 515nm. The images were recorded through the transparent bottom of the wells.

Results

A layer of Ru-dye doped PEL was attached to the wells covered by three different types of nanoparticles (60nm silver nanoparticles, 47nm gold/silver alloy nanoparticles, 13nm gold nanoparticles) and different thickness of spacer layers

(0,3,12,24nm). Due to the low concentration of the dye, the presence of the Ru-dye layer could not be directly detected by absorption spectroscopy, but the presence of the additional PEL layer was indicated by the shift of LSPR of the nanoparticles (data not presented).

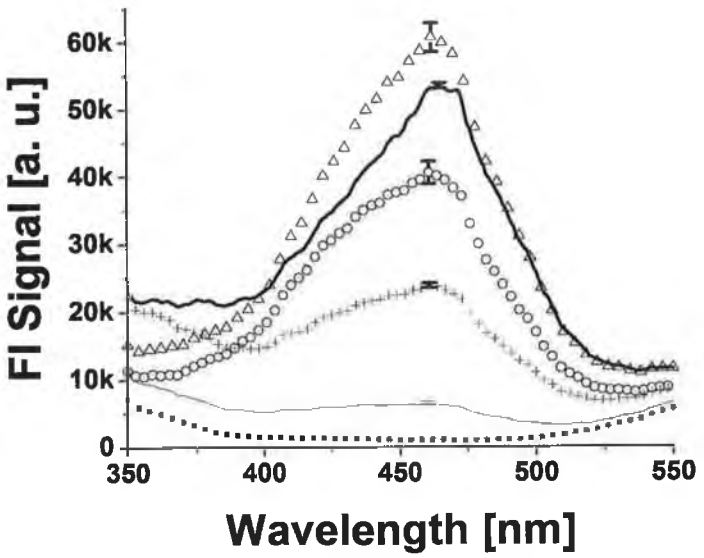

Figure 5.21: Excitation fluorescence spectra of a layer of fluorescent dye, Ru-PEL deposited over pure silver NPs with polyelectrolyte bilayers [PAH/PSS] placed between dye and NPs (monitored at 620nm). Symbols: PEL only (dashed line); pure Ru-PEL (solid thin line); 0 bilayer (o); 1 bilayers (△); 4 bilayers (solid thick red line); 8 bilayers (+)

The fluorescence excitation spectra from different wells were recorded. Comparison of the excitation spectra from a Ru-doped layer and Ru-doped layer attached to 60nm silver nanoparticles with different spacer layers is shown in figure 5.21. Each excitation curve is an average over four samples. It follows from the figure that the fluorescence signal is substantially higher when the 60nm silver nanoparticles are present. Moreover, the fluorescence signal significantly depends on the thickness of the spacer layer. Next, the excitation spectra of the Ru-doped layers were recorded from the wells with gold/silver NPs. The plasmonic effect of the enhanced fluorescence and its dependence on the thickness of the spacer layer was also observed in this case, but the maximum enhancement was lower

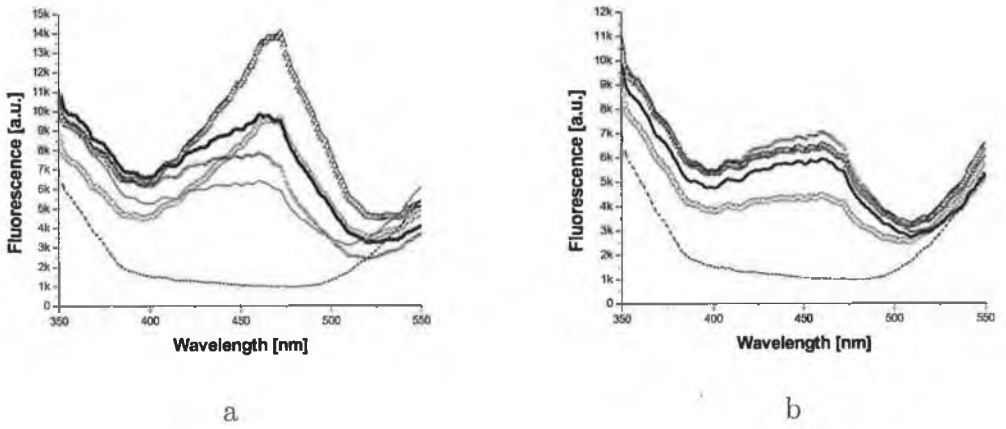

Figure 5.22: Excitation fluorescence spectra of a layer of fluorescent dye, Ru-PEL deposited over silver gold (a) and gold (b) NPs with polyelectrolyte bilayers [PAH/PSS] placed between dye and NPs to regulate the distance. Symbols: PEL only (dashed line); pure Ru-PEL (solid thin red line); 0 bilayer (o); 1 bilayers (△); 4 bilayers (solid thick line); 8 bilayers (+)

(see figure 5.22, part a). In the case of the gold nanoparticles, the signal from the excitation spectra of Ru-doped layers was decreased in the presence of the nanoparticles (see figure 5.22, part b).

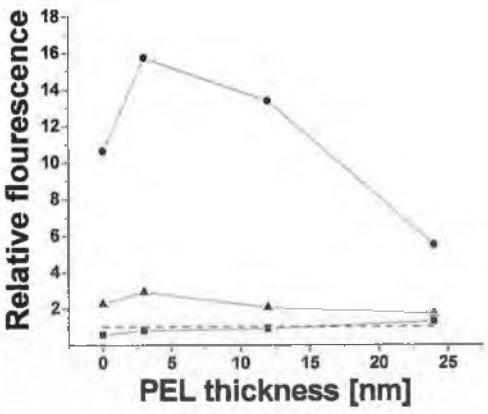

Figure 5.23: Relative enhancement of fluorescence of Ru-PEL coated over silver (•), alloy (■) and gold (▲) NPs with polyelectrolyte bilayers [PAH/PSS] placed between dye and NPs to regulate the degree of overlap of electric field (the dashed line is an enhancement factor of 1).

The results of these measurements were analysed and the enhancement effect, calculated as the ratio between the maximum fluorescence signal with and without nanoparticles, as a function of the thickness of the spacer layer is plotted in figure 5.23. It can be seen that the maxima of the enhancement for silver and gold/silver nanoparticles results for a 3nm thick spacer layer, and with increasing thickness, the enhancement decreases. In the case of the zero spacer layer, the fluorescence is still enhanced but it is lower than is the case for 3nm thickness. On the other hand, the gold NPs behave quite differently. In the case of zero spacer layer, the fluorescence is decreased and when the spacer layer is present, the fluorescence signal is unchanged.

It is important to mention that the thickness of the spacer layer does not directly represent the NP-dye separation but rather the minimum distance between the NP and the dye. This is caused by the fact that only a portion of the dye-doped PEL layer lies upon the NPs, whereas the rest is deposited between the NPs. For example, the results in section 5.3 indicate that the 60nm silver nanoparticles have approximately 10% surface coverage and the inter particle distance is around 60nm. Therefore, only about 10% of dye molecules are at a distance from the NPs equal to the thickness of the spacer layer and the rest of the molecules are at a distance in the range from the thickness of the spacer layer to about 30nm (half distance between NPs).

Therefore, by considering the above, the experimental results are in quite good agreement with the general theoretical conclusions (section 2.4) and can be explained in the following way: when the 60nm silver and 47nm gold/silver nanoparticles have the LSPR overlapping with the absorption spectrum of the Ru-dye complex (compare figures 5.17, 5.18 with figure 5.10) and optimum size (see section 2.4.1), the fluorescence signal is increased. In the case of no spacer layer, the dye molecules attached directly on the nanoparticles are quenched, whereas the fluorescence from the dye in between the nanoparticles is enhanced. In the case of a 3nm spacer layer, there is an additional contribution of the fluorescence signal from the dye placed on the nanoparticles, as they are no longer quenched. With the increasing thickness of the spacer layer, the average NP-dye distance is increasing and therefore the enhancement decreases. The difference in the absolute value of the enhancement for silver (enhancement $\simeq$ 16) and gold/silver (enhancement $\simeq$ 3) nanoparticles could be due to the better optical properties of

silver (see section 2.3.1) and different size of the nanoparticles.

The 15nm gold nanoparticles, in comparison, do not have the LSPR overlapping with the absorption spectrum of the Ru-dye complex. Additionally, the enhanced electromagnetic field is very confined (few nanometers) around the nanoparticles due to their small size. Therefore, if there is no spacer layer, the Ru-dye molecules which are in contact with NPs are quenched and so the fluorescence signal is decreased. In the presence of even the thinnest spacer layer (3nm) the dyes are too far away from the local field generated by the NPs and so the fluorescence signal is almost unchanged.

a b c

Figure 5.24: Fluorescence microscope images of wells with Ru-dye complex and silver nanoparticles with different separation between them: a - pure dye, b - NP/PEL2/dye, c - NP/PEL16/dye. The images, showing a section of the well, were taken from bottom of the microplate and the arc represents the edge of well.

As an independent verification of the fluorescence enhancement, images of the bottom of the wells using a wide field fluorescence microscope were taken. An example of the wells with a Ru-dye doped layer, 60nm silver NPs / 3nm spacer layer / Ru-dye doped layer, and 60nm silver NPs / 24nm spacer layer / Ru-dye doped layer are presented in figure 5.24. The red curved area represents a part of the bottom of the well. It can be seen that the fluorescence signal is quite uniform over the surface of the wells and relative intensities correspond to the previous measurement.

5.5.2 Dependence of the enhanced fluorescence on nanoparticle LSPR wavelength

The previous experiment showed the distance dependence of plasmonic enhancement on NP-dye separation for three different NPs. In the subsequent experiment the emphasis was given to the dependence of the plasmonic enhancement on the NP type. Six different types of nanoparticles were used. They exhibited different spectral position of LSPR, caused by different shapes of nanoparticles (sphere, triangles), their size, or composition.

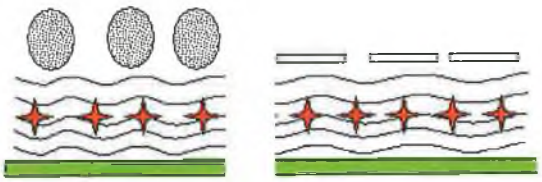

Figure 5.25: Schematic of layers in a well.

As opposed to the preceding experiment, an inverse configuration of the set-up was used (see schematic in figure 5.25). First, dye-doped PEL layers were attached to the surface of the wells. Then a PEL spacer layer was attached. The thickness of the layer was set to 3nm (one bilayer), which was the optimal distance for plasmonic enhancement obtained from previous experiments (see graph 5.23). Finally, different type of NPs were attached to the spacer layer. The advantage of this configuration is that it assured the same amount of fluorescent dye in each well avoiding the ambiguity of the number of dye molecules attached to the plain wells and the NP-modified wells. This ambiguity is associated with the slight increase surface area of the NP-modified wells.

Experimental

Synthesis of the 15nm spherical gold, 60nm spherical silver and 10nm spherical silver, 20nm, 99nm and 163nm triangular-shaped NP is described in detail in sections 4.1.2, 5.1.1 5.1.2 respectively. A method similar to that described in section 5.4.1 was used to attach PEL layers and NPs on the bottom of the microtiter plate wells. Briefly, 6 preliminary PEL layer (PEI/$[PSS/PAH]_2$/PSS) were attached to the bottom of the wells leaving the surface negatively charged.

Next, a Ru-PEL layer was attached to the bottom of 24 wells followed by deposition of a [PSS/PAH] layer. The uniformity of fluorescence signal from Ru-PEL layers was measured. Finally, each type of nanoparticle was attached to bottom of 4 wells. After drying of the sample, the fluorescence and absorption spectra of the microtiter plate were taken using a microtiter plate reader Safire (Tecan).

Results

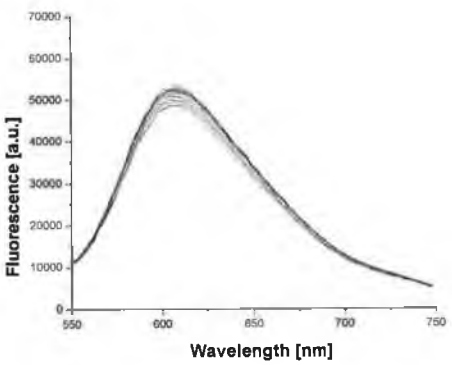

Figure 5.26: Fluorescence from Ru-dye conjugated PEL layers in 24 wells.

The fluorescence emission spectra from 24 wells covered with Ru-PEL layer and 3nm PEL spacer layer are presented in figure 5.26. The graph show that the variation of the fluorescence signal from well to well is low (around 5%). After this, 15nm diameter spherical gold, 60nm spherical silver ,10nm spherical silver, 20nm, 99nm and 163nm triangular-shaped NPs were attached to the these wells (each type of NPs into two wells). After the attachment the absorption spectrum of each well was measured in air. The results are shown in figure 5.27. The absorption of Ru-dye dye in Ru-PEL layer is in the range from around 400nm to 500nm (see figure 5.10). Comparing the spectra from these two graphs indicates that there are two groups of NPs. In the first group are 10nm spherical silver NPs, 60nm spherical silver NPs, 20nm and 99nm triangular-shaped NPs, which have LSPR overlapping with the absorption band of Ru-dye. In the second group are 15nm spherical gold NPs and 163nm triangular-shaped NPs, which have a mismatch of LSPR with the absorption band of Ru-dye. From the conclusion

in the theory chapter (section 2.4.1) it follows that one condition for enhanced fluorescence excitation is the overlap of the LSPR the with absorption spectra of the dye. Therefore, the first group would be expected to exhibit the enhanced excitation fluorescence.

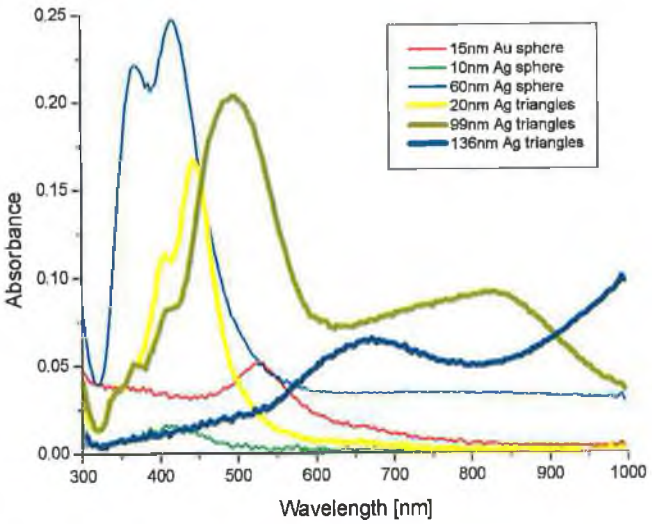

Figure 5.27: Absorption from wells with different types of NPs

The fluorescence excitation spectra from the wells with Ru-PEL and NPs were recorded (the emission wavelength was set to 620nm) and the results are shown in figure 5.28. By comparison of the excitation spectra of pure Ru-PEL layer with Ru-PEL layers with NPs the following can be observed: (1) NPs in the first group (except 10nm silver spherical NPs) give increased fluorescence signal, whereas NPs in the second group give decreased or almost unchanged fluorescence signal. This is in a good agreement with the prediction stated earlier and with the experiments carried out in chapter 3. (2) 10nm silver NPs decrease the fluorescence signal. Due to their small size, the excitation enhancement is minimal and the metal-dye quenching effect is more significant causing the decrease of the fluorescence signal (see section 2.4.1). These results also correspond with the measurement of size dependence of fluorescence on NP size described in chapter 4. (3) The lineshape profile of the excitation spectra of the Ru-dye is changed. This is clearly seen by comparing the excitation spectra of Ru-dye

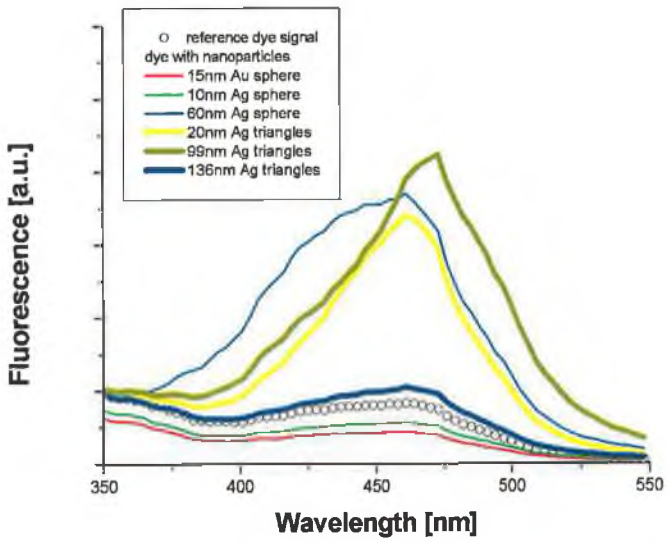

Figure 5.28: Fluorescence excitation spectra from Ru-dye PEL layer coated with different type of nanoparticles. The emission wavelength was 620nm.

with 60nm spherical silver NPs and 99nm triangular shaped triangular NPs. At the wavelengths around the LSPR of the 60nm spherical NPs ($\sim$ 420nm) the enhanced fluorescence is more significant for 60nm spherical NPs, whereas at the wavelengths around the LSPR of the 99nm triangular shaped NPs ($\sim$ 490nm) the fluorescence signal is bigger for the 99nm triangular shaped NPs. (4) The fluorescence signal from Ru-PEL with 163nm triangular-shaped NPs is slightly increased. This could by either emission enhancement (see section 2.4.2) while the LSPR is overlapping with emission band of Ru-dye, or excitation enhancement, because the quadrupole LSPR (see section 2.3.2) is overlapping with the absorption spectrum of Ru-dye.

These quantitative results showed the importance of optimising NP optical properties for plasmonic enhancement of fluorescence.

5.5.3 Dependence of enhanced fluorescence on nanoparticle surface coverage

This next experiment was focused on the relationship between the NP coverage and the enhanced fluorescence signal. As a comparison with the previous experiments, a dye with excitation and emission at longer wavelength was used. Therefore, 163nm silver triangular NPs were used, because they should be optimal for fluorescent enhancement of such dyes.

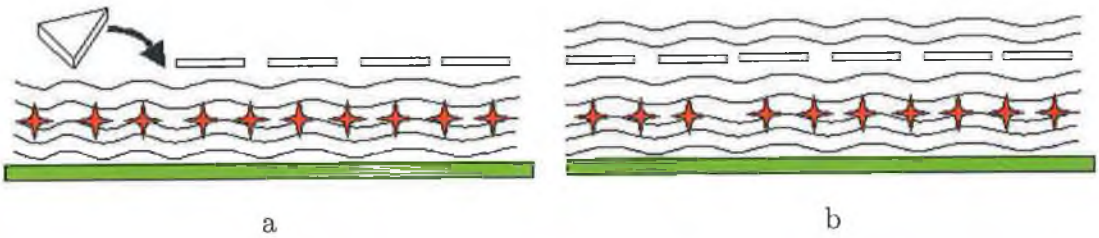

Figure 5.29: Schematic of layers in a well.

The experiment was carried out following the steps presented in figure 5.29. First, dye conjugated PEL layers were attached to the bottom of wells in microtiter plates followed by absorption of a 3nm PEL spacer layer. Next, a solution of NPs was added to the wells. The different NP coverage of substrates in the wells was achieved by different incubation times of the NP solution in the wells. The longer the solution was left in the wells the higher the coverage that was achieved. After removal of the NP solution, an additional PEL layer was attached to the NPs. This additional step improved the LSPR of the NPs. Finally, the emission spectra of the dye with NPs of different coverage were recorded and compared.

Synthesis of Cy5 dye conjugated PEL

The cyanine dye Cy5 and PEL were conjugated via the facile formation of a thiourea bond between the amine group of the polyelectrolyte, poly(allyamine) hydrochloride (PAH) and the isothiocyanate group of the Cy5 dye in a similar manner described in section 5.2.2. The fluorescence properties of the Cy5-PEL were found to be different from free Cy5 dyes. The excitation and emission maxima for free Cy5 are 650nm and 680nm respectively, whereas the excitation

and emission maxima for Cy5-PEL were 670 and 690 nm. Therefore, the quantum efficiency of the Cy5-PEL could not be determined against pure Cy5, but the quantum efficiency was estimated to be very low.

Plate preparation

The method described in section 5.4.1 was used to attach PEL layers and NPs on the bottom of the microtiter plate's wells. Briefly, 6 preliminary PEL layers (PEI/$[PSS/PAH]_2$/PSS) were attached to the bottom of the wells leaving the surface negatively charged. Next, a Cy5-PEL layer was attached to the bottom of 14 wells followed by deposition of a [PSS/PAH] layer. The uniformity of fluorescence signal from Cy5-PEL layers was measured. Next, a solution of 163nm silver triangular NPs was added to the 12 wells. The solution was left in each set of two wells for 1, 2, 3, 4, 5, and 15 hours leading to the different NP surface coverage. Finally, two PEL layers (PAH/PSS) were attached. After drying of the sample, fluorescence and absorption spectra of the microtiter plate were taken using a microtiter plate reader Safire (Tecan).

Results

The emission spectra from wells covered with Cy5-PEL layers are presented in figure 5.30. The excitation wavelength was set at 610nm in order to resolve the whole emission peak. The emission spectra are quite uniform and the variation of the signal from well to well was around 10%. The layers exhibited very low fluorescence signal in comparison to free Cy5 dyes in solution or Ru-PEL layers used in previous experiments. It is believed that the low signal is caused by the very low quantum efficiency of the Cy5 dye conjugated to the PEL. The quantum efficiency of the conjugated dye was decreased probably by self-quenching among the dye [41], because the distance between the dyes conjugated to the PEL was very small and because of the small Stokes shift of the dye.

Next, 163nm triangular silver NPs were attached to a 3nm spacer layer covering the Cy5-PEL fluorescent layers. The NP solution was left in each set of wells for different time periods and then removed, followed by deposition of a 3nm PEL layer. Such prepared wells were first measured by absorption spectroscopy. The spectra are shown in figure 5.31 (part a). The bottom line represents the

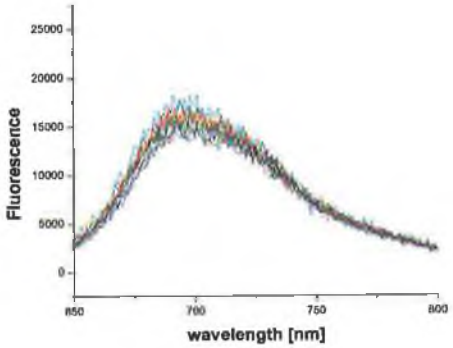

Figure 5.30: Fluorescence from Cy5-PEL layers in 12 wells at 610nm excitation.

absorption of pure Cy5-PEL layer. The other lines represent the absorption from Cy5-PEL layer with the NPs with a different surface coverage (the arrow indicates 1,2,3,4,5,15 hours the solution was in the wells). Each surface coverage was applied in two wells and as can be seen in figure 5.31 (part a) the absorption curves were quite identical. The absorption spectra of attached 163nm silver triangular NPs were broader than the absorption spectra of free NPs in solution (figure 5.4 curve D), but the LSPR was still nicely resolved and overlapping with absorption and emission spectra of the Cy5-PEL layers.

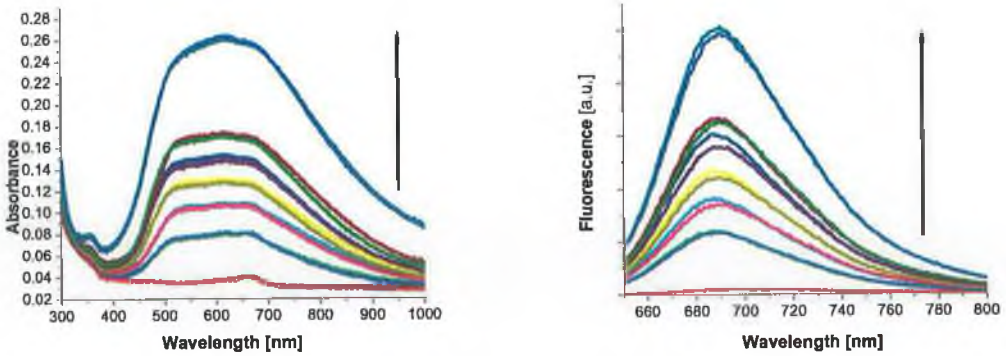

a b

Figure 5.31: Absorption (a) and fluorescence (b) from Cy5 and Cy5 with triangular nanoparticle/PEL2. The arrow indicates increase of the nanoparticle coverage.

The emission spectra of such prepared samples were measured with excitation

wavelength at 610nm. The spectra are seen in figure 5.31 (part b), where again for a given surface coverage there are two curves representing different samples. The bottom lines represent the emission from pure Cy5-PEL layers; the other lines represent the fluorescence from Cy5-PEL layers with the NPs with a different surface coverage (the arrow indicates increasing surface coverage). It is clear from the graph, that the fluorescence of Cy5-PEL layers was significantly increased by the attachment of the 163nm triangular silver NPs and increases with the increasing NP surface coverage. It is thought, that the origin of such significatively increased fluorescence comes from excitation as well as emission enhancement of fluorescence (section 2.4). The excitation enhancement is possible, when the LSPR peak overlaps with the absorption spectra of the Cy5-PEL dye. Because of the small Stokes shift of the Cy5-PEL dye the LSPR peak also overlaps with the emission spectra. Further, the quantum efficiency of the Cy5-PEL dye is estimated to be very low and, therefore, emission enhancement is possible and reaches significantly high values (see section 2.4.2).

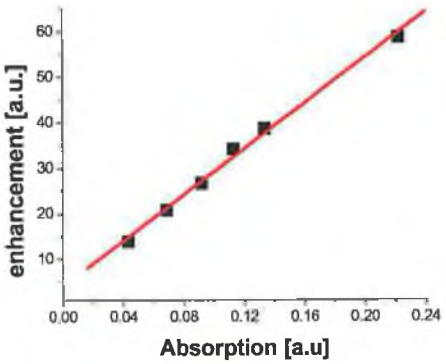

Figure 5.32: The dependence of the enhanced fluorescence from Cy5-PEL on the NPs' surface coverage.

The dependence of the enhanced fluorescence from Cy5-PEL on the NP surface coverage is presented in graph 5.32. The value of the absorbance was measured at 600nm and the enhanced fluorescence was determined as the ratio between the fluorescence signal from Cy5-PEL with NPs and the fluorescence signal from pure CY5-PEL layers at 690nm. The enhanced fluorescence exhibited linear dependence on the NP surface coverage and reaches as high as 60 for the

maximum NP surface coverage. This behavior is expected for low NP surface coverage, where the attached nanoparticles do not interact with each other and the the enhanced fluorescence is proportional to the number of the dyes close to the NPs.

These experiments showed that the enhanced fluorescence is dependent on the NP surface coverage. Therefore, for implementation of the plasmonic enhancement in bio-sensors it is important to achieved reproducible NP surface coverage in order to have a reproducible fluorescence signal. This experiment also suggests a new way of detection of binding kinetics in solutions. In standard fluorescence-based bio-sensors the fluorescence from the bound analyte in solution can not be distinguished from free analyte and therefore, can not be used for a kinetics study. However, use of non-fluorescent metallic NPs with very weak fluorescing layers can be used in a kinetics study of bioreactions, because only the attached NPs will increase the fluorescence signal from the fluorescing layer due to the strong distance dependence of plasmonic enhancement of fluorescence as shown in section 5.5.1, and the unbound NPs will not affect the fluorescence of the attached layers. In order to carry out such measurements the illumination and collection of the fluorescence has to be carried out from below the sample, which was not the case in our experimental set-up, and therefore such an experiment was not carried out.

5.6 Conclusion

This chapter described the development of a method for deposition of various nanostructures on plastic substrates and their usage in plasmon-enhanced fluorescence. In the first section, preparation and characterisation of silver nanoparticles of various shapes was presented. Special focus was given to the process of forming triangular shaped NPs via photo-conversion. This method allowed the production of triangular NPs of various sizes, therefore NPs with different optical properties.

The second section introduced the Layer-by-Layer deposition technique enabling formation of ultrathin polymer layers. The deposited layers were characterised and the method was optimised for deposition of layers on plastic substrates. This method also allowed the formation of thin layers doped with fluorescent dyes. Moreover, these layers proved to be an excellent way for the deposition of NPs on substrates via the electrostatic attraction between the layers and NPs. This method of NP attachment was the subject of the next section, where the protocol for the attachment was optimised and the NP layers were characterised by absorption spectroscopy and atomic force microscopy.

The next part of this chapter showed that, using this method, nanostructured substrates could be applied to commonly used microtiter plates and the reproducibility of such substrates was excellent. Next, the optical properties of these nanostructured layers were studied. Due to the sensitivity of the absorption to the local change of the refractive index, adsorption of single polymer layers over the nanostructured substrates can be detected. This adsorption for various nanoparticles and different thicknesses of the polymer layers was measured and the data compared with the theoretical model.

In the final section, three experiments dealing with plasmonic enhancement of fluorescence were presented. The first one was focused on the dependence of the fluorescence on the NP-dye separation. The results showed that the enhanced fluorescence is highly sensitive to the distance and that the maximum signal is for a 3nm spacer layer. The second experiment was focused on the influence of the fluorescence on the LSPR of the nanoparticles. In agreement with theoretical considerations only NPs with appropriate optical properties enhanced the fluorescence signal. Additionally, it showed the importance of the NPs size on the

fluorescence enhancement. The third experiment investigated the fluorescence enhancement from the dye with excitation and emission in the red region of spectra. The data showed linear dependency of the fluorescence enhancement on the NP coverage.

The method presented herein demonstrated the possibility of the application of a nanostructured surface in order to increase the signal from fluorescence-based biochips. However the experiments showed high sensitivity of the enhancement, and therefore it requires delicate control of the deposition method to achieve reproducible results in plasmonic enhancement in fluorescence-based biochips.

Bibliography

[1] Y. Tan, Y. F. Li, and D. Zhu, "Preparation of silver nanocrystal in presence of aniline," *Journal of colloid and interface science*, vol. 258, pp. 244–251, 2003.

[2] Y. Sun and Y. Xia, "Gold and silver nanoparticles: A class of chromophores with colors tunable in the range from 400 to 750nm," *Analyst*, vol. 128, pp. 686–691, 2003.

[3] R. Jin, Y. C. Cao, E. Hao, G. S. Metraux, G. C. Schatz, and C. A. Mirkin, "Controlling anisotropic nanoparticle growth through plasmon excitation," *Letters to Nature*, vol. 425, no. 2 October, pp. 487–490, 2003.

[4] A. Callegari, D. Tonti, and M. Cherqui, "Photochemically grown silver nanoparticles with wavelength-controlled size and shape," *Nano Letters*, vol. 3, no. 11,NOV, pp. 1565–1568, 2003.

[5] T. Wenzel, J. Bosbach, A. Goldmann, F. Stietz, and F. Trager, "Shaping nanoparticles and their optical spectra with photons," *Applied Physics B*, vol. 69, pp. 513–517, 1999.

[6] K. L. Kelly, E. Coronado, L. L. Zhao, and G. C. Schatz, "The optical properties of metal nanoparticles: The influence of size, shape, and dielectric environment," *Journal of Physical Chemistry B*, vol. 107, no. 3, pp. 668–677, 2003.

[7] X. Shi, M. Shen, and H. Mohwald, "Polyelectrolyte multilayer nanoreactors toward the synthesis of diverse nanostructructured materials," *Progress in polymer science*, vol. 29, pp. 987–1019, 2004.

[8] D. G. Shchukin and G. Sukhorukov, "Nanoparticle synthesis in engineered organic nanoscale reactors," *Advanced Materials*, vol. 16, no. 8, April 19, pp. 671–682, 2004.

[9] M. Schonhoff, "Self-assembled polyelectrolyte multilayers," *Current Opinion in Colloid and Interface Science*, vol. 8, pp. 86–95, 2003.

[10] P. T. Hammond, "Form and function in multilayer assembly: New application at the nanoscale," *Advanced Materials*, vol. 16, no. 15, August 4, pp. 1271–1293, 2004.

[11] P. Bertrand, A. Jonas, A. Laschewsky, and R. Legras, "Ultrathin polymer coating by complexation of polyelectrolytes at interfaces: suitable materials, structure and properties," *Macromolecular Rapid Communications*, vol. 21, pp. 319–348, 2000.

[12] C. Tedeschi, F. Caruso, H. Mohwald, and K. S, "Adsorption and desorption behaviour of an anionic pyrene chromophore in sequentially deposited polyelectrolyte-dye thin films," *J. Am. Chem. Soc.*, vol. 122, pp. 5841–5848, 2000.

[13] M. K. Park, S. Denk, and R. C. Advincula, "ph-sensitive bipolar ion-permselective ultrathin films," *J. Am. Chem. Soc.*, vol. 126, pp. 13723–13731, 2004.

[14] Y. Lvov and G. Sukhorukov, "Assembly of thin films by means of successive depostition of alternate layers of dna and poly(allylamine)," *Macromolecules*, vol. 26, pp. 5396–5399, 1993.

[15] J. J. Kakkasery, J. P. Abid, M. Carrera, and D. J. Fermin, "Electrochemical and optical properties of two dimensional electrostatic assembly of au nanocrystals," *Faraday Discussion*, vol. 125, pp. 157–169, 2004.

[16] M. Salomaki, P. Tervasmaki, S. Areva, and J. Kankare, "The hofmeister anion effect and the growth of polyelectrolyte multilayers," *Langmuir*, vol. 20, pp. 3679–3683, 2004.

[17] J. B. Schlenoff and S. T. Dubas, "Mechanism of polyelectrolyte multilayer growth: Charge overcompensation and distribution," *Macromolecules*, vol. 34, pp. 592–598, 2001.

[18] Q. Li, J. F. Quinn, and F. Caruso, "Nanophorous polymer thin films via polyelectrolyte templating," *Advanced Materials*, vol. 17, pp. 2058–2062, 2005.

[19] H. G. Tompkins and W. A. McGahan, *Spectroscopic ellipsometry and reflectometry: a user's quide.* New York: John Wiley & Sons, Inc., 1999.

[20] Y. K. Hong, H. Kim, G. Lee, W. Kim, J. I. Park, J. Cheon, and J. Y. Koo, "Controlled two-dimensional distribution of nanoparticles by spin-coating method," *Applied Physics Letters*, vol. 80, no. 5, pp. 844–846, 2002.

[21] F. K. Liu, Y. C. Chang, F. H. Ko, T. C. Chu, and B. T. Dai, "Rapid fabrication of high quality self-assembled nanometer gold particles by spin coating method," *Microelectronic Engineering*, vol. 67-8, pp. 702–709, 2003.

[22] H. H. Lee, K. S. Chou, and K. C. Huang, "Inkjet printing of nanosized silver colloids," *Nanotechnology*, vol. 16, pp. 2436–2441, 2005.

[23] T. Okamoto, I. Yamaguchi, and T. Kobayashi, "Local plasmon sensor with gold colloid monolayers deposited upon glass substrates," *Optics Letters*, vol. 25, no. 6, pp. 372–374, 2000.

[24] S. L. Westcott, S. J. Oldenburg, T. R. Lee, and N. J. Halas, "Formation and adsorption of clusters of gold nanoparticles onto functionalized silica nanoparticle surfaces," *Langmuir*, vol. 14, pp. 5396–5401, 1998.

[25] J. Schmitt and G. Decher, "Metal nanoparticle/polymer superlattice films: Fabrication and control of layer structure," *Advanced Materials*, vol. 9, no. 1, pp. 61–65, 1997.

[26] M. Carrera, J. J. Kakkasery, J. P. Abid, and D. J. Fermin, "Modulation of the work function in layer-by-layer assembly of metal nanoparticles and poly-l-lysine on modified au surfaces," *ChemPhysChem*, vol. 5, pp. 571–575, 2004.

[27] A. Hilger, M. Tenfelde, and U. Kreibig, "Silver nanoparticles deposited on dielectric surfaces," *Applied Physics B*, vol. 73, pp. 361–372, 2001.

[28] C. Noguez, "Optical properties of isolated and supported metal nanoparticles," *Optical Materials*, vol. 27, pp. 1204–1211, 2005.

[29] U. Kreibig and M. Vollmer, *Optical properties of Metal Clusters*. Springer Series in Materials Science, Springer-Verlag Berlin Heidelberg, 1995.

[30] A. Curry, G. Nusz, A. Chilkoti, and A. Wax, "Substrate effect on refractive index dependence of plasmon resonance for individual silver nanoparticles observed using darkfield micro-spectroscopy," *Optics express*, vol. 13, no. 7, pp. 2668–2677, 2005.

[31] S. Malynych and G. Chumanov, "Light-induced coherent interactions between silver nanoparticles in two-dimensional arrays," *Journal of american chemical society*, vol. 125, pp. 2896–2898, 2003.

[32] R. F. Aroca, G. J. Kovacs, C. A. Jennigs, R. O. Loutfy, and P. S. Vincett, "Fluorescence enhancement from langmuir-blodgett monolayers on silver island films," *Langmuir*, vol. 4, pp. 518–521, 1988.

[33] G. Chumanov, K. Sokolov, B. W. Gregory, and T. M. Cotton, "Colloidal metal-films as a substrate for surface-enhanced spectroscopy," *Journal of Physical Chemistry*, vol. 99, no. 23, pp. 9466–9471, 1995.

[34] J. Kummerlen, A. Leitner, H. Brunner, F. R. Aussenegg, and A. Wokaun, "Enhanced dye fluorescence over silver island films - analysis of the distance dependence," *Molecular Physics*, vol. 80, no. 5, pp. 1031–1046, 1993.

[35] J. R. Lakowicz, C. D. Geddes, I. Gryczynski, J. Malicka, Z. Gryczynski, K. Aslan, J. Lukomska, E. Matveeva, J. A. Zhang, R. Badugu, and J. Huang, "Advances in surface-enhanced fluorescence," *Journal of Fluorescence*, vol. 14, no. 4, pp. 425–441, 2004.

[36] S. Pan and L. J. Rothberg, "Enhancement of platinum octaethyl porphyrin phosphorescence near nanotextured silver surfaces," *J. Am. Chem. Soc.*, vol. 127, pp. 6087–6094, 2005.

[37] K. Sokolov, G. Chumanov, and T. M. Cotton, "Enhancement of molecular fluorescence near the surface of colloidal metal films," *Analytical Chemistry*, vol. 70, no. 18, pp. 3898–3905, 1998.

[38] D. A. Weitz, S. Garoff, J. I. Gersten, and A. Nitzan, "The enhancement of raman-scattering, resonance raman-scattering, and fluorescence from molecules adsorbed on a rough silver surface," *Journal of Chemical Physics*, vol. 78, no. 9, pp. 5324–5338, 1983.

[39] A. Wokaun, H. P. Lutz, A. P. King, U. P. Wild, and R. R. Ernst, "Energy-transfer in surface enhanced luminescence," *Journal of Chemical Physics*, vol. 79, no. 1, pp. 509–514, 1983.

[40] C. Mayer, N. Stich, T. Schalkhammer, and G. Bauer, "Slide-format proteomic biochip based on surface-enhanced nanocluster-resonance," *Fresenius Journal of Analytical Chemistry*, vol. 371, pp. 238–245, 2001.

[41] J. R. Lakowicz, *Principles of Fluorescence Spectroscopy*. 1999.

Chapter 6

Conclusions

The development of biosensor platforms for the detection and the monitoring of diseases is a very important area of research that can have a dramatic impact on the delivery of health services globally. For these sensors to be successfully adopted, performance criteria such as sensitivity, low cost (preferably disposable) and ease of use have to be addressed. Often these requirements are naturally at odds, such as low cost and high sensitivity. Therefore, new technologies and approaches have to be continually developed and adopted to improve the performance of the sensors.

The aim of the research programme reported in this thesis was to investigate the application a new field of material science to improve the performance of optical biosensors, namely the enhancement of fluorescence-based biosensors using metal nanoparticles. In addition to the theoretical analysis of the fundamental physics, the main focus was to develop techniques for preparation of nanostructured surfaces and their experimental characterisation, which can be readily implemented for the production of biosensors. Furthermore, the aim was to test the prepared nanostructures and to optimise their parameters regarding their ability for enhancing fluorescence signals from fluorescent species in order to improve the fluorescence-based biosensors.

Prior to any experimental work, the plasmonic enhancement of fluorescence was theoretically treated. Initially, the effect of the localised surface plasmon resonance and its dependency on nanoparticle structure was analysed followed by analysis of the enhancement of fluorescence from a fluorescent dye in close proximity to a nanoparticle. The qualitative analysis was restricted principally

to nanoparticles with spherical symmetry, but non-spherical nanoparticles were also considered to some extent. From these theoretical results, some guidelines and restrictions for use of nanoparticles for fluorescence enhancement were established.

Following the theoretical analysis, experimental work with plasmonic enhancement of fluorescence was carried out to verify the analysis. Several techniques for the deposition of metal nanostructures were investigated and evaluated for their simplicity, precision and incorporation in biosensors. Firstly, thermal evaporation techniques were considered. The Nanosphere lithography (NSL) technique was found to be excellent technique for the preparation of periodical identical nanostructures on surfaces due to its excellent control of the size of nanostructures and simultaneously its low cost in comparison with other techniques with similar precision. Additionally, substrates prepared by this technique were examined for their ability to enhance fluorescence signals. Because of the ability of this technique to precisely control the geometrical properties of the nanostructures, the dependence of the fluorescence enhancement on properties of nanoparticle localised surface plasmon resonance was measured, showing the necessity of tuning the localised plasmon resonance in order to optimise the fluorescence enhancement effect. These nanostructures prepared via NSL enhanced the fluorescence signal about 8 times from Cy5 dye molecules.

In the next section, wet chemical approaches for the formation of colloidal particles were investigated. This method of preparation of nanoparticles had the advantage of preparation of large volumes with a reasonably high degree of control of the sizes and composition of nanoparticles. The geometrical and optical properties of the nanoparticles were characterised and compared with theoretical predictions. This was followed by an experimental study of the fluorescence enhancement effect of these nanoparticles in solution with fluorescent dyes attached to them, especially with respect to their optimal size. In agreement with the theoretical models for this system the nanoparticles giving the biggest fluorescent enhancement were about 27nm in radius.

In addition to formation of spherical colloidal nanoparticles, a process for the fabrication of triangular shaped nanoparticles via a photo-conversion method was established. This technique allowed the production of colloidal triangular shaped nanoparticles of various sizes, resulting in nanoparticles with different optical

properties.

The most promising approach for the production of nanostructured substrates investigated in the scope of this thesis was shown to be deposition of colloidal nanoparticles on substrates. This technique had the advantages of a colloidal chemistry approach by forming nanoparticles with desirable optical properties and the advantages of the nanoparticle adsorption technique allowing deposition of the nanoparticles on various substrates with controllable nanoparticle density. The nanoparticles were attached to various substrates via polyelectrolyte layers which were deposited by a layer-by-layer deposition technique. This technique was characterised and the process was optimised in order to get uniform high density nanostructures with desirable optical properties. The optical properties of such prepared nanostructured substrates and their dependencies on changes of the local refractive index caused by deposition of thin polymers layers over the nanostructured substrates were measured and compared with theoretical models.

In the latter part of this thesis, experiments measuring plasmonic enhancement of fluorescence from these substrates were carried out. The dependence of the fluorescence enhancement on three different parameters (i) position of localised plasmon resonance, (ii) nanoparticle-dye distance and (iii) nanoparticle coverage were varied in order to optimise the enhancement. The optimal NP-dye distance in our experimental models was found to be 3-6nm. The experiments confirmed that the largest enhancement of fluorescence is achieved when the spectral position of the LSPR overlaps with the absorption spectrum of a dye and that the enhancement factor increases with nanoparticle coverage.

The next stage of this work will involve further analysis of the influence of metal nanostructures on fluorescence from dyes. This will lead to the development of bioassays on these nanosturctured substrates as a step towards the development of commercial biosensor systems incorporating plasmonic enhancement.

This analysis will involve the measurement of the fluorescence life-times of the dye in the vicinity of metal nanoparticles. The measurement of the fluorescence life-time will allow separation of the excitation enhancement effect from the emission enhancement effect. In these experiments the spectral position of LSPR will be tuned into the emission spectrum of the fluorescent dye and the fluorescence intensity together with the fluorescence life-time can be measured.

Another key aspect is the combination of this plasmonic enhancement effect

with other fluorescence enhancement techniques such as super-critical fluorescence emission. In order to implement these two techniques together in a biosensor platform the influence of the nanoparticles on the angular emission of the dye in the proximity of an interface has to be measured.

Further theoretical work will also be carried out concerning the distribution of the electromagnetic field around triangular nanoparticles, which were used in this work. The calculation will be based on the Discrete Dipole Approximation method.

Appendix A

Spherical vector harmonics

The expressions of spherical vector harmonics are [Bohren 1983]

$$\begin{aligned}
\vec{M}^{(i)}_{emn}(\rho,\theta,\phi) &= \frac{-m}{\sin\theta}\sin m\phi P_n^m(\cos\theta) z_n(\rho)\hat{\theta} \\
&\quad - \cos m\phi \frac{dP_n^m(\cos\theta)}{d\theta} z_n(\rho)\hat{\phi} \qquad \text{(A.1)} \\
\vec{M}^{(i)}_{omn}(\rho,\theta,\phi) &= \frac{m}{\sin\theta}\cos m\phi P_n^m(\cos\theta) z_n(\rho)\hat{\theta} \\
&\quad - \sin m\phi \frac{dP_n^m(\cos\theta)}{d\theta} z_n(\rho)\hat{\phi} \qquad \text{(A.2)} \\
\vec{N}^{(i)}_{emn}(\rho,\theta,\phi) &= \frac{z_n(\rho)}{\rho}\cos m\phi n(n+1) P_n^m(\cos\theta)\hat{r} \\
&\quad + \cos m\phi \frac{dP_n^m(\cos\theta)}{d\theta}\frac{1}{\rho}\frac{d[\rho z_n(\rho)]}{d\rho}\hat{\theta} \\
&\quad - m\sin m\phi \frac{dP_n^m(\cos\theta)}{d\theta}\frac{1}{\rho}\frac{d[\rho z_n(\rho)]}{d\rho}\hat{\phi} \qquad \text{(A.3)} \\
\vec{N}^{(i)}_{omn}(\rho,\theta,\phi) &= \frac{z_n(\rho)}{\rho}\sin m\phi n(n+1) P_n^m(\cos\theta)\hat{r} \\
&\quad + \sin m\phi \frac{dP_n^m(\cos\theta)}{d\theta}\frac{1}{\rho}\frac{d[\rho z_n(\rho)]}{d\rho}\hat{\theta} \\
&\quad - m\cos m\phi \frac{dP_n^m(\cos\theta)}{d\theta}\frac{1}{\rho}\frac{d[\rho z_n(\rho)]}{d\rho}\hat{\phi} \qquad \text{(A.4)}
\end{aligned}$$

where the manuscript (i) means

i=1 $z_n(\rho) = j_n(\rho)$, spherical Bessel function first kind

i=2 $z_n(\rho) = y_n(\rho)$, spherical Bessel function second kind

i=3 $z_n(\rho) = h_n^{(1)}(\rho) = j_n(\rho) + iy_n(\rho)$, 1. spherical Hankel function

i=4 $z_n(\rho) = h_n^{(2)}(\rho) = j_n(\rho) - iy_n(\rho)$, 2. spherical Hankel function

and $P_n^m(\cos\theta)$ are associated Legendre function of the first kind of degree n and order m.

Appendix B

Expansion coefficients of the scattered field with silica shell

The scattered field by a sphere of radius a, dielectric constant ε_1, silica shell thickness d of dielectric constant ε_2 has the same expression the scattered field of a sphere without the shell (eqn. 2.53), but the expansion coefficients are in this case [Bohren 1983]

$$a_n = \frac{\psi_n(y)[\psi_n'(m_2y) - A_n\chi_n'(m_2y)] - m_2\psi_n'(y)[\psi_n(m_2y) - A_n\chi_n(m_2y)]}{\xi_n(y)[\psi_n'(m_2y) - A_n\chi_n'(m_2y)] - m_2\xi_n'(y)[\psi_n(m_2y) - A_n\chi_n(m_2y)]} \tag{B.1}$$

$$b_n = \frac{m_2\psi_n(y)[\psi_n'(m_2y) - B_n\chi_n'(m_2y)] - \psi_n'(y)[\psi_n(m_2y) - B_n\chi_n(m_2y)]}{m_2\xi_n(y)[\psi_n'(m_2y) - B_n\chi_n'(m_2y)] - \xi_n'(y)[\psi_n(m_2y) - B_n\chi_n(m_2y)]} \tag{B.2}$$

$$A_n = \frac{m_2\psi_n(m_2x)\psi_n'(m_1x) - m_1\psi_n'(m_2x)\psi_n(m_1x)}{m_2\chi_n(m_2x)\psi_n'(m_1x) - m_1\chi_n'(m_2x)\psi_n(m_1x)} \tag{B.3}$$

$$B_n = \frac{m_2\psi_n(m_1x)\psi_n'(m_2x) - m_1\psi_n(m_2x)\psi_n'(m_1x)}{m_2\chi_n'(m_2x)\psi_n(m_1x) - m_1\psi_n'(m_1x)\chi_n(m_2x)} \tag{B.4}$$

where ψ, ξ and χ are Riccati-Bessel functions

$$\psi_n(\rho) = \rho j_n(\rho) \qquad \xi_n(\rho) = \rho h_n^{(1)}(\rho) \qquad \chi_n(\rho) = -\rho y_n(\rho) \tag{B.5}$$

x, y are the size parameters and m_1, m_2 are the relative refractive indexes

$$x = ka = \frac{2\pi\sqrt{\varepsilon^m}a}{\lambda} \qquad y = k(a+d) = \frac{2\pi\sqrt{\varepsilon^m}(a+d)}{\lambda} \tag{B.6}$$

$$m_1 = \frac{N_1}{N_m} = \sqrt{\frac{\varepsilon^1}{\varepsilon^m}} \qquad m_2 = \frac{N_2}{N_m} = \sqrt{\frac{\varepsilon^2}{\varepsilon^m}} \tag{B.7}$$

List of publications and conference presentations

Oral presentations

1. "Plasmon enhanced fluorescence for biomedical diagnostics", Photonics West, January 2006, San Jose, USA

2. "Plasmonic enhancement using core-shell nanoparticles", Opto-Ireland, 2005, Dublin, Ireland

3. "Plasmonic enhancement of fluorescence for sensor applications", Photonic Crystal Materials and Nanostructures, 2004, Strasbourg, France

Poster presentations

1. "Plasmon enhanced fluorescence for biomedical diagnostics",35th Spring Weekend Meeting of the IOP, March 2006, Bundoran, Ireland

2. "Plasmonic enhancement of fluorescence for sensor applications", Functional properties of Nanostructured Materials, June 2005, Sozopol, Bulgaria (awarded 1st Prize)

3. "Plasmonic enhancement of fluorescence for sensor applications", BOC Gases Poster Competition, , April 2004, Dublin City University, Ireland (awarded 1st Prize)

Peer-Reviewed Publications

1. Nooney R, Stranik O, McDonagh C, MacCraith B D ,"Optimisation of plasmonic enhancement of fluorescence on plastic substrates", in preparation

2. Stranik O, Nooney R, McDonagh C, MacCraith B D ,"Optimisation of nanoparticle size for plasmonic enhancement of fluorescence", *Plasmonics*, online version, 2006

3. Stranik O, McEvoy H M, McDonagh C, MacCraith B D, "Plasmonic enhancement of fluorescence for sensor applications", *Sensors and Actuators B*, Vol. 101, No. 1, pp.148-153, 2005.

4. Mullegger S, Stranik O, Zojer E, Winkler, A, "Adsorption, initial growth and desorption kinetics of p-quaterphenyl on polycrystalline gold surfaces", *Applied surface science*, Vol. 221, No. 1-4, pp.184-196, 2004.

Conference Proceedings

1. Burke C S, Stranik O, McEvoy H M, MacCraith B D, "Planar optical sensors and evanescent wave effects", Chapter 10 in Proceedings of the NATO A. S. I. on Optical Chemical Sensors (40th Course),Publisher: Kluwer Academic NATO A.S.I. series (2006)

2. Stranik O, Nooney R, McDonagh C, MacCraith B D, "Plasmonic enhancement using core-shell nanoparticles", *Proc. SPIE, Nanotechnology and Nanophotonics*, Vol. 5824, 2005, p. 79-85

3. Stranik O, McDonagh C; MacCraith B D, "Plasmonic enhancement of fluorescence for sensor applications", *Proc. SPIE,Photonic Crystal Materials and Nanostructures*,Vol. 5450, 2004, p 144-149.